Ultrafast Dynamics of Photoexcited Bismuth Films

by

Yu-Miin Sheu

A dissertation submitted in partial fulfillment
of the requirements for the degree of
Doctor of Philosophy
(Physics)
in The University of Michigan
2010

Doctoral Committee:

Professor Roberto D. Merlin, Chair
Professor Paul R. Berman
Professor Roy Clarke
Professor Rachel S. Goldman
Associate Professor David A. Reis, Stanford University

ACKNOWLEDGEMENTS

Expressing my gratitude in terms of words can never be enough to disclose how much I appreciate all the support and encouragement in my Ph.D life. Perhaps just a simple discussion or perhaps just an encouragement, as a little boost to an experiment, Ph.D life can never succeed without all of those important factors from those of you I value so much.

I sincerely thank my advisor Professor David Reis, who welcomed me to his group with an enthusiastic attitude toward science. His guidance and discussion leads me a step further toward physics. Without his encouragement and help at difficult times, I could not have attained this level and completed this dissertation. I appreciate his full support for my Ph.D all the time.

I could not have finished this dissertation without discussions with Professor Stephen Fahy and Dr. Donald Walko. I thank you for your zealous discussion with me. These crucial discussions compose the main frame of my dissertation.

My experiments could not have proceeded smoothly without much help from my buddy coworkers, Mariano Trigo and Vladimir Stoica. I thank you for your help, instruction on the techniques, and many discussions for improving the experiments. Your encouragement and enjoyable discussion besides science are also very important in my Ph.D life.

I thank my group members, Jian Chen and Shambhu Ghimire, for sharing fun and pleasure, especially for our weekly lunch and our beamtime in Argonne. I acknowl-

edge previous group members, David Fritz and Soo-Heyong Lee, for your instruction at the start of learning.

I cannot omit acknowledging much help from Eric Landahl, Emily Peterson, and Don Arms. Your rigorous preparation for beamtime made my experiments and data acquisitions possible. I thank Professor Roberto Merlin for serving as my supervisor after my advisor David Reis's leaving to Stanford, and appreciate his loan of an amplifier laser so that I could conduct my experiments, leading to many interesting results. I also thank Dr. Yi-Jiunn Chien, Professor Ctirad Uher, and Professor Rachel Goldman for providing us excellent quality samples for measurements.

I appreciate my relatives', especially my parents', support and encouragement. Every phone call overseas expresses how much you love me and how much you support me. I bear your support in mind to face difficulties bravely and to overcome problems.

Finally, I would like to thank my boyfriend Chih-Piao Chuu. Pursuing my Ph.D originates from your words, which turned my life to a different direction. Your endless support and infinite encouragement bring courage and energy to me every day. With this precious support, I can conquer frustration, beat challenge and move forward. Without discussion with you about science and about making decisions, this moment could never happen. Because of you, I succeed.

TABLE OF CONTENTS

LIST OF TABLES

Table

LIST OF FIGURES

Figure

CHAPTER I

Introduction

The world has been changed by the improvement of technology, which has given birth to computers, cell phones and many other electronics used every day. Technology continues to progress: faster computer processing, more efficient heat removal from devices, smaller electronic devices, and so on. Solids such as metals, semiconductors, and semimetals play a major role in technological products, and their sizes are growing smaller and smaller with time. Nano-technology is now an important field of scientific research, with consequences for energy storage, energy transfer, processing speed, etc.

To study materials at small size scales and to study their physical properties occurring within very short time spans are both important challenges. Ultrafast lasers have become an important non-contact tool for scientists to study generation of elementary excitations in materials and to probe fundamental dynamical processes in solids. A large amount of energy stored in a short laser pulse can coherently excite materials, creating a perturbation which is detectable using either weak pulsed lasers or x rays to capture snapshots over time. The energy from lasers is absorbed in materials to alter the original configuration of electrons and atoms, leading to an unstable system that (for low enough excitations) tends to return to its original

state by a series of processes. Understanding how a excited material relaxes back to equilibrium is important fundamental research and has direct applications towards development of technology. The energy transfer from laser to electrons and then to the lattice is of particular interest due to potential applications for technology such as the improvement of energy storage. One major application is heat removal from devices which may consist of a heterostructure such as a film grown on a substrate.

Measurements of thermal and charge transport in thin films and heat removal across an interface are fundamentally and practically important for manipulating devices where many of the materials properties are still unknown.

In this dissertation, I study the thermal and carrier transport properties of bismuth films on sapphires using ultrafast x-ray and optical techniques. Bismuth is a semimetal and one of the best bulk-thermoelectric materials because it simultaneously exhibits poor thermal conductivity and substantial electrical conductivity, while sapphire is an insulator with high thermal conductivity. Ultrafast techniques are ideally suited for measuring transport phenomena in the sense that they measure the change in physical properties as a function of time following laser irradiation. Time-resolved x-ray diffraction is a relatively new, non-contact method to directly measure changes in atomic structures after materials are rapidly heated by an ultrafast laser. It becomes an important tool for thermal transport by measuring temperature in different materials directly through changes in the lattice constant [1, 2], but is not yet widely used due to a lack of suitable sources and techniques. A similar method for optical pump and probe, measuring change in optical reflectivity or transmission with temperature, is widely used for thermal transport studies [3]; however, it is only indirectly sensitive to atomic-scale structural changes. Also, due to limited laser penetration of the material, optical probes only detect signals near

the surface of an opaque material.

Though we can learn about thermal transport in bismuth from time resolved x-ray diffraction, the detailed mechanisms of energy transfer from photoexcited carriers to the lattice upon ultrafast laser excitation are not yet clear, due to limited x-ray time resolution and lack of x-ray sensitivity to photoexcited carriers.

In addition, recent experiments demonstrate that strong electron-phonon coupling in bismuth can lead to the generation of large-amplitude coherent atomic motion. Studies of these coherent atomic motions investigate the mechanism of optical phonon generation and its subsequent decay. [4, 5, 6, 7, 8, 9, 10]. The observed phenomena become interesting as excitation increases: the frequency of optical phonons is softened, and a frequency chirp is discovered [6, 8]. The photoexcited carriers in Bi are proved to affect the atomic bonding, leading to the observed softening and frequency chirp at high excitation [8]. Although it is clear that photoexcited carriers affect atomic motion as well as lattice heating, the precise mechanism is still not completely understood.

I perform two types of measurements to study the dynamics of photoexcted bismuth films grown on sapphires: time-resolved x-ray diffraction, and optical pump and probe. Time-resolved x-ray experiments directly investigate the atomic motion induced by the laser, while optical pump-probe measurements are carried out to study the change in reflectivity caused by laser modulation of carrier density and atomic motion upon irradiation. The change in atomic motions upon laser excitation includes optical phonon oscillations, strain generation as well as propagation, and lattice heating, which are detectable using both x-ray and laser measurements if time resolution is achieved.

Time-resolved x-ray diffraction investigates lattice dynamics at various depths,

using grazing incident x-ray geometries to reveal the existence of a large thermal gradient near the surface in thick bismuth film (284 nm). Using symmetric diffraction, x rays can monitor the cooling of entire film. The Kapitza conductance of the bismuth/sapphire interface is extracted directly by numerically solving the one-dimensional diffusion equation with corresponding boundary conditions and only two free parameters: initial maximum temperature rise and Kapitza conductance.

In optical measurements, the conventional pump-probe geometry detects the modulation of the dielectric constant corresponding to carrier diffusion, carrier recombination, optical phonon oscillation, acoustic strain propagation, lattice heating and thermal diffusion, which all contribute to early relative change in reflectivity before $\sim$ 20 ps and result in a carrier peak. Although the conventional pump-probe data cannot isolate the individual factors contributing to carrier peak, by investigating counter-propagating pump-probe data we can separate carrier dynamics from acoustic strain as well as lattice heating, making a simple diffusion-decay model possible for data analysis on carrier dynamics.

Optical measurements include low and high excitation, which display dramatic differences in carrier peak and acoustic strain behaviors. The low and high excitations can be characterized by inspecting the A_{1g} phonon softening or the behavior of reflectivity signal as a function of fluence. At low excitation, A_{1g} phonons suffer no softening from excitation carriers and reflectivity signal is nearly linear as a function of fluence in both conventional and counter-propagating pump-probe data, whereas at high excitation the phonon softening occurs and the carrier peak in counter-propagating pump-probe data shows strong saturation as fluence increases.

Analysis of acoustic strain generation allows us to study lattice thermalization after laser irradiation. Expanding on Thomsen's model [11] for strain generation by

incorporating a two-decay model for carriers and comparing data with simulations, an estimate can be made for lattice thermalization time. This analysis further supports a large thermal gradient created near the bismuth surface upon excitation, consistent with the data from time-resolved x-ray diffraction.

This dissertation is organized into 10 chapters. Chapter II is an overview of the properties of bismuth, starting from the introduction of its rhombohedral structure. Thereafter, I introduce the electronic band structure, which plays a particularly important role for the electronic properties of bismuth such as effective mass, optical properties and so on.

Chapter III contains the theory of thermal properties in the solid state. It starts with an introduction of lattice thermal conductivity and the Kapitza conductance. The mechanism of lattice thermal conductivity is discussed. Thermal transport across an interface along with the phonon transmission is presented in terms of two important models, acoustic mismatch and diffusive mismatch models. A review of interface quality and interface scattering is given to explain the limits on phonon transmission.

In chapter IV, I present the theories of three major ultrafast dynamical processes in solids initiated by ultrafast lasers, including optical phonon generation, carrier dynamics, and lattice thermalization with strain generation. First, the section on optical phonon generation compares the impulsive and displacive excitation mechanisms. The displacive excitation can in fact be explained within the framework of impulsive excitation with the introduction of two distinct tensors, one being the standard Raman susceptibility and the other describing the electrostrictive force acting on the ions. Second, the section on carrier dynamics introduces one- and two-chemical potential models which are assumed in the theoretical calculations of

optical phonon generation [8, 12]. The carrier diffusion and carrier recombination mechanisms are presented within the model of two-chemical potential. Finally, the section on lattice thermalization and acoustic strain generation opens with the introduction of Thomsen's model [11] which assumes instantaneous lattice heating. I modify Thomsen's generation model by taking carrier diffusion and recombination into account. In addition to thermally-generated acoustic strain, I also include the non-thermal strain generated from deformation potential coupling. At the end of this section, I use numerical simulation to make the comparison between thermal and non-thermal strain by analyzing the strain generated in bismuth films.

Chapter V discusses synchrotron radiation sources and several x-ray techniques. My experiments use a synchrotron source which has high flux and higher coherence, and can reduce the data collection time by several orders of magnitude compared to the laboratory-based source. The x-ray experiments were carried out in the Advanced Photon Source (APS) at Argonne National Laboratory. I describe the mechanism for x-ray radiation in synchrotron sources and the basic parameters important for timing schemes in APS. I combine Batterman's and Gibaud's approaches [13, 14] to discuss x-ray reflectivity, which is used to measure the film thickness. The timing scheme between ultrafast lasers and x rays is presented, starting from the clock of x-ray bunches. The electronic gates managed to control the delay between lasers and x rays are described. The time resolution is limited by the x-ray bunch duration. Lastly, I discuss the geometry for asymmetric diffraction, which is chosen for grazing incident x-ray measurements. In contrast to symmetric diffraction which preserves the beam divergence (when beam is not focused), asymmetric diffraction requires an understanding of out-going beam divergence in order to manage the geometry for experimental needs.

Chapter VI introduces optical pump-probe techniques, starting from the mechanism of two ultrafast laser systems, oscillator and regenerated amplified laser. I describe the pump-probe setup including two geometries, conventional and counter-propagating. The conventional geometry which pumps and probes the sample from the same side is normally used in the literature for bismuth [5, 6, 8, 10, 15, 16]. I present the setup of counter-propagating pump-probe geometry, which is used to separate carrier peak from acoustic echoes and lattice heating. At the end of the section, I explain the dependence of reflectivity change in carrier density, phonon coordinate, strain, and lattice heating. In addition, I describe the different sensitivity of the change in reflectivity to dielectric function at the two interfaces (air/bismuth and sapphire/bismuth).

In chapter VII, I present the x-ray experiments along with the analysis and discussion. The chapter starts with the film thickness characterization by x-ray reflectivity. Following film characterization, I discuss the relation between lattice change and reciprocal lattice index using a Gaussian beam approximation [2], in order to make the connection between the lattice change and the asymmetric diffraction in reciprocal space. The overview section discusses the measurements from various depths and the related application to lattice thermal conductivity and Kapitza conductance measurement. Subject to certain limitations, I present a condition for distinguishing measurements of film thermal conductivity from Kapitza conductance. From data analysis, the cooling for 65 nm film measured at various depths is dominated by the Kapitza conductance. While the temperature is near homogeneous in the 65 nm film, the 284 nm film shows a large thermal gradient from the study of various grazing incident x-ray measurements. The Kapitza conductance is directly extracted using the symmetric diffraction measurement.

In chapter VIII, I present the optical pump-probe measurements under low excitation, i.e. $\sim 10^{18}$ cm^{-3} excited carriers. The experiments include the combination of pump and probe from either the bismuth surface or the bismuth/sapphire interface. Surface-pump-surface-probe data is presented first, showing no clear difference among film thicknesses above 185 nm. Carrier peak, acoustic echoes and lattice heating are discriminated later in the surface-pump-interface-probe data. A simple diffusion and single decay model is used to fit the data, and the diffusion and recombination of bismuth are extracted at low excitation. In addition, the acoustic strain including thermal and non-thermal contributions is numerically simulated using the modified Thomsen's model discussed in chapter IV. I show that the different boundary conditions for air/bismuth and sapphire/bismuth can be observed from comparison between interface-pump-interface-probe and interface-pump-surface-probe data. The relatively fast diffusion and slow recombination with rapid lattice thermalization of photoexcited bismuth films are concluded in the summary.

Chapter IX contains optical pump-probe measurements and discussion under high excitation for carrier density above 5×10^{19} cm^{-3}. While surface-pump-surface-probe data shows nearly linear behavior up to $\sim 10^{20}$ cm^{-3}, surface-pump-interface-probe data displays strong saturation of the carrier peak. The carrier peak intensity is reduced by up to a factor of 5 compared with the linear prediction for film thickness ranging 185–384 nm. From the fit using two different scaling methods, we conclude the carrier diffusion becomes slower and recombination faster at high excitation, with the possibility of density- or temperature-dependent diffusion and recombination or Auger recombination.

In both chapters VIII and IX, I include the studies for the optically thin film, i.e. 35 nm and 66 nm film. The counter-propagating pump-probe experiments are

not able to isolate carrier peak from acoustic echoes and lattice heating. Under high excitation, the reflectivity data for 35 nm film shows an abnormal negative signal, including carrier peak, for both conventional and counter-propagating pump-probe experiments. The conclusion of fast recombination applies to thin film at high excitation density phenomenologically.

The last chapter contains discussions and conclusions, including suggestions for the improvement in current studies and for possible areas in future research.

CHAPTER II

Bismuth

Bismuth is a group V element with symbol Bi and atomic number 83 in the periodic table. The electronic configuration of Bi is $[Xe]4f^{14}5d^{10}6s^{2}6p^{3}$ with 5 valence electrons in the outer shell per atom. Bi is a poor metal (semimetal) which has the second lowest thermal conductivity of all the metals. However, it has highest Hall coefficient among the metals.

The band structure of semimetal Bi has a conduction band slightly lower than the valence band. The charge carriers are holes at T point and electrons at L point in Brillouin zone [17]. Bi has been studied for transport properties for a long time. Many experiments have been performed for carriers near the fermi surface, including acoustoelectric effect, thermoelectric power, thermomagnetic wave propagation, semimetal-semiconductor transition for thin film, superconducting phase transition at a few kelvin, and so on. The well known de Haas-van Alphen effect and Shubnikov-de Haas effect were first observed in Bi [18]. The oscillation observed in physical properties such as resistivity, specific heat, conductivity, etc., as a function of the field at low temperature originates from the quantization of electron orbits.

Bi is also known as a thermoelectric material. The thermoelectric effect results from a temperature difference at the two ends of a material, creating a voltage

difference and current flow across the specimen. The inverse process occurs when a voltage difference is applied across the material. Yielding a large voltage difference in response to a small temperature gradient, Bi as well as its III-V compounds are attractive thermoelectric materials for power generation.

The above effects are related to Bismuth's electronic band structure, which is strongly influenced by the atomic structure and vice-versa. For example, change in the atomic structure may change the semi-metal Bi to a semiconductor or a better metal. Therefore, it is critical to investigate the crystal structure of Bi and to understand the electronic band structure, in order to study its physical properties further.

In the following section, I overview the rhombohedral structure of Bi. Thereafter, I turn to the electronic band structure, which plays a particularly important role for electronic properties such as effective mass, optical properties, and so on.

2.1 Crystal structure

Two atoms contribute to a unit cell of Bi, which crystalizes with rhombohedral A7 structure. The lattice parameter a is 4.7236 Å and the rhombohedral angle α is 57.35^{o} [19]. A simple way to construct the A7 structure is to perform two consecutive distortions to sodium chloride (face center cubic lattice), as illustrated in Fig. 2.1. We can take sodium and chlorine as two sub-lattices and replace sodium and chloride atoms by Bi atoms. Each sub-lattice contributes an atom to the unit cell. First, a shear distortion extends along the body diagonal, reducing the rhombohedral angle to be less than 60^{o}. The second distortion, known as the Peierls, translates one sub-lattice along the body diagonal. Two atoms in the unit cell located at $\pm$(0.25a, 0.25a, 0.25a) are now at $\pm$(0.234a, 0.234a, 0.234a) [19, 20]. The distortions transform cubic

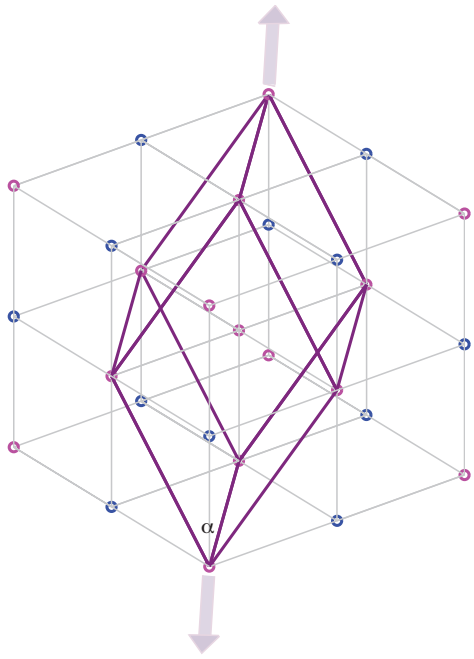

Figure 2.1: A7 structure using NaCl structure with distortions. Blue and magenta points form two sublattices of Bi. A7 crystal structure is derived first by a shear distortion along body diagonal, as indicated in arrows, and second a translation of one sublattice (magenta-point groups) along body diagonal. Rhombohedral structure is indicated by purple line with rhombohedral angle α=57.35^{o} after 2 distortions.

to rhombohedral structure with three-fold symmetry and with trigonal axis (1 1 1) along the body diagonal in cubic lattice. This slight deviation from cubic structure results in a carrier density reduced by a factor of 5 compared with normal metals.

We can also imagine rhombohedral structure by using a hexagonal basis with trigonal axis along (0 0 1) , which is a three Miller index representation in Hexagonal basis. Every six planes (A' B C' A B' C) repeat the same stacking. Planes of (A' C'f B' A') stacking and (A C B A) stacking form two sub-lattices in Bi, shown in Fig. 2.2.

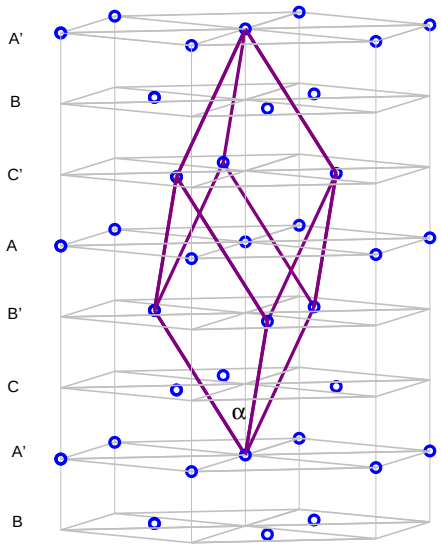

Figure 2.2: A7 structure in hexagonal representation, shown in purple lines. Stacking of (A' C' B' A') and (A C B A) are two sublattice of Bi.

2.2 Electronic band structure

Metals in groups I, II, III, and IV of the periodic table can be described using a near-constant potential for electron motion (very weak periodic potential). Electrons are free-moving conduction electrons and only weakly perturbed by the periodic potential of ions (the so-called near-free-electron model). On the other hand, the isolated atom's wave functions require justifications when the overlap is enough but not too much. This tight-binding approximation is useful for transition metals in which the energy bands arise from partially filled d-shell electrons.

In a perfect crystal, electrons experience a potential $\mathrm{U}(\mathbf{r})$ with periodicity $\mathrm{U}(\mathbf{r}+\mathbf{R}) = \mathrm{U}(\mathbf{r})$, where $\mathbf{R}$ is the Bravais lattice vector. In general, electrons experience both an ionic potential as well as an electron-electron Coulomb interaction, and should be treated as many-body problems. However, the valence electrons are separated from

the ions by the core electrons, and the conduction electrons can screen the positive potential, resulting in a very weak effective potential. For the first order approximation, electrons can thus be treated as a near-free-electron gas in a weakly perturbed periodic potential without electron-electron interaction. Alternatively, the individual atomic wave functions hardly overlap, unless the interatomic spacing becomes comparable to the spatial extent of their wave functions. The Hamiltonian can be treated as arising from isolated atoms at each lattice site (tight-binding model), and the single electronic wave function ψ_n is a linear combination of atomic orbitals ϕ_n. The near-free-electron model solving the one-electron Schrödinger equation works well especially for alkali metals that have a single valence electron per atom, while the tight-binding model is more appropriate for the band arising from the core ion such as transition metals. For a real crystal, more sophisticated approximations are required for band calculations that deal with many-body effects.

Before exploring electronic band structure in periodic crystals, it is crucial to recall Bloch's theorem, which gives remarkable insight into solid state. The theorem states that the wave function corresponding to a one-electron Hamiltonian can be written as a plane wave times a function with periodicity of the Bravais lattice in a periodic potential $\mathrm{U}(\mathbf{r}+\mathbf{R}) = \mathrm{U}(\mathbf{r})$:

$$\psi_{n\mathbf{k}} = e^{i\mathbf{k}\cdot\mathbf{r}} u_{n\mathbf{k}}(\mathbf{r}) \tag{2.1}$$

where

$$u_{n\mathbf{k}}(\mathbf{r}+\mathbf{R}) = u_{n\mathbf{k}}(\mathbf{r}). \tag{2.2}$$

From the periodic boundary condition $\psi(\mathbf{r}+N_i\mathbf{a}_i) = \psi(\mathbf{r})$, it can be found that the

allowed Bloch wave vector is

$$\mathbf{k} = \sum_{i=1}^{3} \frac{m_i}{N_i} \mathbf{b}_i, \tag{2.3}$$

where $\mathbf{b}_i$ are reciprocal vectors of the primitive vectors $\mathbf{a}_i$, and $\mathbf{N}_i$ are integers such that $N = N_1 N_2 N_3$ is the total number of primitive cells in the crystal. Bloch's theorem implies that the wave function at position $\mathbf{r}$ times plane wave $e^{i\mathbf{k}\cdot\mathbf{R}}$ will give the wave function at position $\mathbf{r} + \mathbf{R}$, i.e.

$$\psi(\mathbf{r} + \mathbf{R}) = e^{i\mathbf{k}\cdot\mathbf{R}} \psi(\mathbf{r}). \tag{2.4}$$

Any wave vector $\mathbf{k}'$ not in the first Brillouin zone can be represented as $\mathbf{k}' = \mathbf{k} + \mathbf{K}$ where $\mathbf{K}$ is the reciprocal lattice vector so that $e^{i\mathbf{K}\cdot\mathbf{R}}$=1. Thus from Bloch's theorem, it is clear that any information outside the first Brillouin zone can be folded into the first Brillouin zone (reduced zone scheme represented as $-\pi/a < k < \pi/a$), and the full $\mathbf{k}$ space can be restricted to a single primitive cell.

Applying Bloch's theorem to the eigenvalue problem for the Schrödinger equation with $\mathbf{k}$ restricted to a primitive cell and applying the boundary condition to eq.2.2, one can find an infinite family of solutions with discrete eigenvalues labeled by band index n for continuous $\mathbf{k}$. What follows for the electron wave function and eigenvalues is [21]

$$\psi_{n,\mathbf{k}+\mathbf{K}}(\mathbf{r}) = \psi_{n,\mathbf{k}}(\mathbf{r}) \tag{2.5}$$

and

$$\varepsilon_{n,\mathbf{k}+\mathbf{K}} = \varepsilon_{n,\mathbf{k}}, \tag{2.6}$$

which are in correspondence with the electronic band structure in crystals. Sometimes, Bloch's theorem is represented in the alternative form [21]

$$\varepsilon_{n,\mathbf{k}+\mathbf{K}} = \varepsilon_{n,\mathbf{k}}, \tag{2.7}$$

by choosing the eigenstate of the Hamiltonian. One can write down the electron wave function as a linear combination of plane waves with wave vectors that satisfy eq.2.3, i.e. $\psi(\mathbf{r}) = \sum_{\mathbf{q}} c_{\mathbf{q}} e^{i\mathbf{q}\cdot\mathbf{r}}$. The same trick applies to the potential with wave vectors of the reciprocal lattice, i.e. $\mathrm{U}(\mathbf{r}) = \sum_{\mathbf{K}} U_{\mathbf{K}} e^{i\mathbf{K}\cdot\mathbf{r}}$. Replacing these wave functions and potentials into the Schrödinger equation and performing some manipulation, the eigenvalue problem becomes

$$\left(\frac{\hbar^2}{2m}(\mathbf{k}-\mathbf{K})^2 - \varepsilon\right) c_{\mathbf{k}-\mathbf{K}} + \sum_{\mathbf{K}'} U_{\mathbf{K}'-\mathbf{K}} c_{\mathbf{k}-\mathbf{K}'} = 0. \tag{2.8}$$

The eigenvalue problem can be solved in two cases: non-degenerate and near-degenerate electrons. For the non-degenerate case, the free electron energy $\varepsilon^0_{\mathbf{k}-\mathbf{K}}$ is far from the value $\varepsilon^0_{\mathbf{k}-\mathbf{K}_i}$ for all reciprocal lattice vectors $\mathbf{K}_i, i = 1, ..., m$ in the limit of weak periodic potential, $c_{\mathbf{k}-\mathbf{K}}$ is dominated by the second order of U, and the shift in energy is also second order in U. On the other hand, for the near-degenerate case, the shift in energy can be liner in U, and the leading order in the weak periodic potential is linear in U that significantly shifts the energy level. Therefore, the near-degenerate case is responsible for energy shift in electronic band calculation.

For the near-degenerate electrons, the values of k, K_1,..., k_m, and $\varepsilon^0_{\mathbf{k}-\mathbf{K}_i}$ with i=1,2,...m have relation:

$$\left|\varepsilon^0_{\mathbf{k}-\mathbf{K}} - \varepsilon^0_{\mathbf{k}-\mathbf{K}_i}\right| >> U, \quad \mathrm{K} \neq \mathrm{K}_1, ..., \mathrm{K}_m. \tag{2.9}$$

The coefficient $c_{\mathbf{k}-\mathbf{K}}$ can be approximated to the first order in U,

$$c_{\mathbf{k}-\mathbf{K}} = \frac{1}{\varepsilon - \varepsilon^0_{\mathbf{k}-\mathbf{K}}} \sum_{j=1}^{m} U_{\mathbf{K}_j-\mathbf{K}} c_{\mathbf{k}-\mathbf{K}_j} + O(U^2),$$

$$\mathbf{K} \neq \mathbf{K}_1, \mathbf{K}_2, ..., \mathbf{K}_m. \tag{2.10}$$

Thus the eigenvalue problem from eq.2.8 becomes

$$(\varepsilon - \varepsilon^0_{\mathbf{k}-\mathbf{K}_i}) c_{\mathbf{k}-\mathbf{K}_i} = \sum_{j=1}^{m} U_{\mathbf{K}_j-\mathbf{K}_i} c_{\mathbf{k}-\mathbf{K}_j} + \sum_{\mathbf{K}\neq\mathbf{K}_1,....\mathbf{K}_m} U_{\mathbf{K}-\mathbf{K}_i} c_{\mathbf{k}-\mathbf{K}}. \tag{2.11}$$

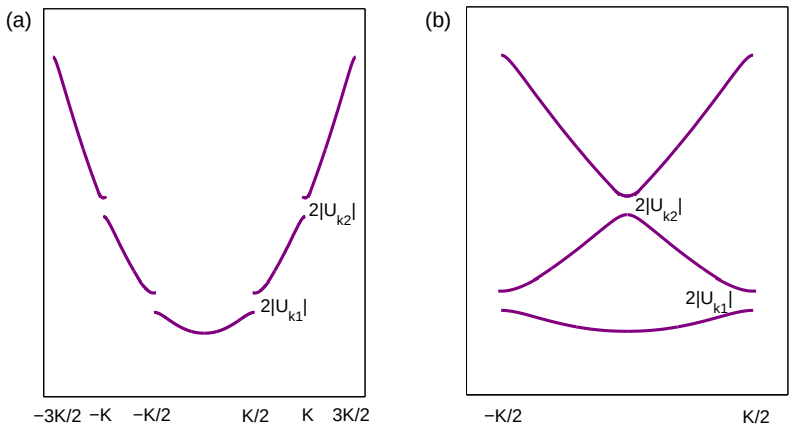

Figure 2.3: Band structures in different representations. (a) First-3-band structure from near-free-electron model in extended zone scheme. When wave vector meets Bragg condition q=$\mathbf{K}/2=\pi/\mathrm{a}$, the band opens a gap $2|U_{\mathbf{K}}|$. (b) Band structure in reduced zone scheme, which folds the band back to the first Brillouin zone by subtraction of n$\mathbf{K}$ with integer n to make the new wave vector fall into first Brillouin zone, preserving the same structure.

Substituting eq.2.10 into eq.2.11, we have

$$(\varepsilon - \varepsilon^0_{\mathbf{k}-\mathbf{K}_i})c_{\mathbf{k}-\mathbf{K}_i} = \sum_{j=1}^{m} U_{\mathbf{K}_j-\mathbf{K}_i} c_{\mathbf{k}-\mathbf{K}_j} + O(U^2) + O(U^3). \tag{2.12}$$

In the non-degenerate case, there is only $\mathbf{K}_1$ in eq.2.12. The summation over index i vanishes because we are at liberty to change the potential energy by an additive constant and can take $U_{\mathbf{K}=0} = 0$.

For the simplest illustration, consider two electrons which have levels within order U of each other but far compared with U from all other levels. Making use of $\mathbf{q} = \mathbf{k} - \mathbf{K}_1$ and $\mathbf{K} = \mathbf{K}_2 - \mathbf{K}_1$, eq.2.12 for $i = 1, 2$ becomes

$$(\varepsilon - \varepsilon^0_{\mathbf{q}})c_{\mathbf{q}} = U_{\mathbf{K}} c_{\mathbf{q}-\mathbf{K}}, \tag{2.13}$$

and

$$(\varepsilon - \varepsilon^0_{\mathbf{q}-\mathbf{K}})c_{\mathbf{q}-\mathbf{K}} = U_{-\mathbf{K}} c_{\mathbf{q}} = U^*_{\mathbf{K}} c_{\mathbf{q}}. \tag{2.14}$$

The solution for ε is

$$\varepsilon = \frac{1}{2}(\varepsilon^0_{\mathbf{q}} + \varepsilon^0_{\mathbf{q}-\mathbf{K}}) \pm \left[\left(\frac{\varepsilon^0_{\mathbf{q}} - \varepsilon^0_{\mathbf{q}-\mathbf{K}}}{2} \right)^2 + |U_{\mathbf{K}}|^2 \right]^{1/2}. \tag{2.15}$$

When $\mathbf{q} = \frac{1}{2}\mathbf{K}$, i.e. zone boundary, the two solutions are separated by a gap $2|U_{\mathbf{K}}|$. In general, when the wave vector is a multiple of $\mathbf{K}/2$, i.e. $j\mathbf{K}/2$ with integer j, one solution raises while the other solution lowers the energy of free electrons. This is the condition for Bragg reflection to happen. Fig. 2.3(a) and Fig. 2.3(b) show the results of electronic band in an extended and reduced zone scheme respectively. If the crystal periodicity a changes, for example to a'=2a, it will open new gaps due to the reduced reciprocal wave vector. It is clear that near-free electrons in a weak periodic potential are primarily affected if their wave vectors are close to the zone boundary where the Bragg reflection happens. The concepts of Bloch's theorem, near-free-electron model, and the band gap opening near the Bragg plane describe the fundamental electronic band structure in the crystal. More sophisticated calculation may predict the electronic band structures in more detail; however, they are simply extended from these basic concepts and are modified with more complicated approximations regarding the electron-electron or electron-ion interactions.

For N primitive cells in the crystal, each one contributes one independent wave vector $\mathbf{k}$ to each energy band. Every energy band can accommodate two spin orientations due to Pauli exclusion and there will be 2N orbitals in every energy band. For even numbers of valence electrons in a primitive cell the band is filled, and the crystal is an insulator because electrons are not free to change momentum in the filled states. If odd numbers of valence electrons fill the band, the crystal is a metal because there are still available states in the band for momentum transfer. When a field is applied, electrons are free to flow in the metal. If the band is filled by 2N

electrons with band gap $E_g < k_B T_r$ at room temperature, electrons can be excited to the upper band with thermal energy. This type of crystals are semiconductors, and they become insulators at T=0 without excess thermal energy to promote electrons to higher bands. Ordinarily, even numbers of electrons in the crystal would fill up a band completely. However, for a band that is slightly overlapping with a higher band, the electrons which would fill upper energy levels in the lower band will instead fill the more energetically favorable bottom of the higher band. This results in a partially filled higher band and mostly filled lower band, and the crystal becomes conductive when the field is applied. This type of crystal is a semimetal, such as Bismuth.

Bismuth has two atoms in the primitive cell and 5 valence electrons per atom, yielding 10 valence electrons per primitive cell. For 10N electrons in N primitive cells, Bi will fill up to the 5th band. However, due to the 36 meV band overlap between the fifth and sixth bands, valence electrons are filled up to the sixth band with carrier density $\sim 3 \times 10^{17}$ cm^{-3} at room temperature. The band structure of Bi was first calculated using the tight-binding model including the spin-orbital coupling by Mase [22], who correctly predicted the location and symmetry of the carriers. Other common band calculation methods were carried out later by various physicists, Ref. [19, 23, 24] for example. The common results such as electron effective mass, g factors, pressure effects and optical properties were calculated by Golin [17] using a pseudopotential calculation, with which physicists were able to compare the earlier experimental results. Golin's results are also extensively used for the explanation of later experiments [25, 26, 27]. The pseudopotential is an effective potential based on the near-free-electron model with weak crystal potential, taking into account the core electrons and nucleus. Although the real crystal potential is much larger than

Table 2.1: Possible critical points of optical transitions in Bi.

Designation	Energy a.u. (experiments)	Bands	Symbols	Energy a.u. (calculated)
E1	0.044	5→7	$L_a \rightarrow L_s$	0.042
E2	0.11	4→7	$L_a \rightarrow L_s$	0.11
E3	0.32	4→8	$X_s \rightarrow X_a$	0.32

the pseudopotential, it has been proved that they have the same eigenvalues. The usual approach to constructing a pseudopotential is to choose a reasonable form of the potential with a few adjustable parameters which are varied until the results agree with the experiments. Golin's pseudopotential includes three parts: the local potential V_l, the spin-orbital coupling V_{so}, and an l (angular momentum) dependent term that increases the energies of the level with s-atomic character V_s. Three adjustable parameters account for the effective-mass anisotropies and other properties of Bi. Golin established a good agreement with earlier experimental results. He proposed that the holes are located at the T point near fermi level, and chose his pseudopotential to locate the electron at the L point according to an experiment on electron-phonon recombination [28]. Thus he predicted the locations of 3 optical transitions which were observed in experiments as $L_a \rightarrow L_s$ (E=0.044 a.u.), $L_a \rightarrow L_s$ (E=0.11 a.u.), and $X_s \rightarrow X_a$ (E=0.32 a.u.). Table 2.1 lists these corresponding transitions.

The detailed band structures of Bi from Golin's calculation are shown in Fig. 2.4(a), and first Brillouin zone with several symmetry points is shown in Fig. 2.4(b).

Note that due to slight overlap of the L point at 6th band and the T point at 5th band, Bi is a semimetal with low carrier concentration under normal conditions. Because of the translation of second sublattice of Bi, it has 2 atoms per unit cell. Were it not for this distortion, Bi would only have 1 atom per unit cell and the reciprocal wave vector would be twice as the one with translation distortion (Peierls

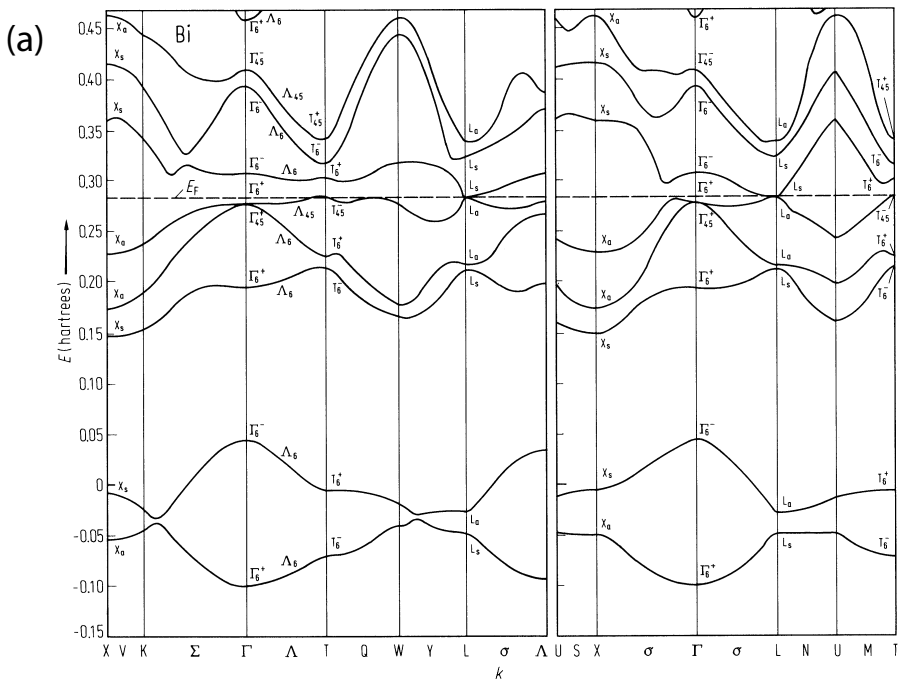

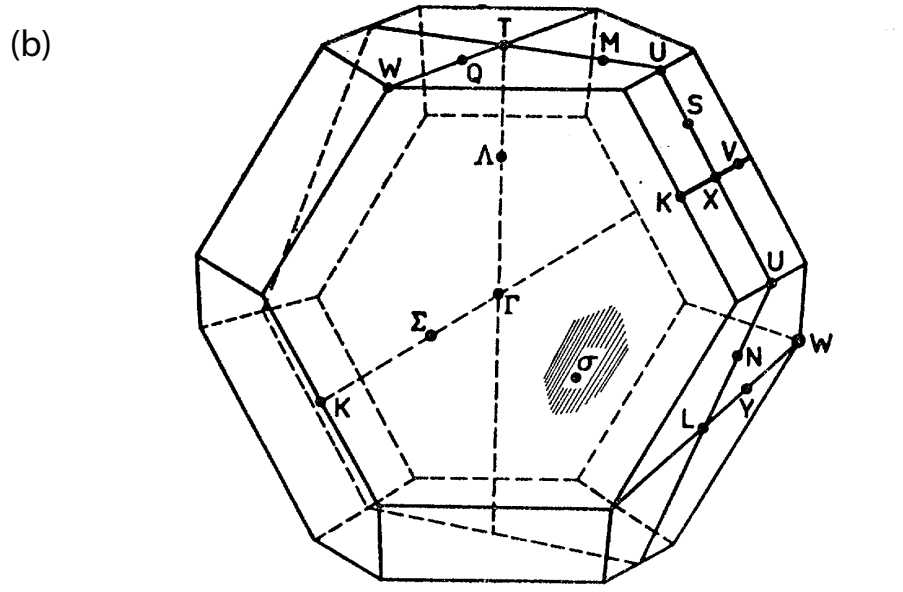

Figure 2.4: Bi band structures calculated by Golin [17]. The hole packets are located at T point and electron packets are located at L point. (b) First Brillouin zone of Bi with several symmetry points from Ref. [17].

distortion). Therefore, without distortion it would close one gap for every 2 gaps. For 5 valence electrons per atom, Bi without Peierls distortion would fill up to the 3rd band. With the translation distortion, there are two atoms per unit cell and electrons fill the band up to the 5th one, which corresponds to the lower part of the 3rd band without distortion. Because of gap opening due to Peierls distortion, the maximum energy of the 5th band is lower than the maximum energy of the 3rd band in the case without gap opening. Thus, Peierls distortion reduces the electronic configuration energy in one dimension. For systems in more than one dimension, the distortion is not always energetically favorable because it would raise the configuration energy in other dimensions. For Bi, this is a preferred structure because the reduction in the distorted direction is greater than the increased energy along other dimensions, leading to an overall reduced configuration energy.

CHAPTER III

Thermal Transport

As well as being conducted by electrons, heat can be carried by phonons, a form of vibration mode in crystal. Just as a photon is the quantum of an electromagnetic wave, a phonon is quantized from crystal vibration. Each phonon carries energy and its occupation follows the Bose-Einstein distribution when in thermal equilibrium. Phonons can interact with phonons or electrons, resulting in different physical properties for various crystals. Whereas electronic thermal conductivity characterizes heat transfer by electrons, lattice thermal conductivity characterizes thermal transport by phonons.

In an idealized perfect harmonic crystal, phonons are stationary and the distribution remains unchanged over time. Therefore, if a phonon distribution in a perfect harmonic crystal carried thermal current, the current would not change in time. The thermal conductivity is then close to infinity. The lattice does not expand and has constant heat capacity at high temperature ($>$ Debye temperature). However, imperfections in real crystals can cause phonon scattering and change the thermal current. Even for the perfect crystals, the full Hamiltonian including anharmonic terms produces only an approximately stationary state, and phonon occupation number does not remain the same at all times. This is the intrinsic limitation of infinite thermal

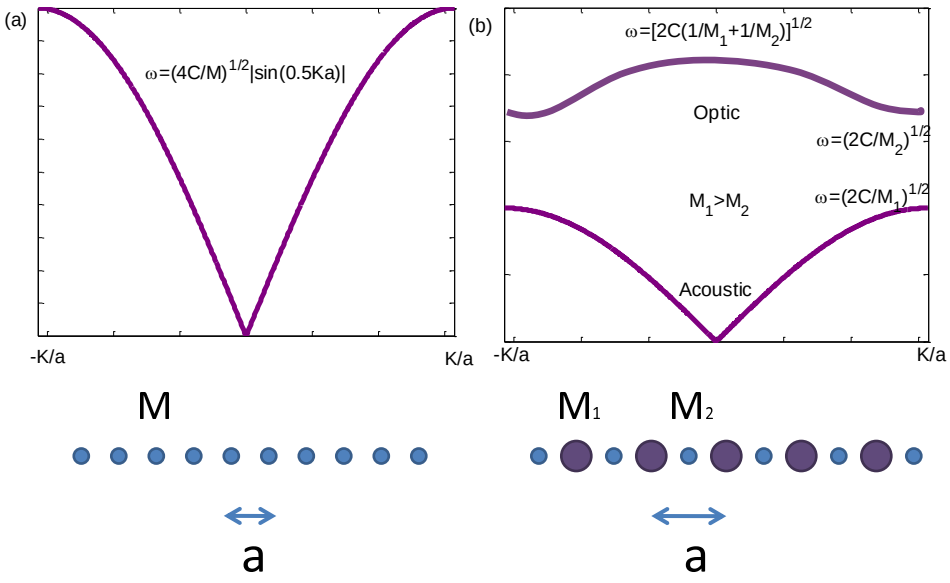

Figure 3.1: Dispersion relation for (a) one dimensional Bravais lattice and for (b) one dimensional lattice with a basis.

conductivity of perfect crystals.

Classically, crystals can be modeled starting from the harmonic approximation. Solving the equation of motion with the harmonic potential in periodic atoms gives the allowed normal modes. In the one dimensional monatomic Bravais lattice with N atoms and atomic separation a, only one acoustic branch is allowed with frequency ω and wave vector $k = 2n\pi/(Na)$. This wave propagates with phase velocity ω/k and group velocity $v = \partial\omega/\partial k$. The relation between ω and k is the dispersion relation usually drawn from $k = -\pi/a$ to $k = \pi/a$ in the reduced zone scheme, i.e. first Brillouin zone. For a linear lattice with two distinct atoms as basis, one acoustic and one optical branch are allowed. The dispersion relation for these two cases can be seen as in Fig. 3.1. In general, for three dimensional lattices with a basis there are $3p$ normal modes for each $\mathbf{k}$ vector, where p is the number of ions in the basis.

Three of the normal modes are acoustic branches which have frequency close to 0 in long wavelength limit, i.e. k approaching zone center. The other $3(p-1)$ are optical branches and their frequencies do not vanish as k approaches zone center (long wavelength limit).

One of the physical properties that can be discussed in the harmonic approximation is the specific heat, which is defined as the temperature derivative of internal energy. The internal energy is carried by all phonons, and the specific heat c_v can be written as [29]

$$c_v = \frac{1}{V}\sum_{\mathbf{k},s}\frac{\partial}{\partial T}\frac{\hbar\omega_s(\mathbf{k})}{\exp^{\hbar\omega_s(\mathbf{k})/kT}-1}. \tag{3.1}$$

where phonon wave vector is $\mathbf{k}$ in branch s. If $\Delta\mathbf{k} \to 0$ and the crystal volume $V \to \infty$, the summation over $\mathbf{k}$ can be replaced by an integral $\int \mathrm{d}\mathbf{k}/(2\pi)^3$ over first Brillouin zone and the sum is over only s. Many approximations exist to express the specific heat analytically [21, 30]; among them Debye's approximation is most widely used. Debye's approximation replaces all vibrational modes with three branches having the same dispersion relation $\omega = ck$, and the integral over first Brillouin zone is replaced by an integral over a sphere of radius k_D. Using the dispersion relation, the Debye frequency ω_D is the cutoff frequency for integral with Debye temperature $k_B\Theta_D{=}\hbar\omega_D$. When T$>\Theta_D$, the classical statistics are valid. For T$<\Theta_D$, the specific heat can be approximately calculated analytically and follows the so called Debye T^3 law where specific heat increases as a function of T^3.

However, there are many physical properties that cannot be explained by using only the harmonic approximation. Higher order terms must be considered in order to explain the phenomena. The general properties can be grouped into equilibrium properties like thermal expansion, and transport properties like thermal conductiv-

ity. Lattice thermal conductivity is perhaps the most important transport property determined from the anharmonic potential. In this chapter, I introduce the concept and theory of thermal transport across the bulk material, i.e. thermal conductivity. I discuss the transport across an interface, in which case temperature may not be continuous and the discontinuity of temperature is determined by the Kapitza conductance. The discontinuity across an interface is due to the fact that the phonon transmission is not equal to unity. Phonon transmission across an interface is discussed based on two models, acoustic mismatch and diffusive mismatch models. Some reviews about Kapitza conductance and the interface qualities are also presented in this chapter.

3.1 Lattice thermal conductivity

This section discusses lattice thermal conductivity, where heat is carried by phonons. The anharmonic approximation and lattice thermal conductivity are presented by using kinetic theory. Important factors that alter lattice thermal conductivity are discussed, including normal as well as Umklapp process, alloy scattering, and reduced reciprocal lattice. Those processes are related to phonon scattering, which is subtle and complex and can be contributed from the scattering centers, the presence of an interface or the crystal temperature.

3.1.1 Anharmonic approximation

Usually among the higher order terms of the interatomic potential, cubic and quartic terms are most important. Assuming that displacement is small and perturbation is valid, the transition due to cubic and quadratic term can be illustrated as in Fig. 3.2. They must follow both crystal momentum conservation and energy

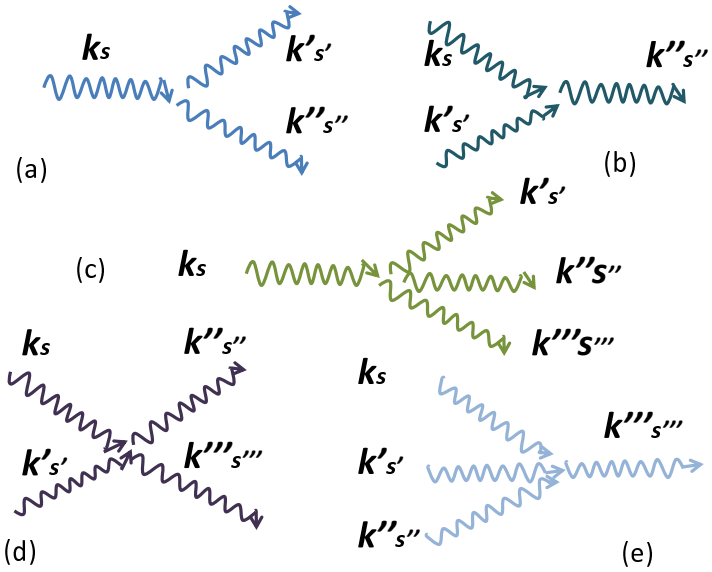

Figure 3.2: Anharmonic processes in the perturbation theory for cubic term (a) and (b), and quadratic term (c) (d) and (e).

conservation for the initial and final states, i.e. [31]

$$\sum \hbar\omega_s(\mathbf{k}) n_{\mathbf{k},s} = \sum \hbar\omega_s(\mathbf{k}) n'_{\mathbf{k},s} \tag{3.2}$$

and

$$\sum \mathbf{k} n_{\mathbf{k},s} = \sum \mathbf{k} n'_{\mathbf{k},s} + \mathbf{K} \tag{3.3}$$

where $\mathbf{K}$ is the reciprocal lattice vector, and $n_{\mathbf{k},s}$, $n'_{\mathbf{k},s}$ are phonon occupation numbers before and after transition respectively. The processes of these diagrams are often called collisions, and they do not need to obey the conservation of number. Phonons can be created and annihilated during these processes constrained by the conservation of energy and crystal momentum.

3.1.2 Kinetic theory of lattice thermal conductivity

In this section, the thermal conductivity is expressed in terms of heat flow and the temperature gradient. For a small temperature gradient along the x direction,

the heat flux (thermal current) is defined as the energy transmitted across unit area and unit time:

$$j = \kappa \left(-\frac{\partial T}{\partial x} \right), \tag{3.4}$$

where κ is the thermal conductivity. Because of the dependence on thermal gradient, the heat flow is not ballistic, i.e. not propagating along a straight line. It is diffusive, depending on the varying temperature across the specimen. Collisions happen frequently during diffusion. Energy density is contributed by phonons, where only the last phonon collision contributes to net thermal current. Thus the thermal current density along the x axis is the product of energy density and the velocity along x direction that determines where phonon comes from to make a collision. Using the Drude model, one has $l = v\tau$ where l is the mean free path of a particle between collisions and τ is the average time between collisions. For a collision with an angle θ to the x axis,

$$j =< v\cos\theta \; u(x_0 - l\cos\theta) >_\theta = \int_{-1}^{1} v\cos\theta \; u(x_0 - l\cos\theta) 2\pi d(\cos\theta)/4\pi. \tag{3.5}$$

Thus, from the first order approximation, the temperature gradient is

$$j = -vl\frac{\partial u}{\partial x}\frac{1}{2}\int_{-1}^{1}\cos^2\theta d\cos\theta = \frac{1}{3}vl\frac{\partial u}{\partial T}\left(-\frac{\partial T}{\partial x}\right). \tag{3.6}$$

Comparing eq.3.4 and eq.3.6, thermal conductivity is

$$\kappa = \frac{1}{3}vl\frac{\partial u}{\partial T} = \frac{1}{3}vlC_v, \tag{3.7}$$

where C_v is specific heat of the phonons, l is the average collision length depending on the collision rate τ^{-1}=l/v. It is clear that thermal conductivity depends on the

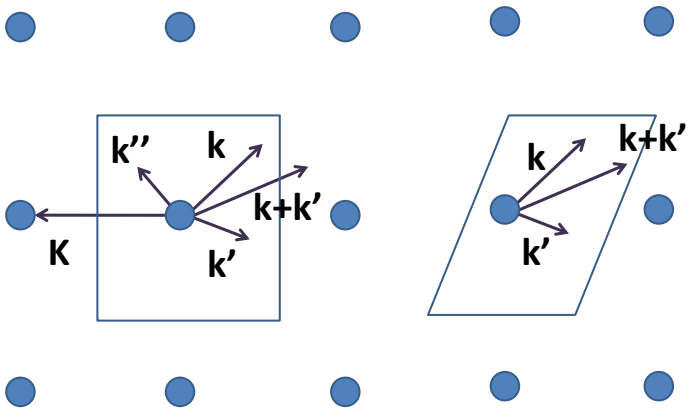

Figure 3.3: Cartoon for Umklapp and normal processes. (a) Umklapp process with an involved reciprocal wave vector in the momentum conservation. $\mathbf{k}''$ is folded back from $\mathbf{k}+\mathbf{k}'$ into the first Brilloin zone by a subtraction of reciprocal wave vector $\mathbf{K}$. (b) The normal process with strictly crystal momentum conservation. The different processes are based on the choice of primitive cell in this diagram.

phonon scattering process. If scattering rate increases, the thermal conductivity decreases. The thermal conductivity is a function of specific heat which depends on temperature following Debye T^3 law when temperature is below Debye temperature. Therefore, the thermal conductivity increases with increasing temperature. However, as temperature rises, scattering probability increases and reduces the phonon mean free path. Thus the increase of temperature corresponding to the increase of thermal conductivity is limited by the higher scattering rate above the Debye temperature.

3.1.3 Normal and Umklapp process

There are two important scattering processes, normal and Umklapp. When the scattering happens leaves the crystal momentum unchanged, i.e. no presence of reciprocal wave vector $\mathbf{K}$, the scattering is called the normal process. On the other hand, when scattering happens involving the change in a reciprocal wave vector, i.e.

a phonon created with the wave vector equal to sum of the original phonon wave vector and reciprocal wave vector **K** as in eq.3.3, the scattering is called the Umklapp process. The difference is shown in Fig. 3.3.

These two processes dominate for different temperature ranges. At high temperature, there are more available energy states for phonons excitation, and the probability of scattering that happens with creation of a phonon outside the first Brilloiun zone increases. On the contrary, for low temperature ($T < \Theta_D$) only phonons with energy comparable to temperature can be excited. For the limited amount of phonons at low temperature, the scattering that creates a phonon with crystal momentum **K** larger than the original one is more unlikely. Thus, at low temperature, the Umklapp process is frozen. However, it dominates at higher temperature.

3.1.4 Alloy scattering, reduced reciprocal lattice, and reduced size effect

Similar to imperfections serving as scattering centers, the structure of an alloy also produces scattering. For an alloy structure, the atoms are random mixture of different elements with different masses and volumes. One alloy scattering model created by Abeles [32] first used an ordered virtual crystal with mass density and elastic constant the same as an alloy crystal. However, the thermal conductivity of an alloy compound would still be below that of the virtual crystal in the model. To deal with this issue, Abeles then replaced the atoms in the virtual crystal with atoms of different mass and size, so-called virtual impurities. The coupling constant between neighborhoods of these virtual impurities is described by the ″misfit″ strain field. In the case of two mixture atoms A and B in the alloy with radius δ' and mass M , the relaxation rate Γ is

$$\Gamma = x(1-x)\left(\frac{\Delta M}{M}^2 + \epsilon\left(\frac{\Delta\delta}{\delta}\right)^2\right) \tag{3.8}$$

with

$$\Delta M = M_A - M_B \quad , \quad \Delta\delta = \delta'_A - \delta'_B \tag{3.9}$$

and

$$M = xM_A + (1-x)M_B, \tag{3.10}$$

where ϵ is a phenomenological adjustable parameter. This alloy scattering model correlated well to the properties of $Al_xGa_{1-x}As$ measured by Afromowitz [33], assuming perfect lattice match between GaAs and AlAs.

For the reduced reciprocal lattice case such as superlattice, i.e. the multilayer of periodic , there have been many experiments [34, 35, 36] studying thermal conductivity, showing that the cross plane thermal conductivity is smaller than that of their alloy compounds. Because of the new periodicity of superlattice structure, the artificial period $(a+b)$ from A and B compounds reduces the reciprocal wave vector to be $2\pi/(a+b)$. This is less than $2\pi/d$, where the periodicity d of the atoms is on the order of the atomic radius, and a, b are usually on the order of nanometers. For this new periodicity, the Umklapp process require less energy to occur.

Generally, the scattering is sensitive to structures on a scale comparable to the phonon wavelength. If phonon wavelength is shorter than a layer thickness, phonons can be treated as particles and their motions are governed by the Boltzmann transport equation. However, when layer thickness decreases and is comparable to phonon mean free path, the size effect needs to be taken into account. This also applies to thin films, so long as phonon mean free path is comparable to the length scale of the medium.

3.2 Kapitza conductance, interface and interface scattering

Thermal transport across an interface is described by the Kapitza conductance. This section starts from the definition of Kapitza conductance. It discusses the factors that can change the phonon transmission across an interface, i.e. interface quality and interface scattering. A few experiments regarding the interface properties are reviewed in this section.

3.2.1 Kapitza Conductance

Kapitza conductance measures the temperature discontinuity across an interface. The first measurement of temperature discontinuity was by Kapitza in 1941, reporting temperature drop across the boundary between helium and solid. This was later explained in terms of thermal boundary resistance, which causes a temperature drop in the same way as electrical resistance causes a drop in the voltage. The inverse of thermal boundary resistance is known as Kapizta conductance or interface conductance. If ΔT is temperature difference across an interface and Q is the heat current density, the Kapitza conductance σ_K is defined as

$$\dot{Q} = \sigma_K \Delta T. \tag{3.11}$$

The temperature discontinuity is due to the non-unity phonon transmission. If the phonons in material A cannot transmit through an interface to material B, the thermal energy stored in A cannot transmit either.

If phonons have frequency $\omega_{\mathbf{k}j}$ with wave vector $\mathbf{k}$ and polarization j, the Kapitza conductance between A and B for heat transfer from A (B) to B (A) can also be written as [37]

$$\sigma_K(T) = \frac{1}{V}\frac{\partial}{\partial T}\sum_{\mathbf{k}j}^{A(B)} \hbar\omega_{\mathbf{k}j} n(\omega_{\mathbf{k}j}, T)|v_{\mathbf{k}jz}|T_{\mathbf{k}j}, \tag{3.12}$$

where the summation is over first Brilliouin zone, V is the volume, $T_{\mathbf{k},j}$ is the transmission of phonons, $v_{\mathbf{k}jz}$ is phonon group velocity along the normal direction to the interface, and $n(\omega_{\mathbf{k}j}, T)$ is Bose-Einstein distribution function.

To understand the details of temperature jump between two materials, it is necessary to know the details of phonon transmission across the interface. The next two sections describe two models of phonon transmission. In each model, we can get a simplified expression for the Kapitza conductance by adding some assumptions.

3.2.2 Acoustic mismatch model (AMM)

If phonons propagate in a medium with lattice spacing shorter than phonon wavelength, they can be approximately treated as continuum acoustic. Assuming phonons are incident to a plane interface, they can partially specularly reflect and partially refract with or without mode conversion. The acoustic mismatch model (AMM) treats the displacement and stress of the crystal with appropriate boundary conditions, i.e. both normal and tangential components are continuous. The results of phonon transmission are analogous to that of light transmission, and Snell's law is applicable. For phonons with incident angle θ to the plane normal, the transmission coefficient T_{AB} (from A to B medium) is expressed in terms of acoustic impedance $Z = \rho v$ as

$$t_{AB}(\cos\theta_A) = \frac{4 Z_A \cos\theta_A Z_B \cos\theta_B}{(Z_A \cos\theta_A + Z_B \cos\theta_B)^2}, \tag{3.13}$$

where ρ is mass density of the material and v is phonon velocity. The reflection coefficient is

$$R_{AB}(\cos\theta_A) = \left| \frac{Z_A \cos\theta_A - Z_B \cos\theta_B}{Z_A \cos\theta_A + Z_B \cos\theta_B} \right|^2 \tag{3.14}$$

Similar to light incident onto a plane surface, only phonons incident within a critical angle $\sin\theta_c = v_A/v_B \times \sin\theta_B$ can transmit. From the boundary conditions in AMM,

only elastic scattering is taken into account, and the transmitted phonons have the same frequency as incident phonons. No mode conversion happens in AMM. Therefore, $T_{AB} = T_{BA}$ and $R_{AB} = R_{BA}$. In the real case of interfaces between different materials, the phonon spectrums are not the same for both sides. High frequency phonons in medium A cannot transmit to medium B if B does not have the same frequency in the spectrum. It follows that high frequency phonons will be confined in medium A, so T_{AB} is no longer equal to T_{BA}. The correction to the transmission coefficient can be made as [38]

$$T_{BA} = \frac{T_{AB} I_{A,eq} \cos\theta_A (d\cos\theta_A)}{I_{B,eq} \cos\theta_B (d\cos\theta_B)}, \tag{3.15}$$

where I_{eq} is the equilibrium phonon intensity and in material A the intensity I_A is

$$I_A = \frac{1}{2\pi} \sum_j \int_0^{\omega_{max}} |v_{A,j}| \hbar\omega n(\omega_{\mathbf{k}j}, T) D_{A,j}(\omega) d\omega. \tag{3.16}$$

Using Debye's approximation at low temperature, the phonon group velocity can be taken out from the integration of eq.3.12. From the transmission coefficient calculated by AMM, the integral over all frequencies is equal to specific heat. Kapitza conductance for heat current from A to B is approximately [38]

$$\sigma_K = \frac{v_A C_A \int_{2\pi} T_{AB}(\cos\theta_A)(d\cos\theta_A)}{2}. \tag{3.17}$$

3.2.3 Diffusive mismatch model (DMM)

By contrast, diffusive mismatch model (DMM) treats the transmission in terms of the phonon density of state on either side of an interface. The scattering completely destroys the correlation between the incident and the transmitted phonons. For phonons incident onto an interface, the possibility of scattering forward or backward from an interface depends on the relative density of states on both sides. All structures of the scatters are also ignored. Incoming phonons lose memory of where they

come from, and the probability of reflection from one side is equal to the probability of the transmission from the other side, i.e.

$$T_{AB} = R_{BA} = 1 - T_{BA} \tag{3.18}$$

From Debye's approximation at low temperature, the transmission can be written as [38, 39]

$$T_{AB} = \frac{\sum_j v_{B,j}^{-2}}{\sum_j v_{A,j}^{-2} + \sum_j v_{B,j}^{-2}}. \tag{3.19}$$

At higher temperature, the phonon dispersion relation has to be taken into account due to phonon excitation from the zone boundary. The frequency integral from eq.3.16 of the product of the phonon density of state and velocity has to be done numerically. However, Chen [38] gave a simple approximation at high temperature by differentiating eq.3.16 with respect to the temperature at equilibrium, which is

$$\frac{dI_0}{dT} = \frac{vC}{4\pi}. \tag{3.20}$$

This assumes that the temperature variation is small and specific heat is constant over the medium. The integration over temperature for the above equation results in

$$I_0 = \frac{vC(T - T_{ref})}{4\pi}, \tag{3.21}$$

where T_{ref} is the reference temperature. Assuming that scattering processes are all diffusive and allowing scattering to be elastic or inelastic for phonons with all frequencies, the transmission coefficient at high temperature is

$$T_{AB} = \frac{v_B C_B}{v_A C_A + v_B C_B}. \tag{3.22}$$

In the diffusive limit, phonons are isotropically distributed. Therefore, we apply Debye's approximation at low temperature, obtaining the approximate Kapitza con-

ductance [38]

$$\sigma_K = \frac{v_A C_A T_{AB}}{4}. \tag{3.23}$$

3.2.4 Interface quality

Generally at low enough temperature, phonon mean free path is very long. If no other scattering occurs and the interface is smooth, AMM can explain the Kapitza conductance of a solid-solid interface. When temperature increases, phonon mean free path decreases and the interface becomes relatively less smooth. In this case, we would expect DMM to be closer to the experimental results. However, at higher temperatures, most experiments cannot be explained by either AMM or DMM. Indeed, the difference between AMM and DMM is usually within 30% [3], which is not enough to explain the deviation for many experiments at high temperature.

Swartz and Pohl have systematically tested the influence of interface quality on the Kapitza conductance [40]. They used Rh:Fe on sapphire with H_2 annealed/polished, synton, diamond, and aluminum polished sapphire as substrates. For H_2 annealed sapphire, the product of Kapitza resistance and T^3 ($R_{th}T^3$) at low temperature is close to the AMM prediction, while for 10-20 K it is close to the DMM prediction. For both diamond and syton polished sapphires, the measurements of $R_{th}T^3$ are close to the DMM with higher Kapitza resistance even at low temperature. The sapphire treated with aluminum does not diffusely scatter phonons any more than the sapphire annealed by H_2 (thermal resistance is smaller than the prediction from AMM). Swartz and Pohl also measured the effect of thermal boundary resistance for a series of interfaces sandwiched with oxide interlayers of various thickness between Rh:Fe and sapphire. The results show that even the thinnest interlayer causes more significant phonon scattering than sapphire treated with diamond.

Swartz and Pohl's experiments strongly indicate that the quality of an interface affects the measurement of thermal boundary resistance even below 1 K, and the results dramatically deviate from either AMM or DMM at higher temperature.

3.2.5 Inelastic scattering

The discussion so far has only focused on elastic scattering without phonon mode conversion. If mode conversion is allowed, i.e. one high frequency phonon can become two low frequency phonons or vice versa, the transmission probability should increase due to down conversion (from higher frequency to lower frequencies). This effect becomes more apparent when two mediums have very different Debye temperatures. When one Debye temperature is much lower than the other and a high frequency phonon is excited, the high frequency phonon should be reflected back because this frequency is disallowed on the other side. However, inelastic scattering can occur if the high frequency phonon down converts to lower frequencies. Through inelastic scattering, a high frequency phonon can transmit through the interface and increase the Kapitza conductance at higher temperatures.

Generally, phonon collision is similar to that of the classical gas in a cylindrical tube with two walls. However, inelastic scattering does not conserve the number of phonons, and the non-exactly conserved crystal momentum at higher temperatures makes phonon scattering more complex, as do impurities and surface scattering. Many effects could result in deviation from the theoretical model. In such cases, sample preparation as well as extremely careful measurements are required for studying thermal transport in crystals.

CHAPTER IV

Ultrafast excitation and dynamics in solids

Light can promote electrons in materials to an excited state that may then relax through multiple processes. As electrons leave their original states, holes are created in the original band. The transition may be direct with the same wave vector or indirect with the change in wave vector compared to the original state. Indirect transition involves the absorption or emission of phonons, and a wave vector changes in a manner obeying momentum conservation. Electrons at higher bands are not stable, tending to go back to their original electronic configuration which gives the lowest free energy and annihilate holes. The process whereby excited electrons return to their original states is called recombination. Electronic transition is not limited to that from upper valence band to lower conduction band (across the band gap), as indicated from discussion of Bi band structure in Chap. II.

The transition of electrons by absorbing light determines the transparency of materials. If the energy of the light is smaller than the band gap, the material is transparent to this wavelength. Otherwise, the material is opaque with strong absorption when the energy of the light is greater than the band gap.

Before recombination, excited electrons may undergo scattering including electron-electron and electron-phonon scattering. Scattering can be elastic with conservation

of both energy and momentum, or inelastic with creation or annihilation of phonons that conserves total energy. Nowadays, due to the improvement of laser technology, ultrafast lasers with high power in a short pulse are useful tools to study materials at highly excited states. In addition, the progress of ultra-short pulse makes it possible to probe the dynamics of excited states as a function of time, although the time resolution is limited by the laser pulse width.

Because the excitation volume is restricted to the laser penetration depth, the generation of excited electrons is near the surface of excitation in opaque materials. The term "excited carriers" or "excited electrons" are used to denote those electrons promoted from their original states. Either free carriers or valence electrons can absorb photons and leave to excited states. Highly energetic carriers have the potential to diffuse deep into material. Many types of dynamics can take place before carrier relaxation or recombination. After carrier relaxation, the energy of the carriers is transferred to the lattice, heating it. The corresponding lattice expansion generates the coherent acoustic strains which propagate into the bulk [11]. If the structure of materials includes an interface, acoustic strain can partially reflect and partially transmit across the interface. Acoustic propagation is useful for the measurement of either film thickness or speed of sound, if one of the properties is known. In addition to the acoustic strain generation, the heated volume gives rise to a temperature gradient which is homogenized by thermal diffusion.

The dynamics and the responses of ultrafast-excited materials are complex and subtle. Each process can be an independent topic of study. However, they are often correlated to each other, which makes analysis challenging. In this chapter, I describe the basic and common physics of these types of dynamics, starting from coherent phonon generation including impulsive stimulated Raman scattering and

progressing to displacive excitation of coherent phonons. Following that, I overview general carrier dynamics upon excitation. The acoustic generation as well as strain propagation are discussed thereafter. Slower dynamics such as the thermal diffusion process have already been discussed in Chap. III. Note that the generation mechanisms discussed here are for above bandgap excitation in opaque materials, except the impulsive excitation of coherent phonons.

4.1 Impulsive and Displacive Excitation of Coherent Phonons

In optical pump-probe experiments, an ultrafast laser is usually split into a strong pump and a weak probe. The pump beam excites materials by altering the carrier system over a very short time, and the probe beam detects the change in the system by measuring the change in optical properties such as transmission or reflection. The idea of the weak probe is to detect the system without a second disturbance. Because the system is in a different electronic configuration, the corresponding dielectric function is changed. The highly excited system is not stable and will gradually recover its original state.

Since the development of femtosecond laser technology, many pump-probe experiments have discovered oscillations with frequencies corresponding to optical phonons in semiconductors, metals and semimetals. These phonons generated by ultrafast lasers are coherent phonons. Many theories attempt to explain the mechanisms of coherent phonon generation. There are two mechanisms that are now commonly accepted to explain the phenomenon: impulsive stimulated Raman scattering (ISRS) [7, 41] and displacive excitation of coherent phonons (DECP) [4].

For the ISRS mechanism, a laser field serves as an external driving force to suddenly change the equilibrium positions of ions. As a results, the ions is that they

start to oscillate if the driving duration is less than half the cycle of their allowed vibration period. The equation of motion can be written as

$$\frac{d^2Q}{dt} + \Omega^2 Q = \frac{1}{2}\left(\frac{\partial\chi}{\partial Q}\right)|E_0(\mathbf{r},t)|^2 = F(\mathbf{r},t), \tag{4.1}$$

where Q is the phonon field, χ is electronic susceptibility, Ω is the phonon frequency, E is the pump electric field, and F is driving force.

For more general systems of transparent materials with excitation energy below the band gap and with the inclusion of phonon dissipation, the equation of motion is [7, 41]

$$\ddot{Q}(\mathbf{r},t) + \Gamma\dot{Q}(\mathbf{r},t) + \frac{1}{8\pi^3}\int \Omega_q^2 e^{-iq(\mathbf{r}-\mathbf{r}')}Q(\mathbf{r}',t)d^3\mathbf{r}'d^3q = \frac{1}{2}\left(\sum_{kl}\frac{\partial\chi_{kl}}{\partial Q}E_kE_l^+\right), \tag{4.2}$$

and the equation for the interaction of the probe field is [7, 41]

$$\nabla^2 e_k = \frac{1}{c^2}\times\frac{\partial^2}{\partial t^2}\left(n^2e_k + 4\pi\sum_{kl}\frac{\partial\chi_{kl}}{\partial Q(\mathbf{r},t)e_l}\right). \tag{4.3}$$

Here, the equation is written in terms of the susceptibility as a tensor χ_{kl} , where q is phonon wave vector, $\mathbf{k}$ or $\mathbf{l}$ are band index, e is probe field and n is index of refraction. When phonon modulation starts with time delay δ to the pump excitation in the bulk material, the solution for the probe intensity change with respect to the unperturbed probe intensity is a cosine form [7]

$$\frac{\sum_{\mathbf{k}}\int|e_{\mathbf{k}}|^2du}{\int|e_0|^2du} \approx 1 - \frac{L\sigma}{c}e^{-\Gamma\delta/2}\cos(\Omega\delta), \tag{4.4}$$

where the modulation is proportional to the slab thickness L, $u = t - zn/c$, pulse width $\tau_0 \ll u$, damping $\Gamma \ll \Omega$, and σ is

$$\sigma = \frac{\pi^{3/2}}{2n}|E_0|^2 e^{-\Omega^2/\tau_0^2} \times \sum_{kl,mp} \left(\frac{\partial \chi_{mp}}{\partial Q} \cos(\alpha_m) \cos(\alpha_p) \right) \times \left(\frac{\partial \chi_{kl}}{\partial Q} \cos(\beta_k) \cos(\beta_l) \right), \tag{4.5}$$

with $\cos(\alpha_m)$=E_m/E_0.

If the contribution from the interface is considered, there is an additional term to both transmission and reflection including the boundary condition at $z = 0$ and $z = L$, which is proportional to $\sin(\Omega\delta)$ and has $\pi/2$ phase difference from the bulk contribution [42].

DECP was first used only to explain coherent phonon generation in opaque materials, such as Bi, Sb and Te [4], whereas the assumption of a strongly absorbing material is not required in ISRS. For opaque materials with more than one Raman active mode, early pump-probe experiments show that only the A_{1g} mode appears. Not all the materials have A_1 mode vibration. A structure with A_1 mode is derived from a "virtual crystal" of higher symmetry by unclear displacements (Peierls distortion for example) which increase the size of unit cell. These displacements, which preserve the symmetry of actual crystal, are A_1 symmetry displacements [4]. Materials with A_1 vibration mode such as Bi and Sb are opaque to the pump laser, and resonant transition happens when laser light is applied. Due to the disturbance of the electronic distribution by absorption, the equilibrium positions of ions in a unit cell are changed by a displacement of A_1 symmetry. In DECP, usually the measurement is set up to detect the change in optical reflectivity, because laser penetration depth for strongly absorbing materials is short and transmission geometry is more challenging unless the sample is thin enough to have a detectable transmitted signal. The oscillation observed in pump-probe experiments is proportional to $\sin(\Omega\delta)$ in

the ISRS mechanism and is proportional to $\cos(\Omega\delta)$ in the DECP mechanism. If the excitation by ISRS is resonant, the oscillation also has cosine behavior but all the Raman active mode will appear [4].

The phenomenologically interpreted DECP mechanism was later explained within the framework of ISRS modulated with two distinct tensors [7, 43], χ^R_{kl} and π^R_{kl}. The tensor χ^R_{kl} is the standard Raman susceptibility, and π^R_{kl} is a new tensor describing the electrostrictive force acting on the ions. The real parts of the tensor are identical, but their imaginary parts greatly differ, leading to the oscillation observed in the DECP model. In the limit t $\rightarrow \infty$, the phonon field in eq.4.1 becomes

$$\lim_{t\to\infty} < Q(t) >= \frac{-i}{\sqrt{8\pi}\Omega}[e^{i\Omega t}F(-\Omega) - e^{-i\Omega t}F(\Omega)], \tag{4.6}$$

where $F(\Omega)$ is the Fourier transform of $F(t)$ so that a real $F(\Omega)$ results in $Q(t) \propto \sin(\Omega t)$ for excitation below bandgap, and pure imaginary $F(\Omega)$ gives $Q(t) \propto \cos(\Omega t)$ for excitation above bandgap. If the Raman tensor is written in terms of linear dielectric tensors $\varepsilon_{ij}(\omega)$ and the decay rate of the nth state is near zero as well as $|\Omega/\omega| \ll 1$, the two tensors can be approximately expressed as [43]

$$\begin{aligned}\chi^R(\omega, \omega+\Omega) &\approx \frac{\Xi_0}{4\pi\hbar\Omega}[\varepsilon(\omega+\Omega) - \varepsilon(\omega)] \\ &\approx \frac{\Xi_0}{4\pi\hbar}\left[\frac{d\mathrm{Re}(\varepsilon)}{d\omega} + i\frac{d\mathrm{Im}(\varepsilon)}{d\omega}\right],\end{aligned} \tag{4.7}$$

and

$$\begin{aligned}\pi^R(\omega+\Omega, \omega) &\approx \frac{\Xi_0}{4\pi\hbar\Omega}[\varepsilon(\omega+\Omega) - \varepsilon^*(\omega)] \\ &\approx \frac{\Xi_0}{4\pi\hbar}\left[\frac{d\mathrm{Re}(\varepsilon)}{d\omega} + 2i\frac{\mathrm{Im}(\varepsilon)}{\Omega}\right],\end{aligned} \tag{4.8}$$

where Ξ is dipole moment so that the electron-phonon and electron-radiation interaction are given by $-\hat{\Xi}\hat{Q}$. In addition, the driving force is [43]

$$F(t) = \frac{Nv_c}{4\pi} \sum_{kl} \int_{-\infty}^{+\infty} \int_{-\infty}^{+\infty} e^{-i\Omega t} E_l(\omega) \pi_{kl}^R(\omega, \omega - \Omega) E_k^*(\omega - \Omega) d\omega d\Omega. \tag{4.9}$$

Inserting eq.4.8 into eq.4.9 and Fourier transforming we get

$$F(\Omega) \propto \left[\frac{d\mathrm{Re}(\varepsilon)}{d\omega} + 2i \frac{\mathrm{Im}(\varepsilon)}{\Omega} \right] \int_{-\infty}^{+\infty} e^{i\Omega t} |E(t)|^2 dt. \tag{4.10}$$

The real part of ε leads to $F(t) \propto |E(t)|^2$ which is a characteristic of impulsive excitation, while the imaginary part of ε gives $F(t) \propto \int_{-\infty}^{t} |E(t')|^2 dt'$ which is a characteristic of displacive excitation. Because phonons couple to a carrier density that decays after a few oscillation cycles in the strongly absorbing case, the driving force is steplike rather than impulsive.

Early experiments suggested that only A_{1g} is excited in opaque materials like Sb, Bi, Te [4], leading to the original construction of the DECP model. The discovery of E_g phonons in Bi, Sb in later experiments [5, 6, 44] supports the hypothesis that DECP can in fact be explained within the framework of ISRS.

4.2 Carrier Dynamics

When electrons absorb energy from light, the dynamics become very complex. The transition depends on the wavelength of light as well as the electronic band structure. In this section, the details of transition is not included. After carrier excitation, the lattice can gain energy from carrier relaxation. The energy of carrier and lattice system can be expressed in terms of the one- or two-temperature model, depending on the duration of interaction between the laser pulse and the system. Two mechanisms, the one- and two-chemical potential models, that are normally used for the description of excited carriers in theoretical calculations [12, 45] are introduced in this section.

4.2.1 One- and Two- Temperature Models

Upon laser excitation, electrons are promoted away from the fermi level. For a short laser pulse with duration less than the time required for carrier and lattice to reach equilibrium, once electrons thermalize with themselves carriers can be represented by their Fermi-Dirac distribution with an effective temperature T_e after absorption of photons. Before equilibrium, the lattice stay at it original temperature T_l and can be represented by a Bose-Einstein distribution. This is the well-known two-temperature model of the photoexcited carriers and lattice systems. On the other hand, if the pulse duration is long compared to the carrier-lattice equilibrium time, the carrier and lattice can be simply described as the same temperature, and carrier concentration is determined by the Fermi-Dirac distribution at a lattice temperature higher than the original temperature of lattice before photoexcitation.

In the case of a long pulse ($t_{eq} \gg t_{pulse}$, equilibrium time less than pulse duration), when phtoexcited electrons thermalize themselves within pulse duration, the temperature of carrier system can be expressed as [46],

$$C_l \frac{\partial T}{\partial t} = \kappa_l \frac{\partial^2 T}{\partial z^2} + A(z,t), \tag{4.11}$$

where C_l is lattice specific heat, κ_l is lattice thermal conductivity, z is along the sample normal, and $A(z,t)$ is the heat contributed by the laser pulse. The system temperature is the equilibrium temperature of both lattice and photoexcited carriers. This is the thermal diffusion equation modified with a heat source for adding energy continuously to the system until the end of the laser pulse.

For short laser pulse ($t_{eq} \gg t_{pulse}$), the system is described by a coupled equations in terms of the separate temperatures of the carriers (T_e) and the lattice (T_l) [46, 47,

48]

$$C_e(T_e)\frac{\partial T_e}{\partial t} = \kappa_e \frac{\partial^2 T_e}{\partial z^2} - g(T_e - T_l) + A(x,t), \tag{4.12}$$

$$C_l \frac{\partial T_l}{\partial t} = g(T_e - T_l), \tag{4.13}$$

where C_e is electronic specific heat, κ_e is electronic conductivity, and g is electron-phonon coupling parameter. Before equilibrium is reached between lattice and carriers, electrons thermalize themselves quickly by electron-electron scattering. Meanwhile, the inhomogeneous spatial distribution leads to diffusion along the sample normal. The equilibrium between carrier and lattice is achieved by the electron-phonon coupling constant g. In a metallic system it is usually expressed as $g \simeq \pi^2 mnv_s^2/6\tau_{eq}$ [46] where m is electron mass, n is electron density, v_s is sound velocity, and τ_{ep} is electron-phonon collision time. Through electron-phonon interaction, carriers transfer energy to the lattice, and g is temperature-independent. Note that the electron specific heat (C_e) is temperature-dependent. Since the temperature of electrons can be normally heated to a few thousand Kelvin by using an ultrafast laser, the specific heat cannot be approximated as a constant as in the lattice system. Lattice specific heat C_l is usually treated as a constant for experiments at room temperature, due to small increase of temperature and smooth variation of specific heat above room temperature.

In the two-temperature model, the diffusion of carriers can be ignored if sample thickness is comparable to or less than the optical penetration depth. In some cases, the diffusion equation requires some modification in order to account for the possible ballistic transport of carriers. Additionally, depending on the character or quality of samples the electron-imperfection scattering needs to be considered in the equation.

Based on different cases, these equations could become complicated; however, the distinct feature of having two separate temperature system for carriers and lattice before equilibrium is straightforward.

In metallic systems measured by short laser pulses and described by the two-temperature model, if laser energy is lower than the interband transition, the d band electrons will not be excited and only free carrier absorption occurs. With a short and intense laser pulse below transition energy, broad non-Fermi distributed carriers are created, carrying energy up to photon energy by assuming one photon absorption per electron. Through electron-electron scattering, non-thermalized carriers redistribute energy to follow the Fermi-Dirac distribution. During or after this process, they can also exchange energy with the lattice by electron-phonon scattering. In a phenomenological explanation, carriers can be separated into two groups, thermalized and non-thermalized. Thermalized carriers can be expressed by the carrier temperature, while the total energy N is required for the description of non-thermalized carriers. The thermalized carriers can be expressed as in the two-temperature system with a source adding carrier numbers from the nonthermalized carriers at carrier heating rate α. In addition to thermalized electrons, non-thermalized carriers can also exchange energy to the lattice with energy transfer rate β. Thus, the total energy of non-thermalized carriers decays into two parts, thermalized carriers and thermal energy in the lattice. The coupled and modified two-temperature equation become [49],

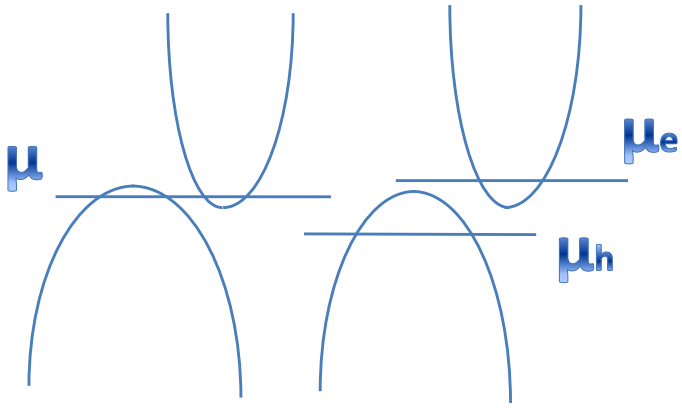

Figure 4.1: Illustration of one and two chemical potential.

$$\frac{dN}{dt} = -\alpha N - \beta N, \tag{4.14}$$

$$C_e \frac{dT_e}{dt} = -g(T_e - T_l) + \alpha N, \tag{4.15}$$

$$C_l \frac{dT_l}{dt} = g(T_e - T_l) + \beta N. \tag{4.16}$$

4.2.2 Carrier Transport in Two-Chemical Potential

Two models have been used for the photoexcited carriers in Bi, one- and two-chemical potential models [12, 45], in order to account for the influence of photoexcited carriers on the A_{1g} phonon generation in density fuctional theory calculations. Both these two models assume that short laser pulses are used, and that the photoexcited carriers do not reach thermal equilibrium with the lattice at the end of pulse. Fig. 4.1 illustrates the physical difference between these two models.

In the one-chemical potential model, it is assumed that there is no heat exchange between ions and electrons upon laser excitation, so that the entropy of the electrons is a constant of motion which is the only constraint in the model. In addition,

electron-electron scattering leads to thermalized carriers at all times, and carriers follow the Fermi-Dirac distribution with a single chemical potential μ [12].

In the two-chemical potential model, on the other hand, the numbers of photoexcited electrons and of holes are constrained to be equal. Electrons and holes are assumed to be instantaneously thermalized to and to follow Fermi-Dirac distribution with the same temperature T_e and separate chemical potentials μ_e and μ_h respectively. The electron concentration in the conduction band is the integration over the entire band of the product of density of state and Fermi distribution

$$n_e = \int_{E_c}^{\infty} D_e(\epsilon) f_e(\epsilon) d\epsilon = 2 \left(\frac{m_e k_b T}{2\pi\hbar} \right)^{3/2} \exp[(\mu_e - E_c)/k_b T] \\ = n_0 \exp[(\mu_e - E_c)/k_b T], \tag{4.17}$$

where Fermi distribution for electrons with conduction band edge E_c is

$$f_e(\epsilon) = \frac{1}{e^{E_c - \mu_e/k_B T_e} + 1}, \tag{4.18}$$

and density of state $D_e(\epsilon)$ is

$$D_e(\epsilon) = \frac{1}{2\pi^2} \left(\frac{2m_e}{\hbar} \right)^{3/2} (\epsilon - E_c)^{1/2}. \tag{4.19}$$

Similarly to the electron concentration, the hole concentration is calculated with Fermi distribution replaced by $f_h{=}1 - f_e$. Therefore, with valence band edge E_v, the hole concentration in the two-chemical potential model is

$$n_h = n_0 \exp[(E_v - \mu_e)/k_b T]. \tag{4.20}$$

From eq.4.17 and 4.18, it is clear that when temperature changes or carriers cool, electrons and holes can maintain equal density by varying their own chemical

potential separately.

Electron and hole current are driven in the two-chemical potential model by the gradient of chemical potential [50]

$$j_e = -R_e \frac{d\mu_e}{dz} n_e = R_e \times kT \frac{dn_e}{dz}, \tag{4.21}$$

$$j_h = -R_h \frac{d\mu_h}{dz} n_h = R_h \times kT \frac{dn_h}{dz}, \tag{4.22}$$

where $R_{e,h} \times kT$ corresponds to carrier diffusivity, giving the diffusion contribution to the spatial density change of electrons and holes by

$$\frac{dN_e}{dt} = -\frac{dj_e}{dz} \quad \text{and} \quad \frac{dN_h}{dt} = -\frac{dj_h}{dz}. \tag{4.23}$$

In addition to density change due to spatial diffusion, photoexcited electrons can recombine with holes in a process driven by the difference between their chemical potentials $(\mu_e - \mu_h)$:

$$\frac{dn_e}{dt} = -K(\mu_e - \mu_h)(n_e + n_h), \tag{4.24}$$

$$\frac{dn_h}{dt} = -K(\mu_e - \mu_h)(n_e + n_h), \tag{4.25}$$

and also driven by the change in the carrier temperature T_e:

$$\frac{dn_e}{dt} = n_e \left(\frac{E_c - \mu_e}{k_B T_e^2} \right) \frac{dT_e}{dt}, \tag{4.26}$$

$$\frac{dn_h}{dt} = -n_h \left(\frac{E_v - \mu_h}{k_B T_e^2} \right) \frac{dT_e}{dt}. \tag{4.27}$$

Thus carrier diffusion, change in carrier temperature, and electron-hole recombination all can lead to the decay of photoexcited carriers:

$$\frac{dn_e}{dt} = -R_e \times kT\frac{d^2n_e}{dz^2} - K(\mu_e - \mu_h)(n_e + n_h) + n_e\frac{(E_c - \mu_h)}{kT^2}\frac{dT_e}{dt}, \tag{4.28}$$

$$\frac{dn_h}{dt} = -R_h \times kT\frac{d^2n_h}{dz^2} - K(\mu_e - \mu_h)(n_e + n_h) + n_h\frac{(E_v - \mu_h)}{kT^2}\frac{dT_e}{dt}. \tag{4.29}$$

Assuming one photon absorption per electron-hole pair, energy exchange between the carriers and the lattice is through electron-hole recombination or carrier cooling via electron-electron scattering. Carrier cooling can be driven by the difference of lattice and carrier temperature as well as electron-hole recombination

$$\begin{aligned}\frac{dT_e}{dt} &= -g'(T_e - T_l) - \frac{2}{3k(n_e + n_h)}(\mu_e - \mu_h)\frac{dn_e}{dt} \\ &= -g'(T_e - T_l) + \frac{2K}{3k}(\mu_e - \mu_h)^2,\end{aligned} \tag{4.30}$$

where $3k(n_e + n_h)/2$ is assumed for the carrier heat capacity and g' here is electron-phonon coupling constant divided by the carrier heat capacity. Assuming classical phonons and Dulong-Petit heat capacity per unit volume, $3n_{at}$, the lattice gains energy from the carriers through

$$\frac{dT_l}{dt} = g(T_e - T_l)\frac{(n_e + n_h)}{n_{at}}. \tag{4.31}$$

For a short laser pulse, Eq.4.30 and 4.31 are two-temperature equations for photoexcited carriers and lattice under the assumption that electrons and holes have separate chemical potentials μ_e and μ_h respectively.

4.3 Acoustic Generation and Propagation

Upon lattice gain energy from photoexcited carriers, thermal expansion can launch an acoustic strain to propagate in the material. Due to the sudden lattice expansion,

a stress is generated in the lattice. A corresponding strain forms according to the boundary conditions, with propagation similar to the string wave. The propagation of strain is a useful tool for the measure of either sample thickness or speed of sound, by the relation $L = vt$ where L is sample thickness, v is speed of sound and t is propagation time.

If an interface is present, the strain can partially reflect and partially transmit. The study of transmission and reflection across an interface contains useful information about acoustic impedance as well as the properties of an interface. The details of the transmission properties of acoustic strains are discussed in Chap. III.

In this section, I start with Thomsen's model [11, 51] for the strain generation and propagation assuming instantaneous heating. I also discuss how to modify the model if the heating is not instantaneous but gradual, and I discuss the strain generated from deformation potential as well as give the general comparison between thermal and non-thermal strain.

Assume laser energy Q with projection area A is absorbed in the sample, laser penetration depth is ζ, and lattice specific heat is C_l per unit volume of the sample. If the energy absorbed in the sample has an exponential profile as a function of depth z, then

$$W(z) = \frac{Q}{A\zeta} e^{-z/\zeta} \tag{4.32}$$

is the energy per unit volume deposited in the sample. The lattice absorbs energy from photons and increases in temperature with a profile as a function of depth z

$$\Delta T(z) = \frac{W(z)}{C_l} = \frac{Q}{CA\zeta} e^{-z/\zeta}. \tag{4.33}$$

The increase in lattice temperature will set up a thermal stress

$$-3B\alpha\Delta T(z), \tag{4.34}$$

assuming the sample is isotropic, bulk modulus is B, and linear expansion coefficient is α. Normally, the laser projection area A ($\sim$ 10 $\mu m-$ few 100 μm) is much larger than the sample thickness ($\sim nm$ $-$ few μm), and the probe beam mainly detects the dynamics parallel to the sample normal or the normal of laser projection. This is true unless during the time-scale of interest the in-plane dynamics has spread out of the probe region. Since the stress is along the sample normal, the motion of strain is also along z according to the relation

$$\sigma_{ik} = \frac{\partial F}{\partial \eta_{ik}}, \tag{4.35}$$

$$\eta_{ik} = \frac{\partial F}{\partial \sigma_{ik}}, \tag{4.36}$$

with stress σ, strain η, and free energy F [52]. The free energy by definition is written as [52]

$$F = \frac{3B(1-2\nu)}{2(1+\nu)}\left(\eta_{ik} - \frac{1}{3}\delta_{ik}\eta_{ll}\right)^2 + \frac{1}{2}B\eta_{ll}^2. \tag{4.37}$$

The indexes i, k, l label the x, y, z coordinates, and ν is Poisson's ratio. Thus the total stress along z is

$$\sigma_{33} = 3B\frac{1-\nu}{1+\nu}\eta_{33} - 3B\alpha\Delta T, \tag{4.38}$$

and equations of elasticity are

$$\rho\frac{\partial^2 u_3}{\partial t^2} = \frac{\partial \sigma_{33}}{\partial z}, \tag{4.39}$$

$$\eta_{33} = \frac{\partial u_{33}}{\partial z}, \tag{4.40}$$

where u_3 is displacement along z, and ρ is the density. The surface is initially at rest and free to move, while the strain is zero everywhere when $t = 0$. With these boundary conditions, the solution for the strain is [11]

$$\eta_{33}(z,t) = \frac{\alpha Q}{A\zeta C}\frac{1+\nu}{1-\nu}\left[e^{-z/\zeta}(1-\frac{1}{2}e^{-vt/\zeta}) - \frac{1}{2}e^{-|z-vt|/\zeta}\mathrm{sgn}(z-vt)\right], \tag{4.41}$$

with longitudinal speed sound v expressed as

$$v^2 = 3\frac{1-\nu}{1+\nu}\frac{B}{\rho} \tag{4.42}$$

The solution for strain in eq.4.41 can simply be viewed as a superposition of thermal expansion η_s (first part of solution which is static and not propagating) and two traveling waves η_+, η_- (second part of solution). One traveling wave is along the positive axis determined by the surface normal and the other is along the negative of the sample normal, propagating at the longitudinal speed of sound. At $t = 0$, strain from thermal expansion cancels the sum of the two propagating strains, owing to the zero stress. Because the static thermal strain is an expansion, the two propagating strains are compression strains initially from boundary conditions. The negative-propagating strain η_- travels toward the free surface and flips its phase, becoming an expansion due to the mismatch of impedance, i.e. $Z_s > Z_{air}$, and then traveling toward the substrate. The positive propagating strain η_+ travels toward the substrate and reflects back. When it reflects, the phase flips if the acoustic impedance of the substrate is smaller than that of the film ($Z_s < Z_f$). Otherwise, the reflected strain retains the same phase and becomes negative propagating as it reflects. The propagation of an acoustic pulse in the film is simulated as shown in Fig. 4.2.

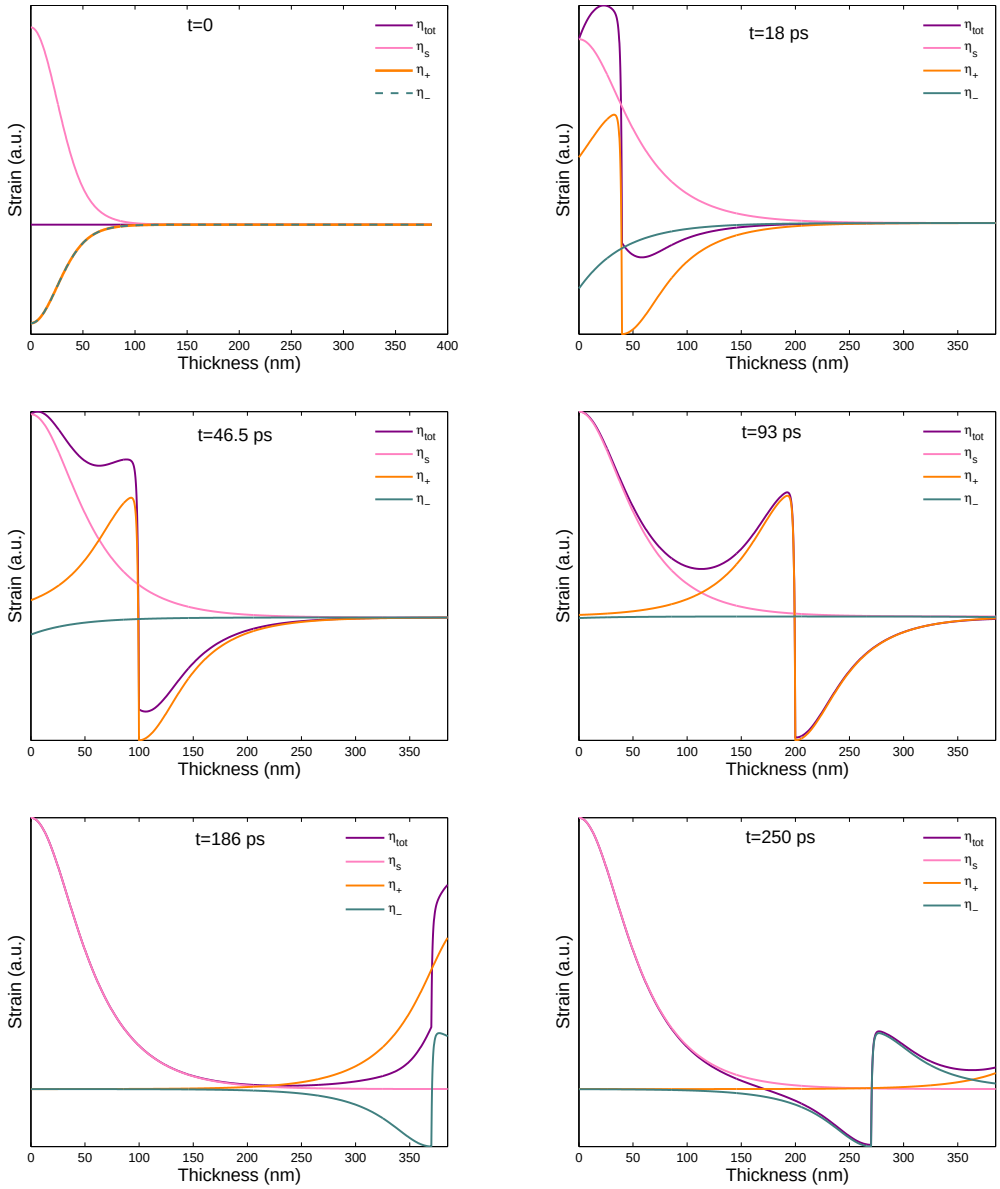

Figure 4.2: Simulation of thermal strain profile evolving as a function of time delay including the effect of carrier diffusion and recombination but not including thermal diffusion. The parameters used here are ζ=15 nm, film thickness 385 nm, speed of sound 2150 m/s, carrier diffusivity 22 cm/s, lattice thermalization time 0.8 ps, and recombination time constant 14 ps. η_{tot} is the summation of static thermal strain, η_+ is positive going strain, and η_- is negative going strain. Reflection coefficient from interface of substrate and film is 35% without phase change here. At t=186 ps, the strain is reflected from the film/substrate interface.

The strain η_{33}, is based on the assumption that heating is instantaneous and thermal profile does not diffuse. In a more general case, a thermal gradient leads to thermal diffusion, and temperature profile changes as a function of time, becoming more homogeneous. Conceptually, the change in thermal profile, i.e. $\Delta T(z) = T(t = t_2, z) - T(t = t_1, z)$, can be viewed as a new source that generates new propagating strains η'_R, η'_L. The instantaneous strain at t_2 is the sum of three components: thermal strain that has diffused between t_1 and t_2), the two strains η_+, η_- at t_1 that have been propagating for $\Delta t = t_2 - t_1$, and the two strains η'_+, η'_- newly generated by $\Delta T(z)$. Therefore, the sharp edge of the positive-propagating strain becomes more smooth, due to the thermal diffusion that produces expanded η'_+ and η'_- from negative $\Delta T(z)$. The negative propagating strain flips as reflects from free surface, becoming an expansion, which experiences no smear-out effect. This is shown in Fig. 4.3. Thermal diffusion is a relatively slow process, which can be ignored in materials where thermal diffusivity is much less than the product of speed of sound and laser penetration depth, i.e. $D_{th} \ll v\zeta$, as shown in the upper and the middle panels of Fig. 4.3.

The analytical solution for strain assuming instantaneous heating, including thermal diffusion, is

$$\eta_{33} = \frac{\alpha Q}{A\zeta C}\frac{1+\nu}{1-\nu}F(z - vt), \tag{4.43}$$

where $F(z,t)$ for $z > vt$ is

$$F(z - vt) = -\frac{1}{2}e^{-(z-vt)/\zeta} - \frac{1}{2}\int_{0^+}^{\infty} dt' \int_0^{\infty} dz' \frac{\partial \Theta}{\partial t'}\delta(z' - z + v(t - t')), \tag{4.44}$$

or for $z < vt$ is

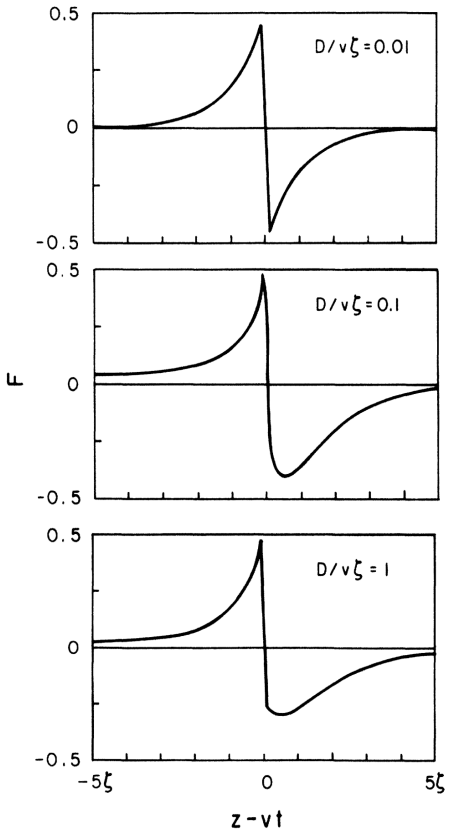

Figure 4.3: Thermal diffusion effects on the shape of thermal strain for various condition. Figure is adapted from Ref. [11].

$$F(z-vt) = -\frac{1}{2}e^{-(z-vt)/\zeta} - \frac{1}{2}\int_{0^+}^{\infty} dt' \int_0^{\infty} dz' \frac{\partial \Theta}{\partial t'}[\delta(z'-z+v(t-t')) - \delta(z'+z-vt(t-t'))]. \tag{4.45}$$

Here $\Theta(z,t)$ is

$$\Theta(z,t) = \int_{-\infty}^{\infty} dz' \frac{1}{\sqrt{4\pi D_{th} t}} e^{-(z-z')^2/4D_{th}t} e^{-|z'|/\zeta}, \tag{4.46}$$

which is a function taking thermal diffusion into account such that

$$\Delta T(z,t) = \frac{Q}{A\zeta C}\Theta(z,t). \tag{4.47}$$

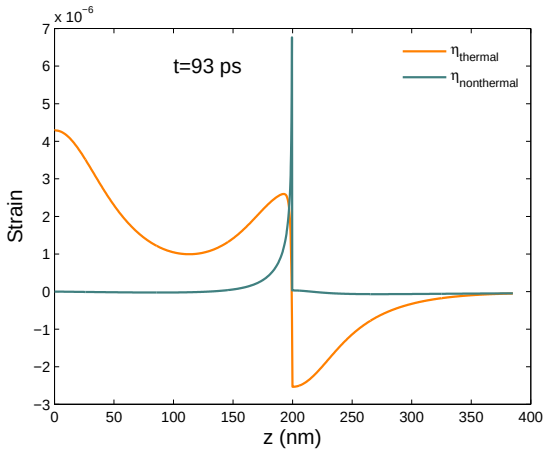

Figure 4.4: Comparison between thermal strain generated from lattice heating and non-thermal strain generated from deformation potential at t=93 ps after laser excitation. Parameters are used as in Fig. 4.2. The strain to carrier coupling is $d\eta_{33}/dn_e$=0.72 for Bi [53].

If, however, heating is not instantaneous and carrier recombination transfers energy to the lattice after laser excitation at $t = 0$, the thermal profile evolves faster since carrier recombination is usually faster than thermal diffusion. In this case, the strain becomes broader than the laser penetration depth ζ. Moreover, if carriers cool while diffusing and before recombination, the width of the acoustic pulse will be dominated by the carrier cooling which contributes energy to lattice heating. The strain propagation of Fig. 4.2 includes both carrier cooling and recombination, so that the width of the acoustic strain is wider than laser penetration depth ζ.

The above discussion concerns strain generation due to thermal expansion. Alternatively, the sudden increase of photoexcited carriers can also launch the acoustic pulses (non-thermal strain) by changing the deformation potential. The increase in free carrier density leads to expansion or compression of the lattice depending on the sign of the coupling constant. The sudden lattice expansion/compression also sets up the stress and modifies the corresponding elasticity equations. The main

difference between thermal strain and non-thermal strain is the generation source, and the corresponding coupling constants between sources and strains are $d\eta/dn$ and $d\eta/dT$. Generally, the carrier diffusion is much faster than the thermal diffusion , i.e. $D_{th} \gg v\zeta$. The non-thermal strain generated by deformation potential coupling alters the bi-polar profile in a manner similar to, but more pronounced than, the effect of thermal diffusion shown in Fig. 4.3. The non-thermal strain displayed in Fig. 4.4 is generated from the increase of carrier density using the same parameters shown in Fig. 4.2. Fig. 4.4 is a comparison between thermal strain generated from lattice thermal expansion and non-thermal strain due to the change of deformation potential.

From the above discussion, strain can be generated both from thermal expansion and from change in deformation potential that couples photoexcited carriers to strain. These two generation sources can modify the shape by thermal diffusion, carrier diffusion, carrier cooling and carrier recombination. Therefore, the strain contains information about early dynamics of carriers.

CHAPTER V

X-ray Techniques

X rays are a type of electromagnetic (EM) radiation waves, similar to optical light but with much higher energy per photon and much shorter wavelength ∼10 - 0.1Å. Because of their short wavelength, x rays can penetrate deep in many light materials and have important applications in medical treatments. In addition, there have been many technical applications of x rays both in daily life (e.g. airport security scan) and research studies (e.g. structure studies of solids and proteins).

One of many important techniques is x-ray diffraction. X-ray diffraction has long been used to study structures of solid state and proteins, resulting in several Nobel prizes. Any crystalized structure with some periodicity, either single or poly crystal, can be investigated by X-ray diffractions. From the diffracted pattern, the crystallography can be reconstructed. Hard x rays (photon energy E_{ph}∼10 keV-100 keV) have a short wavelength comparable to atomic distance in materials. Deep penetration and high sensitivity to lattice spacing make them an ideal tool for studying heterostructures, which are a composite of more than two materials. One material embedded under a second or sandwiched by two other materials usually cannot be detected directly by most non-x-ray methods. Even for non-contact laser techniques, the long wavelength and short penetration/skin depth limits the region of material

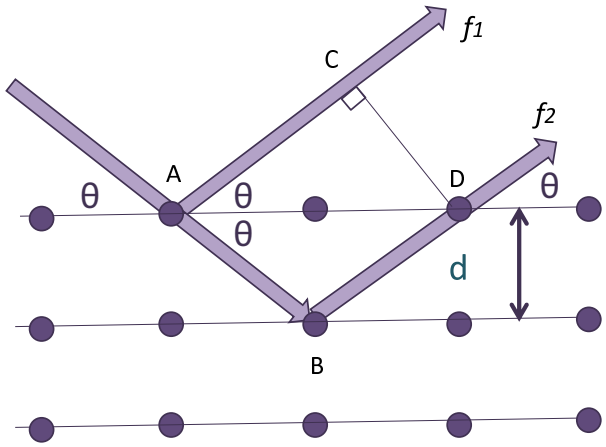

Figure 5.1: Macroscopic and kinematic Bragg diffraction. The path difference between f_1 and f_2 is **AB**+**BD**-**AC**. When the path difference is equal to an integer multiple n of incident wavelength, i.e. $n\lambda$ n=1,2,3..., constructive interference forms. Simple geometry gives that $2d\sin\theta = n\lambda$.

that can be studied.

X-ray Bragg diffraction was first proposed by William Lawrence Bragg. When absorption is not taking into account, x-ray diffraction is often referred to as Bragg diffraction. Bragg's law gives a condition for x rays scattered by atomic lattice planes to interfere constructively:

$$2d\sin(\theta) = n\lambda, \tag{5.1}$$

where d is lattice spacing, θ is incident angle with respect to sample surface, and λ is the wavelength of incident x rays. When x rays hit the atoms, the electronic clouds move and reradiate EM waves with the same frequency. These waves interfere with each other constructively or destructively. Bragg's law can be presented as a simple cartoon in Fig. 5.1.

For a fixed wavelength of x rays hitting certain atomic planes with lattice spacing d, only certain angles meet the condition of eq.5.1. If lattice spacing changes, the

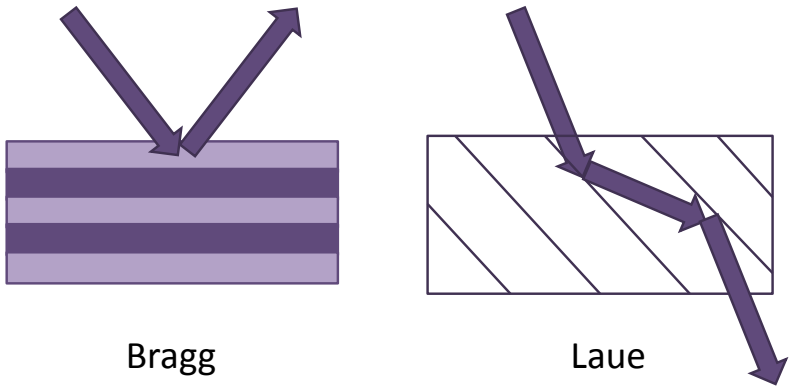

Figure 5.2: X-ray diffraction in two geometries. Depending on the diffracting plane, incident x rays may or may not exit on the same side of the sample.

incident angle should also change in order to satisfy Bragg's law. This sensitivity to lattice spacing offers great potential for x rays to study the dynamics of lattice structure.

There are two geometries for diffraction, Bragg geometry and Laue geometry. If diffraction happens with incident and exit x rays on the same side of the sample, it is Bragg geometry. Otherwise, it is Laue geometry. The diffraction in Laue geometry also follows the Bragg condition. However, it may undergo Bragg reflection between the atomic planes many times before it leaves from the other side. Real crystals with finite thickness have certain absorption lengths, and the exit x rays in Laue case may or may not be a strong diffraction. When absorption is strong, the x rays can be mostly absorbed before they exit the crystal, unless the incident beam meets the Bragg condition and condition for anomalous transmission (Borrmann effect) [13]. If the absorption or diffraction is strong, the dynamical x-ray diffraction theory should be applied [13], although in this dissertation, the kinematical diffraction is sufficient for analysis. The different geometries are shown in Fig. 5.2.

When ultrafast lasers are used to instantaneously excite a material, the electronic structure changes and the excited carriers carry energy from the absorption of photons. When this energy relaxes through complex scattering processes, most of the energy is transferred to the lattice within a few picoseconds if the processes are non-radiative. The lattice becomes hot and expands, increasing the lattice constant. Because of their sensitivity to lattice constant, x rays become very useful to detect lattice dynamics after laser excitation. Many experiments use time-resolved x-ray diffraction to study lattice dynamics from photo-excited material for time-scales ranging from sub-femtosecond to nano-second scale [1, 9, 54, 55, 56, 57, 58].

In this chapter, I introduce the application of x-ray diffraction to thermal transport. Starting with the experiment x-ray source, I discuss several methods of x-ray methods that are applied to my measurements. The film thickness is measured by the x-ray reflectivity, which is a critical parameter to determine many other parameters especially in transport studies. The combination of time- and depth-resolved diffraction overcomes the disadvantage from limited penetration depth of laser techniques. Since the depth-resolved diffraction requires grazing incident x rays, I discuss the grazing incident geometry and the related x-ray beam characteristics.

5.1 Synchrotron source of APS

For lab-based x-ray sources, electrons are produced from a heated cathode and accelerated through a short distance (vacuumed) between cathode and anode. With high voltage in between, electrons can accelerate to high enough energies to ionize inner-shell electrons from the anode. If inner-shell electrons are removed, the atom becomes unstable, and outer-shell electrons fall into the hole left by the removal of inner-shell electrons. When this happens radiatively, x rays are produced with energy

equal to the difference of inner and outer shell states. However, the efficiency of removal of inner-shell electrons is low, and most energy goes to excite the outer-shell electrons, which return to their normal states accompanied only by heat production.

Compared to lab-based x rays, synchrotron based x rays are more efficient and have higher brightness (the source power per unit area and per unit solid angle) for more applications in research. Advanced Photon Source (APS) [59] in Argonne National Laboratory is a third-generation synchrotron based x-ray source. The facility contains a linear accelerator, booster synchrotron, electron storage ring, insertion device, and experimental halls. The linear accelerator is composed by alternating high-voltage electric fields, and accelerates electrons produced from a heated cathode up to 450 MeV. With this much energy the electrons are traveling at relativistic velocities. The booster synchrotron accepts electrons injected from the linear accelerator and boost them to 7 GeV. The electrons then circulate along the storage ring, composed by more than a thousand electromagnets. Inside the storage ring, small-size and low-divergence electron beams are produced. In APS there are 40 straight sections/sectors arranged around the ring. Electron injection and radio frequency equipment make up five of the sectors. The measurements in this dissertation were done in Sector 7, one of the insertion devices with an undulator. The undulator has alternating dipole magnets, which cause electrons to oscillate and radiate, producing x rays.

There are three common synchrotron radiation forms: bending magnet, undulator, and wiggler radiation [60]. The radiation from bending magnets has a broad spectrum but relatively low brightness, and the energy range of the photons does not include much hard x-ray radiation. The radiation from undulator has narrow spectrum, high brightness and partial coherence. Wiggler radiation has high pho-

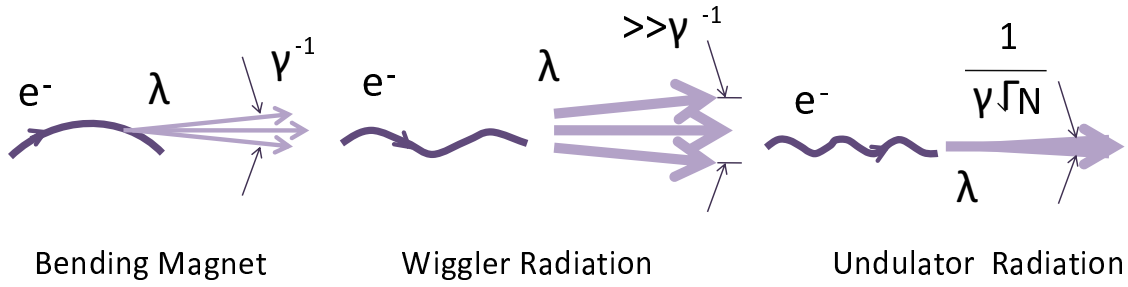

Figure 5.3: Three common radiation forms. The arrows are x rays and the spread of arrows is a cartoon of spectrum. The brightness is expressed as thickness of arrows.

ton energy, broadband spectrum and high photon flux. Both bending magnet and wiggler radiation have broadband spectra, but wiggler has a much higher photon flux. For bending magnet there is a high energy cutoff, depending on the electron beam energy and radius of curvature. In each radiation form, relativistic electrons undergo different trajectories and radiate as illustrated in a simple cartoon in Fig. 5.3. Radiation wavelength is denoted as λ_r, and γ=$1/\sqrt{1-v^2/c^2}$ where v is the velocity of electrons and c is speed of light.

In undulator radiation for example, the undulator has N alternating magnet dipoles with period $\lambda_{\rm und}$. In the electrons' moving frame, they experience λ'=$\lambda_{\rm und}/\gamma$ oscillation with bandwidth $\Delta\lambda'/\lambda'$=1/N (transform limited). In the observer's frame with an angle θ from the electrons' direction of motion, due to the Doppler effect the radiation wavelength becomes $\lambda = \lambda'\gamma(1 - v/c\cos(\theta))$. With small θ it is approximately equal to

$$\lambda \sim \frac{\lambda_{\rm und}}{2\gamma^2}(1+\gamma^2\theta^2), \tag{5.2}$$

so that slightly off-angle observers will see longer wavelength. When θ is at 0, observer sees $\lambda = \lambda_u/2\gamma^2$. An illustration of an undulator is shown in the upper panel of Fig.

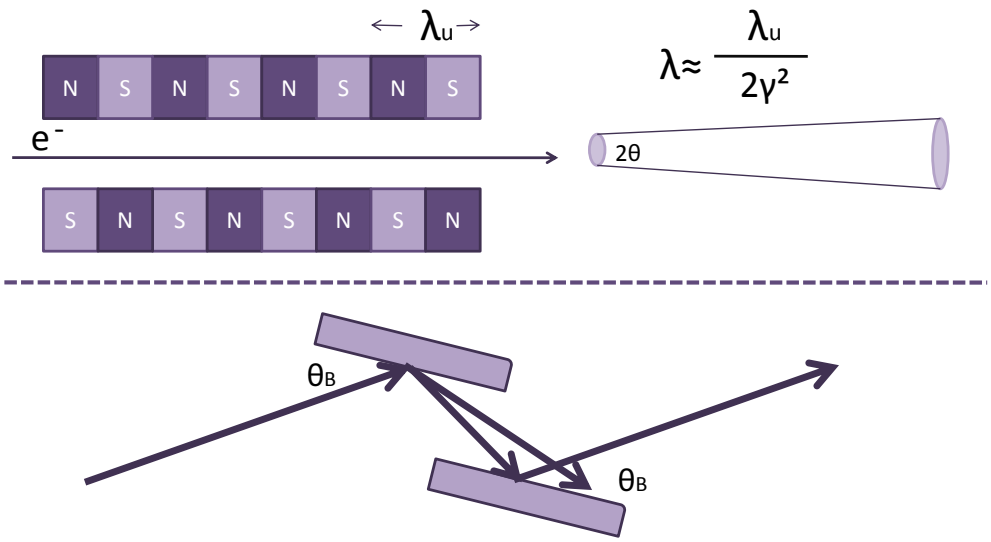

Figure 5.4: Cartoon of undulator and a pair of monochromators. The upper panel is the alternating magnet dipoles with period λ_u. The radiation wavelength at θ=0 is $\lambda_u/2\gamma^2$. The lower panel is a pair of diamond crystals. Polychromatic incoming x ray comes in angle θ_B and diffracts at various angles. The second parallel crystal only allows the dispersed x rays at θ_B to diffract again and exit with the angle θ_B. Thus the exit x rays become monochromatic with very small energy spread.

5.4.

Eq.5.2 assumes small magnetic field strength, **B**. When **B** is increased it affects the orbit of electrons so that the wavelength is increased:

$$\lambda \sim \frac{\lambda_{\rm und}}{2\gamma^2}(1+\gamma^2\theta^2+\frac{\rm K^2}{2}), \tag{5.3}$$

where $\rm K = e\mathbf{B}\lambda_\mu/2\pi mc$. Thus the wavelength can be tuned by varying the gap.

In Sector 7 at APS, a pair of diamond monochromator is used to further select the wavelength. Depending on the application of experiments, polychromatic or monochromatic beams may be required. Polychromatic beams contain x rays with a certain energy range while monochromatic beams have a very small energy spread. In Sector 7, $\Delta E/E$ is on the order of 10^{-4}. Monochromators are based on the idea of Bragg diffraction. As incoming polychromatic x rays hit the crystal with an angle

θ_B, different wavelengths diffract at various angles. A parallel second crystal allows the diffracted radiation with angle θ_B to diffract again, and the beam returns to its original direction as displayed in the lower panel of Fig. 5.4.

Depending on the requirement of different experiments, Sector 7 is equipped with a KB (silicon) focusing mirror to focus beams in the vertical, or horizontal direction, and slits in the upstream or downstream detector arm can either increase the angular resolution or increase the coming flux.

5.2 X-ray techniques

This section introduces some useful techniques for structural determination as well as a basic theorem on x-ray reflectivity. X-ray reflectivity can measure film thickness. The time-resolved x-ray diffraction subsection discusses the timing scheme between x-ray and laser pulses. The asymmetric x-ray diffraction subsection mainly discusses the grazing incident case. It covers the difference in beam profile between incident and exit beams when x rays enter a sample at a very shallow angle. A simple diagram is introduced for the aid of understanding.

5.2.1 X-ray reflectivity

X-ray reflectivity is a useful tool for thin film studies and characterizations. The reflectivity is usually performed at low incident x-ray angles so that the x rays mainly detect the upper layer of the sample due to small extinction depth at small incident angle. Here, I combine Batterman's [13] and Gibaud's [14] approaches to give a simple overview of x-ray reflectivity.

If a Fourier series is used to express electron density at any point $\mathbf{r}$ in a crystal

and sum is taken over the reciprocal lattice, the electron density becomes

$$\rho(\mathbf{r}) = \frac{1}{V}\sum_{H} F_H \; e^{-2i\pi\mathbf{H}\cdot\mathbf{r}}. \tag{5.4}$$

The vector $\mathbf{H}$=(hkl) is the reciprocal vector, V is the volume of the unit cell and F_H is the structure factor that can be conversely written as

$$F_H = \int_{\mathrm{V}} \rho(\mathbf{r}) \; e^{2i\pi\mathbf{H}\cdot\mathbf{r}} dv. \tag{5.5}$$

If atoms are treated as rigid bodies without thermal vibration, the structure factor becomes

$$F_H = \sum_{n} f_n \; e^{2i\pi\mathbf{H}\cdot\mathbf{r}_n}, \tag{5.6}$$

where n is over all atoms in the unit cells. For electric displacement vector $\mathbf{D}$ with electric field $\mathbf{E}$, charge e, and amplitude of the induced electron motion x, the dipole moment $\mathbf{P} = \rho(\mathbf{r})ex$ is related to electric displacement as $\mathbf{D} = k\epsilon_0\mathbf{E} = \epsilon_0\mathbf{E} + \mathbf{P}$ and the dielectric constant is k=$1 + \mathbf{P}/(\epsilon_0\mathbf{E})$. Treating the electric field as a sinusoidal amplitude with frequency ω_0 acting on an electron cloud with density $\rho(\mathbf{r})$, the electric displacement is $x = e\mathbf{E}_0/m(\omega^2 - \omega_0^2)$ with ω being frequency of the electrons. Using eq.5.4 and considering hkl= 0 0 0, the dielectric constant k_0 is

$$k_0 = 1 - \Gamma(\mathrm{F}_0' + i\mathrm{F}_0'') = 1 - \Gamma\sum_{n}(f_0 + f_0')_n - i\Gamma\sum_{n}(f_0'')_n, \tag{5.7}$$

where f_0 is the atomic scattering factor with corrections due to resonance f_0' and absorption f_0'', and $\Gamma = r_e\lambda^2/\pi/V$ with $r_e = 2.813\times10^{-6}$ nm being the classical radius of an electron. Because this is a zeroth order approximation, eq.5.7 is the expression for the average value of the dielectric constant. In a non-magnetic medium, the x-ray index of refraction can be written as [14]

$$\mathrm{n} = \sqrt{k_0} = \left(1 - \Gamma\sum_{n} \; f_0 + f_0' + if_0''\right)^{1/2} = 1 - \delta - i\beta \tag{5.8}$$

with

$$\delta = \frac{r_e}{2\pi}\lambda^2 \sum_n \frac{f_0 + f_0'}{V} = \frac{r_e}{2\pi}\lambda^2 \rho \tag{5.9}$$

and

$$\beta = \frac{r_e}{2\pi}\lambda^2 \sum_n \frac{f_0''}{V} = \frac{\lambda}{4\pi}\mu \tag{5.10}$$

where

$$\mu = \frac{2\pi}{\lambda}\Gamma f_0'' \tag{5.11}$$

is linear absorption coefficient and is related to the imaginary part of the average dielectric constant.

From eq.5.8 the index of refraction n is lower than 1, since δ as well as β are both positive. The incident x rays can undergo total external reflection with a critical angle θ_c relative to the surface, derived from Snell's law

$$\cos\theta_c = \mathrm{n} = 1 - \delta. \tag{5.12}$$

Since n is slightly smaller than 1 and the critical angle is very small, using Taylor expansion to the lowest order of θ_c we can get

$$\theta_c \simeq \sqrt{\frac{r_e\lambda^2}{\pi}\rho}. \tag{5.13}$$

For specular reflection of x rays incident onto a flat medium with uniform electron density, the reflectivity at various incident angles can be defined as $\mathrm{R}(\theta) = I(\theta)/I_0$ with incident intensity I_0. As angle increases, the transmission increases, and thus the reflectivity only is strong for small incident angles. From the Fresnel relationship, reflectivity $\mathrm{R}(\theta)$ is

$$\mathrm{R}(\theta) = \left| \frac{\theta - \sqrt{\theta^2 - \theta_c^2 - 2i\beta}}{\theta + \sqrt{\theta^2 - \theta_c^2 - 2i\beta}} \right|^2 . \tag{5.14}$$

From eq.5.14, reflectivity decreases as incident angle increases for a flat medium. This can be observed in the reflectivity measurement of Bi grown on sapphire with

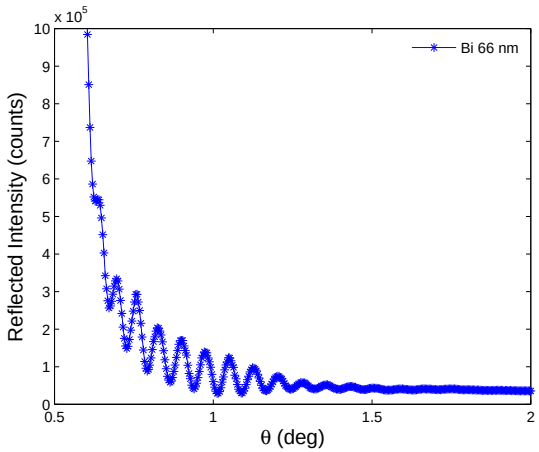

Figure 5.5: Reflectivity measurement for Bi film at 7 keV. The background intensities decrease as angle increase. The oscillation is due to the interference from the beam reflected from Bi surface and interface of Bi/sapphire.

66 nm film thickness, shown as the background intensities without oscillations in Fig. 5.5.

For x rays incident onto a multi-layered flat medium, the reflected beam from different interfaces can interfere with each others. If $k_{z,j}$ is defined as the wave vector in the z direction (along sample normal) of an electric field in the j layer, the reflection amplitude of the electric field from layers 0 to layer 1 (shown in Fig. 5.6) can be derived by treating electromagnetic waves with appropriate boundary conditions, yeilding

$$r_{0,1} = \frac{k_{z,0} - k_{z,1}}{k_{z,0} + k_{z,1}}. \tag{5.15}$$

If there is an interface between layers 1 and 2, the transmitted light can reflect from 1/2 interface shown as Fig. 5.6, causing interference with the reflection from the 0/1 interface. By transform matrix calculations [14], the reflection coefficient for the combined reflection from two interfaces 0/1 and 1/2 is

$$r = \frac{r_{0,1} + r_{1,2}\exp^{-2ik_{z,1}h}}{1 + r_{0,1}r_{1,2}\exp^{-2ik_{z,1}h}}, \tag{5.16}$$

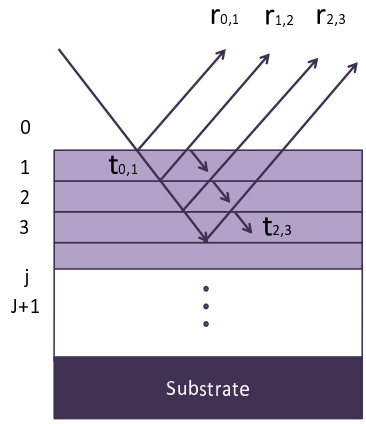

Figure 5.6: Illustration of several interfaces and x-ray interference. $\mathbf{r}_{i,j}$ and $\mathbf{r}_{i,j}$ are reflection and transmission between medium i and j.

with h being the thickness of layer 1. The constructive interference happens when $2k_{z,1}h = 2\pi p$. Since $\overrightarrow{k}_{1,in}$- $\overrightarrow{k}_{1,ref} = 2k_{z,1} = q_{z,1} = 2\pi/h$, thus

$$2\pi p = 2k_{z,1}h = q_{z,1}h \tag{5.17}$$

for constructive interference.

For flat surface, eq.5.14 gives the reflectivity of x rays as a function of incident angle. Reflectivity at angles higher than the critical angle drops dramatically. For a thin film on a substrate, the reflections from the surface and from the interface interfere with each other, and the film thickness can be determined by the period of the interference pattern. For very small angles, $\Delta\theta$ can be approximated as

$$\Delta\theta \approx \frac{\lambda}{2h\cos\theta}. \tag{5.18}$$

Film thickness h thus can be calculated from the known period of interference using reflectivity. As film thickness increases, $\Delta\theta$ becomes smaller, and angle resolution is hard to achieve for x-ray diffractometers because the fringes become less and less

distinct. For thick films, other methods are required for determination of thickness, ultrasonic for example.

5.2.2 Time resolved x-ray diffractions

In APS there are 1296 buckets in the ring available to fill with the electrons; not all the buckets are necessary to be filled. The mode running for my experiments is 24 bunches which are filled with equal spacing ($\sim$153 ns apart) around the storage ring $\sim$1.1 km. The revolution of each bunch inside the ring is 271.5 kHz (P_0 frequency); in another words the radio frequency (RF) is $\sim$351.9 MHz. in In 24-bunch mode, the x-ray pulse frequency is $\sim 6.53 \times 10^6$ Hz, a useful value to determine the total counts in photon-counting mode when the detector is not gated. The x-ray pulse duration in APS is about 100 ps. A Ti:sapphire amplified laser used to photoexcite materials is electronically phase-locked to the RF. It usually runs at a 1 or 5 kHz repetition rate. My measurements are mostly performed at a 5 kHz laser repetition rate. The frequencies of x rays and laser are locked by the error signal (352.5 MHz + phase), which is a mixed signal from the laser oscillator as well as RF. The error signal is feedbacked to piezo-stage with a highly reflective mirror to adjust the cavity length. The timing between the x rays and laser can be varied continuously by adding a phase shift in the feedback loop, and selecting the appropriate laser pulse to be amplified. The timing jitter is a few picoseconds, much smaller than the the x-ray pulse duration.

To distinguish x ray pulse to pulse, the detector needs to be fast. For 24-bunch mode, to tell one bunch from another, the detector response should be faster than 153 ns. In Sector 7, avalanche photo diodes (APD) are used in my experiments with rise time about 10 ns; enough to distinguish x-ray pulse trains. For photon-counting

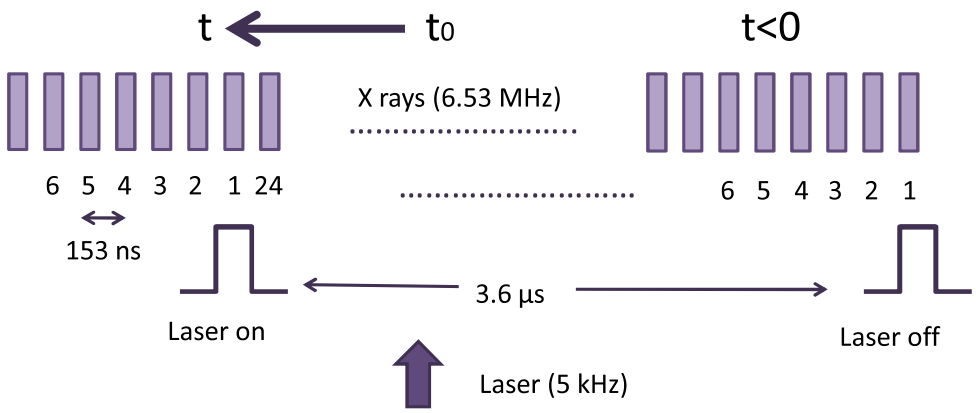

Figure 5.7: Diagram of x ray and laser timing scheme. The upper figure is x-ray pulse trains in 24 bunch mode. The middle figure is cartoon of two gates set to the same x-ray bunch at different times. The lower figure is laser. When laser is coincident with bunch 1 in figure, the time is called time zero.

detection, a threshold is set to the current of the detector to distinguish one or zero photons. The threshold is set in such a way that for a single x-ray pulse hitting the APD detector, the output is counted as one photon. For a non-gated APD detector, photon-counting mode should in principle read all the x-ray pulses, and in 24-bunch mode it reads $\sim 6.53\times10^6$ counts/s, when the probability for detecting at least 1 photon/bunch is $\sim$1.

For time delay between laser pump and x-ray probe, an electronic logical gate is used to determine which x-ray pulse to look at. In my measurements, 4 gates are set. The timing scheme can be understood from a simple cartoon shown in Fig. 5.7. One gate is set to the x rays nearly coincident with the laser pulse while the second gate is set on the same x-ray pulse but one revolution earlier. The third gate is set to the next x-ray bunch, 153 ns later in order to see the dynamics at long time delay. The fourth gate is set one revolution earlier than the third gate. The 1st and 3rd gates are used to detect the signal nearly coincident with the laser pulse and $\sim$153 ns later

than laser pulse. The 2nd and 4th gates are simply one revolution before the 1st and 3rd gates, and detect signals before the laser hits the sample. Because the laser repetition rate is 5 kHz, laser pulse to pulse separation is 200 μs apart. This is long enough for most dynamics in solid state initiated by the laser to recover to original state. Because 2nd and 4th gates are set at the same bunches as 1st and 3rd gates respectively, they can be used as normalizations factor to see the difference between the data with and without laser effects. In addition, any fluctuation from different bunches due to electron injection can be eliminated.

5.2.3 Asymmetric x-ray diffractions

Because x rays normally penetrate deep in materials, good sensitivity to surface layers requires a grazing incident geometry. If incident and exit angles are allowed to be different, the choice of diffraction peaks is more flexible. This is of great help in detecting the dynamics just around laser excitation region. In addition, tuning x-ray incident angle also varies the extinction depth, allowing the dynamics be mapped out through different depths of the medium.

The grazing incident x rays have large cross section on the sample surface. This can make the spacial overlap between laser and x-ray problematic when a small laser spot is required to keep high fluence. If monochromatic x rays are focused, the diffracted signal can be more divergent on the detector than in other geometries. Depending on the geometry, monochromatic x rays with various angular widths of incident beam can be smaller than, larger than or equal to the the angular width of the exit beam. The details of the divergence for the exit beam depend on the collimation and the energy spread of incident beams. Understanding these details is helpful for arranging the experimental geometry between laser and x rays.

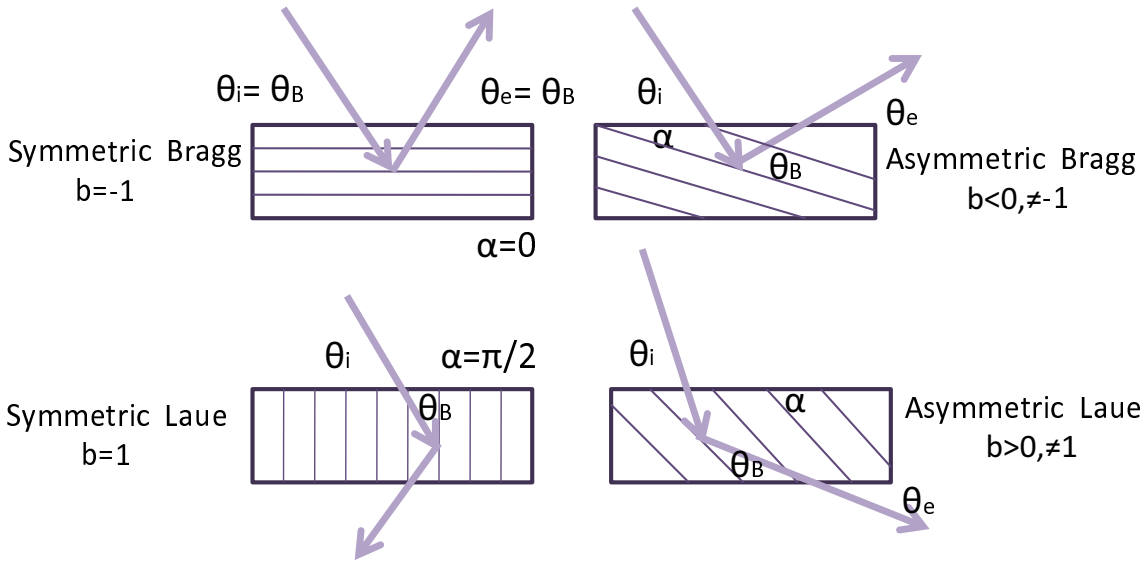

Figure 5.8: Symmetric and asymmetric diffractions in Bragg and Laue geometries. Incident and exit angles are θ_i and θ_e, Bragg angle is θ_B, and α is the angle between surface and atomic plane.

Assuming θ_i is the incident angle of the x ray and θ_e is the exit angle, when $\theta_i = \theta_e$ it is symmetric diffraction. If α is the angle between the diffracting atomic plane and the sample surface, the diffraction is asymmetric for $\alpha \neq 0$ in Bragg case and $\alpha \neq \pi/2$ in Laue case. Shown in Fig. 5.8 for $\alpha \neq 0$, the Bragg angle θ_B corresponding to the diffraction plane can be written as $\theta_B = \alpha + \theta_i = \alpha - \theta_e$. If the crystal is asymmetrically cut, the asymmetry can be characterized as a b factor which is defined as the ratio between directional cosine of incident and diffracted beams with respect to the incident surface:

$$b = \frac{\mathbf{n} \cdot \mathbf{s}_0}{\mathbf{n} \cdot \mathbf{s}_H} = \frac{\sin(\theta_i)}{\sin(\theta_e)} = \frac{\sin(\alpha + \theta_B)}{\sin(\alpha - \theta_B)}, \tag{5.19}$$

where $\mathbf{s}_0$, $\mathbf{s}_H$ are the incident and diffracted beam direction vectors, and $\mathbf{n}$ is the surface normal. Bragg diffraction geometry is the case when b <0, and $b > 0$ corresponds to Laue diffraction geometry. For symmetric Bragg diffraction, b=1 because α=0. Similarly, $b = -1$ is the case of symmetric Laue diffraction. If we define w_i

and w_e as half-width for incident and exit angle of x rays and w_s as half-width for the symmetric case in which $w_i = w_e = w_s$, we have the relation [61]

$$w_e = -bw_i = -w_s|b|^{\frac{1}{2}}. \tag{5.20}$$

The general expression for the angular range of an exit beam for polychromatic x rays with finite angular divergence D_i can be given as

$$D_e = 2|w_i||1 + b| + D_i, \tag{5.21}$$

valid for both Bragg and Laue geometry.

DuMond's diagram [61, 62] shown in Fig. 5.9 is very useful for easy understanding of the relationship between a beam's angular width and divergence schematically. Using the y-axis as x-ray wavelength λ and x-axis as incident angle range, the diagram can be plotted with two parallel lines at 45 degrees near the figure diagonal. The separation of the parallel lines is determined through eq.5.20. An x-ray beam can be represented by an arrow between these two parallel lines. The vertical and horizontal dimensions of an arrow represent, respectively, the wavelength range and the range in incident angle of the beam. For example, a vertical arrow indicates collimated x rays, and a horizontal arrow is a representation of a monochromatic beam. This wavelength versus incident angle plot is referred to as an incidence diagram.

Because x-ray energies are conserved, the same wavelength range should be conserved in the similar exit diagram with x-axis representing exit angle. In the Bragg case, the arrow in the exit diagram starts from the same oblique line as in the incident diagram, pointing to the other line. On the other hand, the exit arrow in the Laue case is oppositely directed between the two lines. Thus from the illustration of Fig. 5.9(a) and Fig. 5.9(d) it is clear that a monochromatic beam preserves the range of angles in symmetric Bragg diffraction ($|b| = 1$). If $|b| > 1$, shown in

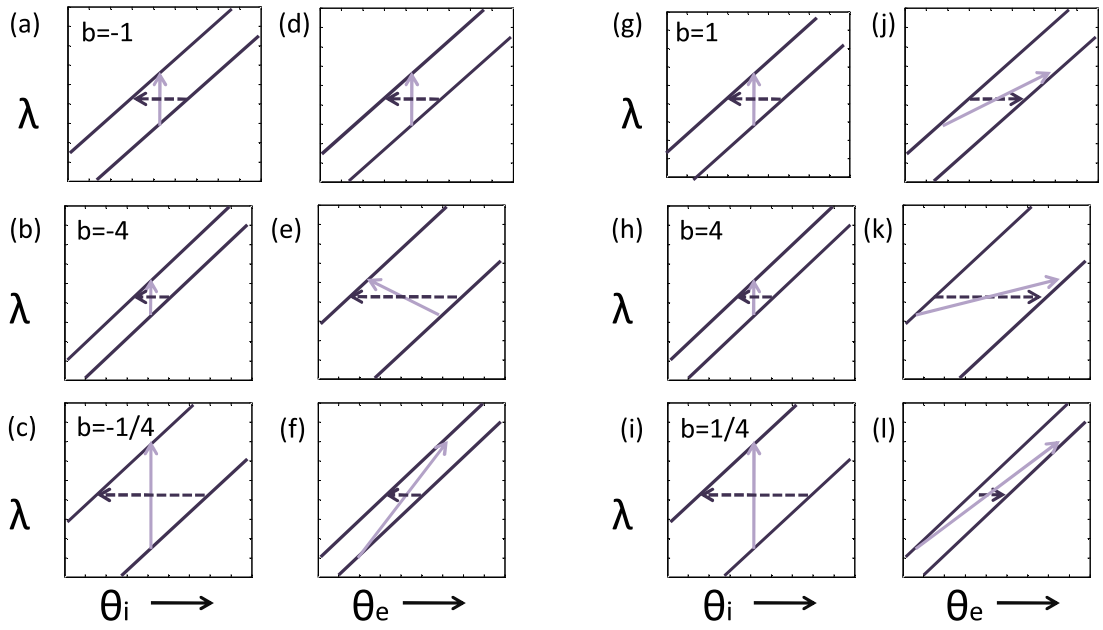

Figure 5.9: DuMond diagram in Bragg case (b<0) and Laue case (b>0). α is the angle between surface and diffraction atomic plane.

Fig. 5.9(b) and Fig. 5.9(e), a monochromatic and less collimated beam exits with increased angular divergence and smaller spatial cross section, to preserve the power of the beam between incidence and exit. For a collimated polychromatic beam with $|b| > 1$, the exit beam disperses. For $|b| < 1$, shown in Fig. 5.9(c) and Fig. 5.9(f), a monochromatic and less collimated (respectively, a collimated polychromatic) beam exits more collimated (more dispersed). For polychromatic but collimated x rays, only symmetric Bragg diffraction preserves collimation. For all $b \neq 1$, asymmetric diffraction results in a dispersed exit beam. A similar method applies to the Laue geometry, with similar results for the monochromatic incident beam. However, for polychromatic x rays in Laue diffraction, whether symmetric or not, the angular dispersion increases in all three cases as shown in the far left column of Fig. 5.9(j)-Fig. 5.9(l).

In some of my experiments, asymmetric Bragg geometry is used with a monochromatic beam. This results in a broader monochromatic exit beam, which reduces the sensitivity to change in Bragg angle. For a fixed angular divergence of the incident beam in Bragg diffraction, the divergence of exit beam can be reduced by using a small magnitude of b factor or small beam width. One way to minimize the angular divergence for the exit beam is to minimize the beam width of the incident beam (this is different from focusing the beam since focused beams always diverges). Another way is to use grazing exit geometry, which can increase the sensitivity to the change in exit angle. In order to probe near surface, a grazing incident or grazing exit geometry is required. However, the grazing incidence has a broader exit beam while the grazing exit has a narrower exit beam, making grazing exit geometry more sensitivity to change in Bragg angle.

CHAPTER VI

Optical Pump-Probe Techniques

Ultrafast lasers are useful tools for studying dynamics of condensed matter. The mode-locked titanium doped sapphire (Ti:sapphire) laser is one of the most common lasers used in optical pump-probe experiments. A high-power continuous laser pumping the Ti:sapphire crystal creates fluorescence with a wide bandwidth ~ 300 nm centered around 800 nm that travels in an open resonator cavity. Ti:sapphire crystal has a short inversion lifetime, ~ 3.2 μs, and high saturation power to give high intensity of peak power. A high reflective output coupler allows a very small amount of light to transmit and leave the cavity. The very broad bandwidth allows very short pulses to be generated. Normally $\sim$ 100 fs for Ti:Shippre is easily to obtained, and some designs can obtain $\sim$ 5 fs with high stability.

Pump-probe experiments using ultrafast laser detect reflection or transmission from a sample. They can study the signal as a function of time by using a controllable delay stage to delay the probe with respect to the pump or to advance the pump with respect to the probe. In order to detect the dynamics upon pump excitation, spatial and temporal overlap of pump and probe are required.

This chapter describes pump-probe technique by the introduction of ultrafast laser oscillators and amplifiers used in the chapter of optical experiments. Following

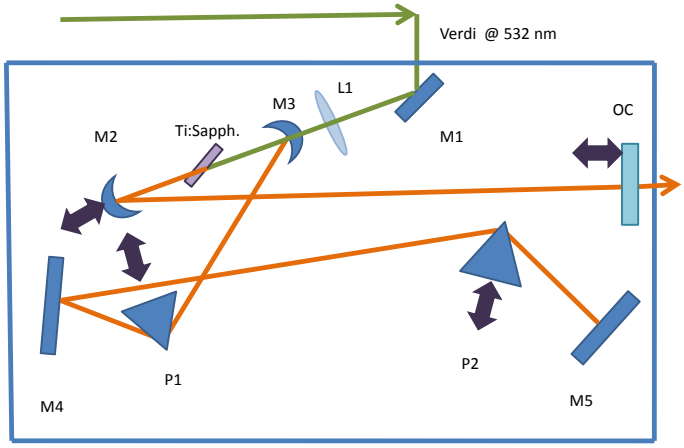

Figure 6.1: The cavity diagram for KM oscillator. OC: output coupler. M1,M4,M5: Mirror. M2,M3: Focusing mirror. L1: Focusing lens. P1,P2:Prism. Ti:Sapph.: Titanium doped sapphire crystal.

that I explain the detection method of the probed signal, i.e. $\partial R/R$, in terms of the change in the dielectric constant, which is in general a function of carrier density, and strains in lattice contributed from optical phonons, acoustic phonons and lattice heating.

6.1 Ti: Sapphire Mode-Locked Oscillator

Displayed in Fig. 6.1, the main cavity or optical resonator of a Ti:sapphire mode-locked oscillator is composed of a Ti:Sapphire crystal as a gain medium. Two end mirrors face each other as M4 and OC in Fig. 6.1. One of the end mirrors, OC, is as output coupler. The light emitted from the crystal travels in the cavity, bouncing back and forth so that interference forms. The constructive standing wave is known as the longitudinal mode of the cavity. The separation of two allowed modes is determined by the cavity length L,

$$\Delta\nu = \frac{c}{2L}. \tag{6.1}$$

The bandwidth of the gain medium determines the number of supported modes in the cavity. If many modes (usually above many thousands) oscillate in the cavity without a fixed phase-relationship, the average output has a constant intensity in a continuous wave called c.w. laser. If the modes oscillate in a fixed phase, they will interfere constructively in a period leading to a burst of pulse. The pulse separation is

$$T = \frac{2L}{c}. \tag{6.2}$$

The bandwidth or number of modes determines the pulse duration. The lower limit of pulse duration is known as the transform limit, and the product of time-bandwidth is at its minimum without chirp, i.e. the frequency does not change over times.

When light travels through materials the frequency becomes chirped, i.e. frequency is time dependent. Whether positive or negative chirp depends on the material light passing through, and a chirp broadens the pulse duration. To compensate for the chirp, an optical element with opposite chirp can be added. Normally, a pair of prisms or grating is added in the cavity for compensation of chirp. Compensation by using a pair of gratings or prisms is also common outside the cavity for pulse compression if many optics are used in the design of the optical path. Fig. 6.1 displays the design of the KM Lab Oscillator. Fig. 6.2 shows the scheme of a pair of prisms as well as gratings.

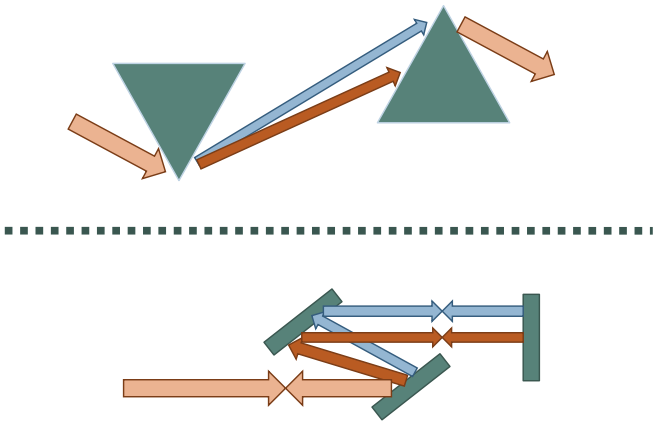

Figure 6.2: Simple illustrations for a pair of prisms and for a pair of gratings for frequency compensation, in upper and lower panel respectively. Center frequency f with width $2\Delta f$ is incident onto the 1st prism. Various frequency components are subject to different index of refraction (dispersion). Between two prisms, various frequencies have trips of different distances. A second prism recovers the spatial overlap of all frequencies and a frequency chirp is produced. A positive chirp corresponds to the increasing instantaneous frequency as a function of time delay. The similar idea applies to a pair of gratings. The different frequencies have different round trips, producing a frequency chirp when the spatial overlap is recovered.

6.2 Regenerative Amplifier

The amplifier receives an input pulse and can generate higher output signal. There are many designs for amplification by pumping a gain medium in the cavity. Experiments at high excitation in this dissertation were performed with a regenerative amplifier.

Pumping the Ti:sapphire crystal (gain medium) with a high power continuous wave (c.w.) laser for some time can store energy. Injecting a seed pulse into a resonator controlled by an electro-optic switch, Pockels cell for example, enables the pulse to travel many round trips in the resonator and be amplified. Using a second electro-optic switch can release the pulse after amplification, and the pulse is usually

amplified to mJ range with one to several hundred kHz repetition rate. An oscillator can serve as a seed pulse, which usually has high repetition rate up to many tens of MHz, e.g. Ti:Sapphire oscillator is normally around a few hundred MHz. Not all seed pulses are injected into the resonator. The selection of seed pulse is controlled by the electro-optics or acousto-optic switch.

Usually before the seed pulse enters the amplifier, it needs to be temporally stretched to avoid damage caused by its high intensity in the amplifier. This requires a very highly dispersive optical element, and usually a pair of gratings does the work. Thus the pulse is stretched with a long time duration to reduce its peak intensity. After pulse amplification, it requires a compression again to become a short duration pulse and to increase its peak intensity. A second pair of gratings with the opposite dispersion from first pair can be used to compress the pulse. This scheme is called chirped-pulse amplification (CPA) [63].

The experiments in this dissertation use Coherent company's amplifier Rega which is seeded by $\sim$ 120 fs pulse from Mira , the Ti:Sapphire oscillator. The pulse switch is controlled by the acousto-optic modulator (AOM), which can control the power, frequency or direction of the incoming pulse. The AOM consists of a transparent crystal attached with a piezoelectric transducer that generates acoustic waves in the crystal using pressure. When a laser pulse propagates through the crystal with a periodic acoustic wave, it experiences Bragg diffraction and slightly changes direction and frequency compared to the transmitted beam. Thus AOM in Rega (cavity dumper) controls the ejection and injection of the pulse in and out of the resonator. Another acousto-optic switch in Rega's resonator, the Q-switch, holds off the spontaneous lasing in the cavity until the seed pulse is injected.

In order to have a stable system of amplification, the seeded pulse needs to have

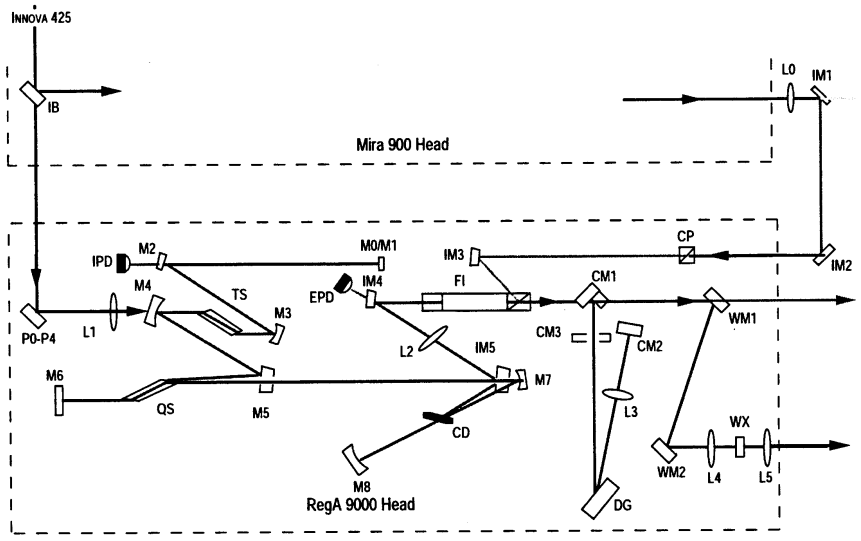

IB:	Ion Beamsplitter	WX:	White-Light Crystal
IPD:	Injection Photodiode	M0 - M8:	Cavity Optics
EPD:	Ejection Photodiode	IM1-IM5:	Injection Optics
QS:	Q-Switch	CM1-CM3:	Compressor Optics
CD:	Cavity Dumper	WM1 - WM2:	Whitelight Optics
FI:	Faraday Isolator	L0 - L5:	Lenses
CP:	Cube Polarizer	P0 - P4:	Pump Optics
DG:	Diffraction Grating	TS:	Ti:Sapphire Crystal

Figure 6.3: Diagram of Rega system, from manual of Rega.

a broad bandwidth and specific center wavelength, i.e. 800 nm in Rega and $\geq$10 nm bandwidth is required from the Mira oscillator. The seed pulse circulates through many round trips in the cavity, and the Q-switch as well as the optical elements cause a large dispersion which stretches the seed pulse to a $\sim$ 40 ps before pulse extraction. Thus, the pulse does not need to be pre-stretched before injection into cavity. The output pulse from the cavity is usually compressed by a pair of gratings which can be tuned to get the various pulse widths. Rega uses a combination of mirrors and a single grating for the pulse compression. By tuning a compensation chirp with opposite sign from that caused in the cavity, the pulse can in principle be made transform-limited. Otherwise, it will have a positive or negative chirp, and the pulse will not be transform limited. Fig. 6.3 shows the optical design of Rega

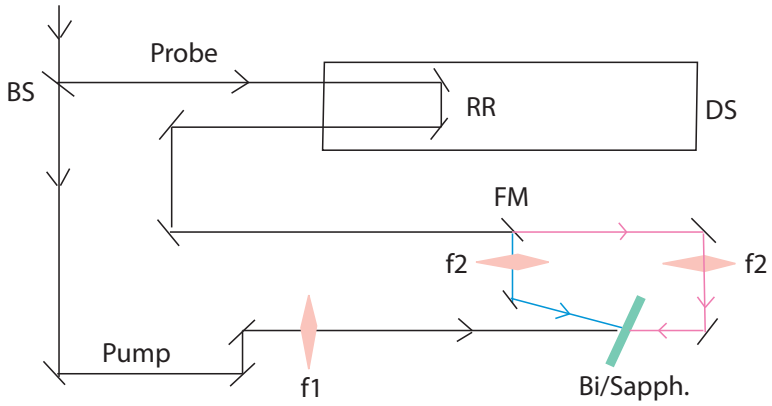

Figure 6.4: Counter-propagating pump-probe geometry which also allows the conventional pump-probe to be performed. BS: beam splitter, RR: retro-reflector, DS: delay stage, FM: flip mirror, f1: focussing lens with 300 mm focal length, f2: focussing lens with 150 mm focal length.

amplifier.

6.3 Pump-Probe Setup

In the study of Bi thin film, I use four pump-probe geometries resulting from the combinations of pump and probe with the two surfaces of the film. The first is a conventional geometry with pump at the film surface and probe at the same surface. The second is a counter-propagating pump-probe geometry with pump at the film surface and probe at the interface of film and substrate. The third is also a counter-propagating geometry as in the second, but with sample flipped so that pump is at the interface and probe is at the film surface. The fourth geometry has pump and probe both at the interface. The geometries of counter-propagating and conventional pump-probe measurements are shown in the Fig. 6.4. Both surface pump surface probe and interface pump interface probe excite and measure from the same site, while surface pump interface probe and interface pump interface probe use counter-propagating beams on opposite faces.

The experiments were performed in a modified Sagnac interferometer-type geometry using counter-propagating beams at room temperature as shown in Fig. 6.4. In the experiments at low excitation range, a KM Lab Ti:Sapphire oscillator is used with 85 fs pulse duration centered at 830 nm with 3 nJ/pulse at ∼85 MHz repetition rate. Approximately 5 % of the pulse energy was used for the probe beam. A mechanical delay stage with retro-reflector controlled the pump-probe delay. Spatial overlap was determined by the interference of pump and probe beam recombined together when the sample was removed. Temporal overlap was determined by second harmonic signal of a (BBO) crystal in place of the sample. The laser diameter was ∼ 1 mm, determined by translating a razor blade along the beam plane before the lens. Pump and probe beams were focused by lenses with 30 cm and 15 cm focal length respectively. This setup also allows conventional surface pump and surface probe experiments to be performed. A lockin amplifier was used for detection at ∼ 1.5 kHz chopping frequency. Each reflectivity data set is reproducible better than 10% error of ΔR/R, and with the 30 ms lockin integration time we are able to measure the signal with accuracy $\sim 10^{-6}$.

At high excitation range, a Rega amplifier is used with similar modified Sagnac interferometer-type geometry for the counter-propagating beams. The output of the amplifier is a ∼4 μJ/pulse with 100 fs pulse duration at 250 kHz repetition rate, and it is focused to about 100×150 μm at half maximum assuming Gaussian profile.

6.4 Probing Reflectivity of Bi

Bi is opaque to the laser wavelength at ∼800 nm with penetration depth ∼ 15 nm estimated from the absorption coefficient at $\hbar\omega \sim 1.55$ eV [64]. The index of refraction for Bi including imaginary part is $n + ik$ =2.6+4i at 800 nm [65]. The

complex dielectric function is

$$\varepsilon = \varepsilon_r + i\varepsilon_i = (n + ik)^2. \tag{6.3}$$

The reflectivity from the interface of Bi and any transparent medium, s, is written as

$$\begin{aligned} R = \left|\frac{\sqrt{\varepsilon} - \sqrt{\varepsilon_s}}{\sqrt{\varepsilon} + \sqrt{\varepsilon_s}}\right|^2 &= \left|\frac{\sqrt{\varepsilon_r + \varepsilon_i} - \sqrt{\varepsilon_s}}{\sqrt{\varepsilon_r + \varepsilon_i} + \sqrt{\varepsilon_s}}\right|^2 \\ &= \frac{\varepsilon + \varepsilon_s - \sqrt{2\varepsilon_s}\sqrt{\varepsilon + \varepsilon_r}}{\varepsilon + \varepsilon_s + \sqrt{2\varepsilon_s}\sqrt{\varepsilon + \varepsilon_r}}. \end{aligned} \tag{6.4}$$

where ε is dielectric function of Bi, ε_s is dielectric function of the transparent medium, ε_r, ε_i are real and imaginary parts of Bi dielectric function, and $|\varepsilon| = \sqrt{\varepsilon_r^2 + \varepsilon_i^2}$. The change in reflectivity due to change in Bi dielectric function is

$$\frac{\partial R}{\partial \varepsilon_i} = \frac{\sqrt{2\varepsilon_s}\varepsilon_i(-\varepsilon_s + 2\varepsilon_r + \sqrt{\varepsilon_r^2 + \varepsilon_i^2})}{\varepsilon\sqrt{\varepsilon_r + \varepsilon}(\varepsilon_s + \varepsilon + \sqrt{2\varepsilon_s}\sqrt{\varepsilon + \varepsilon_r})^2} \tag{6.5}$$

and

$$\frac{\partial R}{\partial \varepsilon_r} = \frac{\sqrt{2\varepsilon_s}(\varepsilon_r^2 - \varepsilon_i^2 - \varepsilon_r\varepsilon_s - \varepsilon\varepsilon_s + \varepsilon\varepsilon_r)}{\varepsilon\sqrt{\varepsilon_r + \varepsilon}(\varepsilon_s + \varepsilon + \sqrt{2\varepsilon_s}\sqrt{\varepsilon + \varepsilon_r})^2}. \tag{6.6}$$

If the transparent medium is air, ε_s=1.

In the photoexcited Bi system, the change in reflectivity is due to a combination of change in free carrier density, lattice expansion or compression (acoustic and optical phonons), and/or change in carrier temperature, so that

$$\frac{\Delta R(t)}{R} = \frac{1}{R}\left[\frac{\partial R}{\partial Q}Q(t) + \frac{\partial R}{\partial n}n(t) + \frac{\partial R}{\partial \eta}\eta(t) + \frac{\partial R}{\partial T_e}\Delta T_e(t) + \frac{\partial R}{\partial T_l}T_l(t)\right], \tag{6.7}$$

where Q is the A_1 coordinate, n is photoexcited carrier density, η is strain, and T_e and T_l are photoexcited carrier and lattice temperature respectively. Ideally,

the coefficients would be determined by experiments individually. These coefficients may not be constant: for example $\partial R/\partial n$ may be a function of the carrier density. Therefore, for a pump-probe measurement which contains all the modulations, the determination of the coefficients is not straight forward. To simplify the problem, the coefficients are usually assumed constant for analysis, unless dramatic differences between the model and data are observed. Special approaches may sometimes help for the derivation of these coefficients, but in general the determination is difficult.

CHAPTER VII

Depth and time resolved X-ray diffraction study of thermal transport

X rays can directly probe change in lattice structures. In addition, tunable probing depth and non-contact nature of x-ray experiments make them a perfect tool for thermal transport study. In the past, I have used symmetric time-resolved x-ray diffraction (TRXD) for thermal conductivity measurements of AlGaAs heterostructure [1]. Highland et al. also combined optical reflectivity and TRXD measurements to extract the interface conductance of an buried layer of $(GaAs)_{(1-x)}(InAs)_x$ [2]. In this chapter, I apply and extend TRXD to the studies of thermal transport in Bi films grown on sapphires.

Both my AlGaAs experiment and Highland's experiments use an ultrafast laser to deposit energy in the form of heat, either to the interface of the heterostructure or to the surface of the transducer. I used two symmetric Bragg diffractions, one from the film and one from the substrate, as two thermometers measuring average temperature of film and substrate separately by use of the relation $\Delta\theta = -\alpha_l T \tan(\theta_B)$ where α_l is the linear expansion coefficient for the film and for the substrate. Fig. 7.1 displays Bragg angle shift as a function of time delay between the x-ray and laser pulses. Because the film is transparent to the laser at 800 nm wavelength, heat

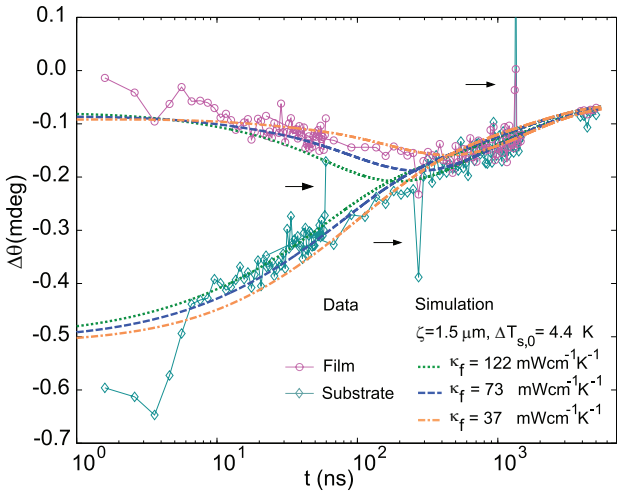

Figure 7.1: Time-resolved Bragg shift for excitation with 0.95 W average power. Data showing the heating and cooling of the film and substrate and comparison with simulations. The arrows indicate periodic coherent acoustic echoes.

is deposited in the substrate from laser excitation and diffuses in both directions toward the film and the bulk substrate. Initially when the temperature gradient is large, the inhomogeneous thermal distribution in the substrate leads to heating in the film and cooling in the substrate via heat conduction. When both temperature distributions of film and substrate are close to uniform with very small gradient, both cool together. With known thermal conductivity of substrate, linear expansion coefficient, and boundary condition, and assuming no interface conductance, I numerically solved the one-dimensional diffusion equation incorporating dynamical x-ray diffraction to derive the diffusion constant of the film, D_f. I extracted the thermal conductivity of $Al_{0.3}Ga_{0.7}As$ using the relation between specific heat and thermal conductivity via $D_f = \kappa_f / C_f$. I also found that temperature profile (from the fit) is broader than laser penetration depth in the GaAs substrate.

Highland et al. deposited heat to a 100 nm Al transducer on a GaAs substrate. They assumed the temperature decay signal from time domain thermal reflectance (TDTR) was due to the heat conduction of GaAs [2]. To produce a different lattice

constant, they doped indium (In) on the top layer of GaAs (GaAs:In) and measured heating and cooling on GaAs:In using TRXD. They established a sensitivity function and claimed that TDTR is more sensitive to the measurement of thermal conductivity, while TRXD is more sensitive to the measurement of interface conductance (Kapitza conductance). They found 20% decrease of interface conductance, suggesting that 20% of the phonons in GaAs:In are ballistic due to a mean free path longer than the film thickness. Those phonons do not carry heat across the interface.

In addition to the above TRXD experiments using symmetric diffraction, in this chapter I discuss experiments in which various Bi films are grown on sapphire substrates, starting with sample characterization. I discuss the characteristic times for thermal conductivity and Kapitza conductance in the simplified case where one or the other effect dominates. For thermal transport studies in heterostructures of films grown on substrates, TRXD is limited in its sensitivity to the various combinations of thermal conductivity and Kapitza conductance. In addition, the sensitivity of TRXD is limited by the x-ray pulse duration. The depth resolved TRXD using asymmetric diffraction shows a non-negligible temperature gradient in the 284 nm thick film but a near-uniform distribution in 65 nm film. I extract the Kapitza conductance in the 284 nm film by numerically solving one dimensional diffusion equation, assuming the literature value for the thermal conductivity. For comparison with the numerical simulation, I use a simple exponential fit for 65 nm film. From grazing incident x-ray measurements, I confirm that the decay of Bragg angle shift from 006 symmetric diffraction is due to the Kapitza conductance. Assuming exponential decay temperature profile, we can find the maximum temperature change upon laser irradiation as well as Kapitza conductance.

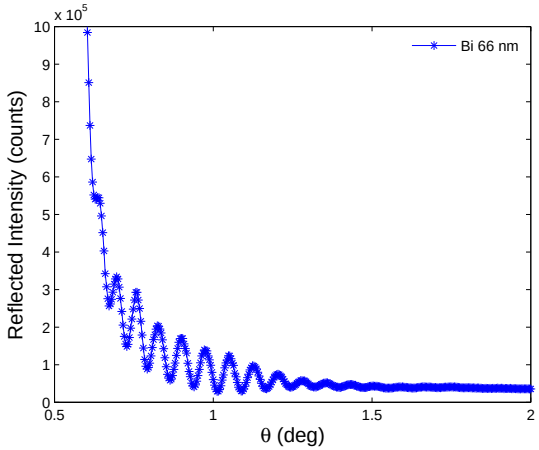

Figure 7.2: Reflectivity measurement for Bi film at 7 keV.

7.1 Film thickness and crystal characterization

Three thicknesses of Bi films are grown on sapphires along the c-axis (001) by molecular beam epitaxy (MBE). From symmetric x-ray 006 diffraction of Bi and sapphire at 9.5 keV energy, it is confirmed that both sapphire and Bi are high-quality single crystals. The full width half maximum (FWHM) of sapphire in a $\theta - 2\theta$ scan is about 1.34 mdeg. About 100 mdeg is seen in Bi $\theta - 2\theta$ scan and no obvious grain boundary is observed. From these measurements, we conclude that both sapphire and Bi are single crystals.

In order to determine the film thickness, we use x-ray reflectivity measurements for film thicknesses below 185 nm, and optical pump-probe measurements for film thickness above 185 nm. From the separation of interference in x-ray reflectivity measurements, the film thickness is derived by eq.5.18, $\Delta\theta \approx \lambda/2h\cos\theta$.

Thus at 7 keV the thickness corresponding to interference with 0.078^{o} period is 65 nm, shown in Fig. 7.2. For thicker films (above 185 nm) the oscillations in the reflectivity are not resolved, so acoustic measurement by optical reflectivity is used instead. The speed of sound $\sim$2150$\pm$100 m/s is measured in 185 nm film (known

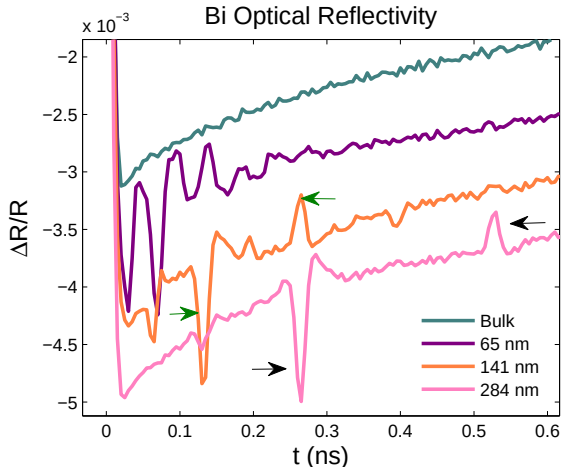

Figure 7.3: Optical pump-probe measurement for acoustic strain and its echoes using dual fiber laser system. Two color set of arrows indicate round trip for two films.

from x-ray reflectivity) using round trip propagation time in optical pump-probe measurements via $v = 2L_{\mathrm{Bi}}/\Delta t$ (with L_{Bi} being film thickness). Shown in Fig. 7.3, round trip propagation time is indicated by the separation between pairs of arrows. From the measured speed of sound, the thicker films are calculated to be 141 $\pm$ 13 nm and 284 $\pm$ 25 nm. 65, 141 and 284 nm are used in the measurements of this chapter.

7.2 Reciprocal lattice scan and Gaussian peak approximation

This section discusses the relation between change in lattice constant and change in reciprocal lattice. Fig. 7.4 displays both static $\theta - 2\theta$ measurement of 006 diffraction and reciprocal l scan near 014 diffraction at α=0.4°, shown at two different time delays between x ray and laser. Any change in the lattice spacing after laser excitation will be mainly due to the change in temperature for the time scale of interest here. The lattice spacing d along the c axis is related to Miller index (hkl) as well as lattice constants a and c:

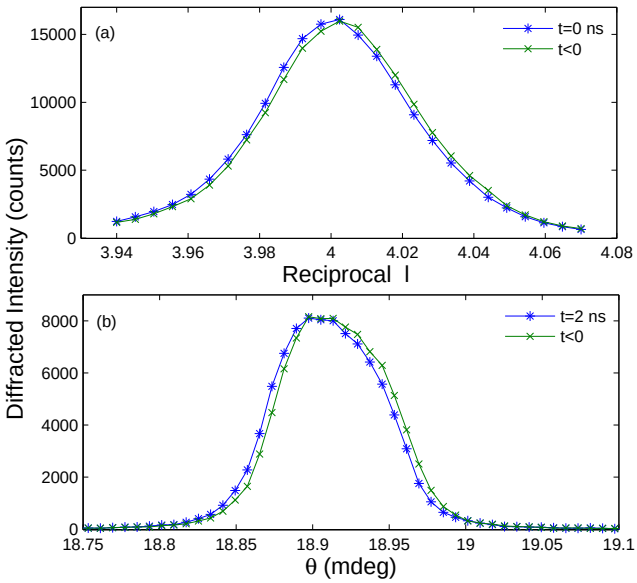

Figure 7.4: X-ray diffraction peaks in symmetric and asymmetric geometries. (a) Reciprocal l versus diffracted intensity of asymmetric 014 diffraction. (b) Angle versus diffracted intensity of symmetric 006 diffraction. Line with ($\times$) marker is conventional x ray measurements without laser effect. Line with (*) marker is simultaneous measurement with laser and x ray near coincident, which is x ray (a) coincident with and (b) 2 ns later than laser irradiation.

$$\frac{1}{\mathrm{d}^2} = \frac{4}{3}\left(\frac{h^2 + hk + k^2}{a^2}\right) + \frac{l^2}{c^2}. \tag{7.1}$$

With some algebra, the change in lattice spacing along the c axis can be expressed as a function of the change in Miller index along the l direction:

$$\frac{\Delta \mathrm{d}}{\mathrm{d}} = \frac{-\mathrm{d}^2}{c^2} \times l\Delta l. \tag{7.2}$$

Gaussian-like x-ray diffracted intensity I as a function of Miller index l can be written as

$$I(l) = \exp((l - l_0)^2/2\beta^2). \tag{7.3}$$

The change in diffracted intensity will be approximately linear with the change in l away from the peak [2]. Thus it can be assumed that the change in diffracted

intensity is linear with change in average temperature across x-ray probe region. It is clear from Fig. 7.4(a) that the change in x-ray diffraction intensity is most efficient around half maximum of the peak, i.e. l=4.02. From eq.7.2 it can be assumed that the change in the diffracted intensity is proportional to the change in average temperature over the probe region. Thus instead of considering the 014 peak as a function of time for the full range of l, we simply measure the intensity at half peak as a function of time.

The asymmetric TRXD measures change in l by positioning the detector at half maximum of the 014 peak at various time delays. The symmetric TRXD measures the full $\theta-2\theta$ as a function of time delay, and the angle shift is the difference between average angle with and without laser effect, weighted by the diffracted intensity.

7.3 Overview of thermal transport studied by TRXD

Since x-ray diffraction is very sensitive to the lattice constant, TRXD is a powerful tool to detect the lattice change as a function of time delay upon laser irradiation. Following lattice heating, a thermal gradient results in heat transport to reduce the gradient, evening the heat distribution. In TRXD measurements, a laser pulse incident on the film has a relative large diameter compared to the film thickness. Thermal transport across the film is thus assumed to occur along the sample normal and is reduced to a one-dimensional problem. Assuming substrate thermal conductivity is known, thermal transport usually involves several distinct parameters: thermal conductivity, Kapitza (boundary/interface) conductance and temperature profile. These parameters are normally correlated in the decay signal. Generally, a sample is designed to measure either thermal conductivity or Kapitza conductance with a known thermal profile [35, 37]. In the case of film grown on a substrate with a high thermal

conductivity, film thermal conductivity plays a major role when the film thermal gradient is large, whereas the Kapitza conductance dominates when thermal profile is nearly uniformly distributed in the film.

The thermal gradient is largest after irradiation by a laser pulse incident onto the sample. The sample redistributes its temperature profile via thermal conductivity, and as temperature becomes nearly uniform, the transport is dominated by Kapitza conductance. Using a thin film with large thermal conductivity, for example, the conditions are optimized for the measurement of Kapitza conductance. However, if the film is thin or has low thermal conductivity, both thermal conductivity and Kapitza conductance contribute to the signal, first by thermal conductivity and later by Kapitza conductance.

Due to the large penetration depth, x rays are capable of probing heterostructures. For the heterostructure of films grown on substrates, the Bragg peaks from the film and substrate can be separated and thus serve as two thermometers to monitor the temperature change separately by detecting the change in Bragg angle via $\Delta\theta = -\alpha_l T \tan(\theta_B)$ [1]. However, for a substrate with relative high thermal conductivity, the bulk conducts heat quickly and the temperature rise is very small near the interface, so that in practice there is only one thermometer from the film. To measure thermal transport with one thermometer, either thermal conductivity or Kapitza conductance should be known, in order to derive the other. X-ray diffraction measures the average temperature of the entire film. If both thermal conductivity and Kapitza conductance are unknown, the fit becomes complex since these two parameters are correlated. Take the Bi grown on sapphire for example and plot temperature profile at various time delays with a given initial temperature rise. The two extreme cases shown in Fig. 7.5 can result in the same measurement when x rays

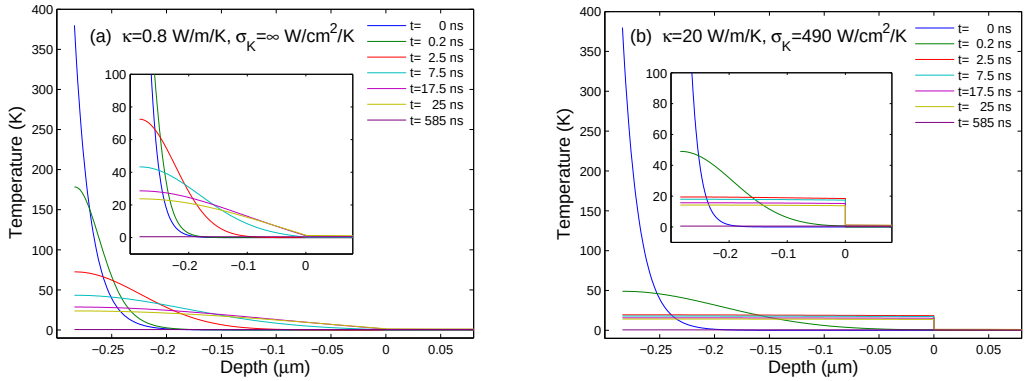

Figure 7.5: Simulations of temperature profiles as a function of depth for 284 nm film at various time delays in the limit of (a) high Kapitza conductance and (b) high thermal conductivity. Initial temperature is an exponential-decay profile with 15 nm penetration depth and maximum temperature rise 380 K. The negative and positive are film and substrate separately with interface located at 0.

probe the entire film and average the temperature distribution.

The challenge of this special case can be overcome by tuning the x-ray incident angles and hence the extinction depths and probe depths. As long as sufficient time resolution is achieved, the two cases can be be distinguished. Thus, grazing incident x-ray diffraction is useful when more than one parameter is unknown.

7.4 Characteristic Time

For limited time resolution, both time and length scales are crucial in the study of thermal transport. For two films of the same material but different thickness, the dominating factor in thermal transport for a given time scale could be different. With the same thermal conductivity, a temperature gradient in thinner film becomes homogeneous more quickly than in thicker film. This characteristic time for homogenization is very important, since if a detector is not fast enough, it misses early thermal conductivity and only sees dynamics that is dominated by Kapitza conductance. For a fast detector that is able to catch signals before the characteris-

tic time, dynamics is first dominated by thermal conductivity and later by Kapitza conductance. The detectors are characterized as fast or slow in comparison to characteristic time of the sample. Since x-ray pulses take snapshots of a dynamic, the time resolution is limited by the x-ray pulse duration.

The above discussion is based on the assumption that the substrate thermal conductivity is large, so that the temperature rise upon irradiation is negligible. If substrate thermal conductivity is small and temperature rise is not negligible, the problem becomes more complex. However, the effect of substrate thermal conductivity is not discussed here since samples can always be grown on a chosen material known to have high thermal conductivity.

The characteristic time due to thermal conductivity can be estimated from the diffusion equation with the appropriate boundary condition. The one-dimensional diffusion equation is

$$\frac{\mathrm{d}T(t,x)}{\mathrm{d}t} = \frac{\kappa}{C}\frac{\mathrm{d}^2T(t)}{\mathrm{d}z^2}, \tag{7.4}$$

where $T(t,x)$ is temperature profile as a function of depth x and time delay t, κ is thermal conductivity, and C is specific heat. For a semi-infinite crystal with an initial delta-function temperature distribution, the characteristic time to for heat to diffuse a distance l_d away from the surface is

$$t_c = \frac{Cl_d^2}{4\kappa}. \tag{7.5}$$

Although this is not the exact solution for the finite thickness case upon laser irradiation, it is good as a rough approximation of characteristic time when thermal conductivity is known.

When thermal profile is close to homogeneous, it is the Kapitza conductance rather than the thermal conductivity which plays the main role in reducing the

thermal energy in the film. Kapitza conductance comes with its characteristic time which can be found using the equation

$$CL\frac{\mathrm{d}T(t)}{\mathrm{d}t} = -\sigma_K(T_f(t) - T_s(t)), \tag{7.6}$$

where L is film thickness, σ_K is Kapitza conductance, and $T_f(t)$, $T_s(t)$ are film and substrate temperature as a function of time. Normally the substrate has relatively large thermal conductivity and no obvious temperature rise occurs; thus T_s can be treated as constant. Therefore, eq.7.6 has decay time constant

$$\tau_{\sigma_K} = \frac{CL}{\sigma_K}. \tag{7.7}$$

This is the characteristic time for Kapitza conductance.

7.5 Limitation and sample manipulation

Although x-ray diffraction is a powerful tool for measuring thermal transport via lattice changes, there is some limitation due to the finite time resolution of x-ray pulses and due to sample itself when more than one parameter is unknown. When time resolution is limited due to long x-ray pulses, even with an aid from various depth probes, some cases are not discriminable. Fig. 7.6 displays temperature profiles at various times from computer simulation using the heterostruture of a film grown directly on a substrate. When thermal conductivity is low, i.e. 0.5 W/m/K in Fig. 7.6(a) and Fig. 7.6(b), the characteristic time due to thermal conductivity estimated from 284 nm film is $\sim$ 50 ns. The time constants due to Kapitza conductance for cases (a) and (b) are 54 ns and 5.4 ns respectively. The thermal transport dynamics in cases (a) and (b) are mainly dominated by the slow thermal conductivity. For the cases (c) and (d), the characteristic times due to thermal conductivity are 1.2 and

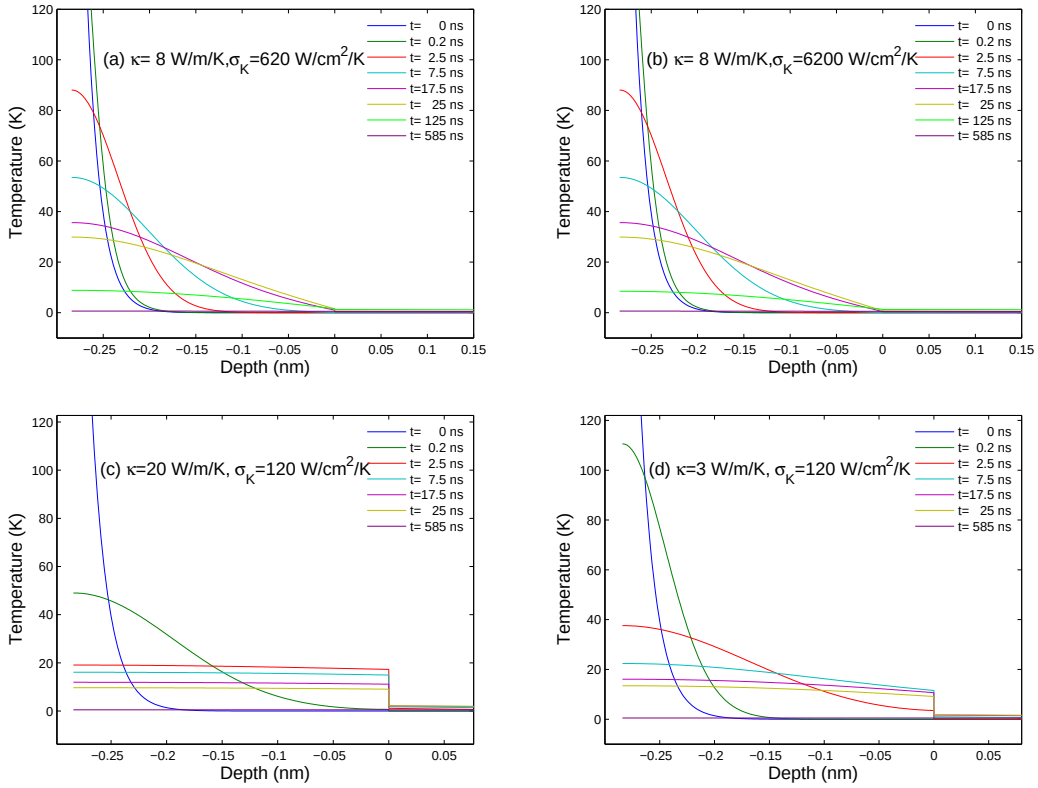

Figure 7.6: Simulations of temperature profiles as a function of depth for 284 nm film at various time delays in the limit of (a)(b) low thermal conductivity and (c)(d) low Kapitza conductance. Initial temperature is an exponential-decay profile with 15 nm penetration depth and maximum temperature rise 380 K. Negative and positive are film and substrate respectively with interface located at 0.

12 ns respectively. The time constant due to Kapitza conductance is 270 ns which is much slower than either value of characteristic time for thermal conductivity. For cases (c) and (d), the processes are dominated by Kapitza conductance. It is difficult to distinguish temperature profiles from (a) to (b) as well as from (c) to (d). However, cases (c) and (d) are distinguishable if time resolution is not limited by x-ray pulse duration. With better time resolution, the fast decay in case (c) is measurable and discrimination between (c) and (d) is possible.

The discrimination between cases (a) and (b) is not limited by time resolution. For thick film with slow thermal conductivity, a negligible temperature jump occurs

across an interface even with finite Kapitza conductance. This leads to the same situation as in the case for an interface with infinite Kapitza conductance. In such a case when measuring temperature decay at various depths, x rays are not sensitive to the Kapitza conductance and any value can fit the data. To elude the problem of negligible temperature jump across an interface when thermal conductivity is slow, a thin film is a better choice when both parameters are unknown. A thin film can limit diffusion time even with low thermal conductivity, and can increase the temperature jump across an interface with finite Kapitza conductance. Therefore, for thermal transport measurement, a thin film is a better design so long as small size effect does not occur.

7.6 Time- and depth-resolved x-ray studies of thermal transport for Bi on sapphire

This section covers asymmetric (grazing incident) and symmetric TRXD experiments. Asymmetric TRXD resolves dynamics at various depths in 65 and 284 nm films. For 65 nm film, shown in Fig. 7.7, the thermal decay signal is only due to Kapitza conductance for all grazing incident angles. For 284 nm, shown in Fig. 7.8, the decay is due to thermal conductivity at early times for small grazing incident angle ($< 1^{o}$), and is dominated by both thermal conductivity and Kapitza conductance at larger grazing angles. Symmetric TRXD measures the average dynamics of the entire film, detecting a decay only dominated by Kapitza conductance.

7.6.1 Grazing incident X-ray study for 65 nm film

The grazing-angle dependence of x-ray diffraction offers depth tunability of the probe in the film. Probing the top level of the film is sensitive to thermal conductivity at early times with a large thermal gradient. Probing the whole film is

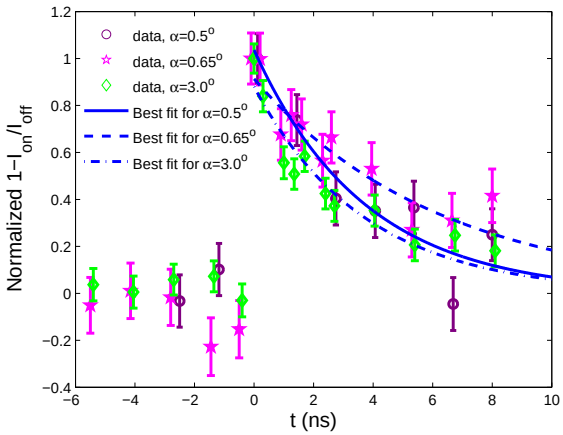

Figure 7.7: Thermal decay curves for 65 nm probing from various x-ray grazing incident angles. Using single exponential $ae^{(-t/\tau)}$, the best fit (a,τ) for various angles are (1.04±0.16, 3.70±1.03 ns), (0.91±0.08, 6.25±1.36 ns), and (0.88±0.07, 3.70±0.62 ns) respectively. The best fits are plotted as well.

sensitive to Kapitza conductance (assuming film thermal conductivity is not slow) which dominates heat transport across the interface and reduces the overall thermal energy stored in the film. The comparison among various probe depths also provides insight into heat distribution in the film. For thick film, the difference in decay signal at various probing depth is more pronounced.

Fig. 7.7 displays thermal decay curves following laser irradiation. Laser on and laser off are defined as the x-ray intensities measured after and before laser irradiation respectively at a selected (hkl). No significant difference in thermal decay curves exists among various probe angles. The characteristic time for thermal conductivity can be estimated using the literature value of total thermal conductivity (carriers and lattice) 5.2 W/m/K to get a lower bound, and using lattice thermal conductivity 1.9 W/m/K to get an upper bound [66], via eq.7.5. The characteristic time is thus estimated to lie between 0.24-0.65 ns, which is fast compared to the decay observed in 65 nm film. This indicates that the heat distribution is close to uniform on this

time scale and the observed decay is dominated by Kapitza conductance.

The best single exponential fit for the thermal decay curve in 65 nm film at various grazing angles is shown in Fig. 7.7. The Kapitza conductances extracted from eq.7.7 at $\alpha = 0.5^o$, 0.65^o, and 3.0^o x-ray grazing angles are 2066±574, 1223±268, and 2066±344 W/cm^2/K respectively.

To conclude the discussion on 65 nm film, it is found that temperature distribution is nearly homogeneous at various probe depth. For an uniform heat profile, probing at the surface or more deeply results in similar dynamics. However, it is found from the simulation that even with a large gradient near the surface in thin films such as 65 nm, the differences derived from simulations at various depths are within the margin of error. Thus, grazing incident TRXD for thin films requires much better statistics in order to tell whether the film has a large gradient near the surface. Nonetheless, from the estimate of characteristic time using the literature value for thermal conductivity, the thermal decay should be mainly dominated by the Kapitza conductance, which is about 1000-2000 W/m/K here.

7.6.2 Grazing incident x-ray study for 284 nm film

Fig. 7.8 displays time and depth resolved measurements for 284 nm film with (*hkl*) at half maximum on the peak for various x-ray incident angles as described in Sec. 7.6.1. The time delay was chosen from ∼10 ns before time zero to ∼ 70 ns after time zero. Because there is another gate set on the next x-ray bunch, the data is collected at whatever time delay is chosen, t, and $t + 153$ ns. 153 ns is the time separation between two x-ray bunches at 24-bunch modes at APS, as discussed in Chap. V.

When film gets thicker, the difference among various probing depths becomes

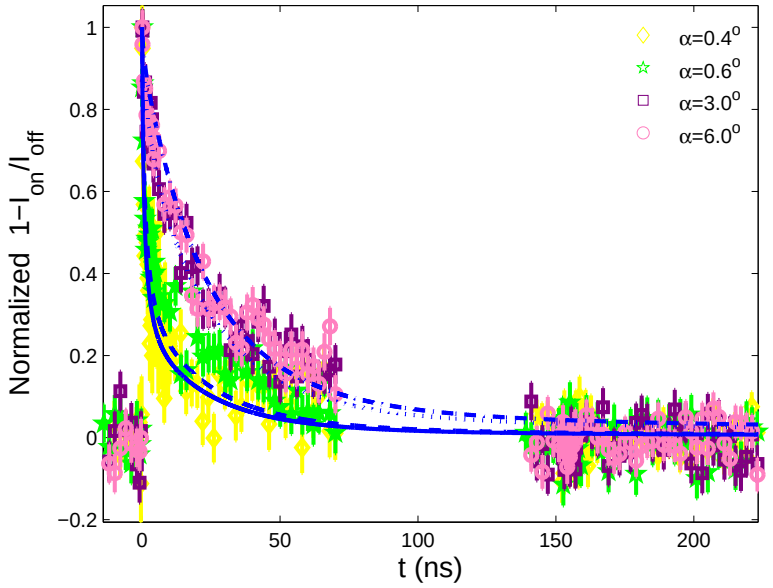

Figure 7.8: Various grazing incident x-ray measurements for 284 nm film. Different lines are simulation using best fit of Kapitza conductance 7760 W/cm^2/K with literature lattice thermal conductivity. The initial temperature profile is an exponential function with laser penetration depth 15 nm. The simulation result is convoluted with x-ray profile for various probe depthes.

noticeable if there is a large thermal gradient near the surface. For 284 nm film, the estimated characteristic time due to thermal conductivity is $\sim$ 4.5–12.5 ns (from lower and upper bounds using total and lattice thermal conductivity as discussed in the preceding section), which is slow compared to x-ray resolution. Thus with the known bulk thermal conductivity of Bi, different dynamics or decay signal is expected from various depth probes as shown in Fig. 7.8. As grazing angle increases, the decay becomes slower. Therefore, the inhomogeneity of temperature distribution is clearly seen here. The x-ray extinction depth corresponding to various incident angles at energy 7 keV are listed in Table 7.1.

While probing at the surface is sensitive to thermal conductivity in 284 nm film at early times, using larger grazing angles to probe more deeply becomes more sensitive

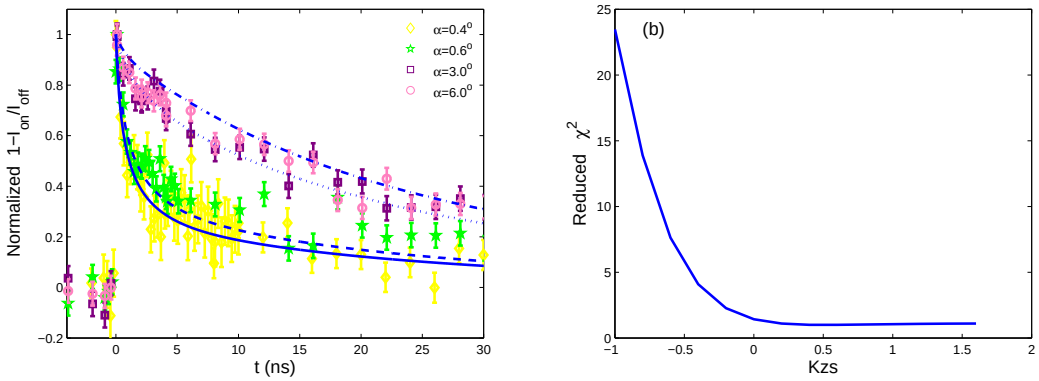

Figure 7.9: Various grazing incident x-ray measurements for 284 nm film at early times. (a) Data from Fig. 7.8 at early times. (b) Reduced chi square fit for data taken at α=6°. The relation between Kzs and Kapitza conductance is $1.95\times10^{2+Kzs}$ W/cm^2/K.

α (degree)	0.4	0.5	0.6	0.7	0.8	0.9	1.0	1.1	1.2	3	3.5	6	6.5
d_{ex} (nm)	3.5	12	21	29	36	41	48	54	60	160	186	320	347

Table 7.1: Various grazing angles and the corresponding extinction depth at 7 keV x-ray energy interacting with Bi.

to Kapitza conductance. When more material is probed, the decay process depends on both thermal conductivity and Kapitza conductance. Assuming film thermal conductivity is not low, x-ray measurement is sensitive to Kapitza conductance when the entire film is probed. In this case, the average temperature of the entire film stays the same while the film redistributes to a more uniform thermal profile.

Since film thermal conductivity of Bi is known and probing at the surface is not very sensitive to Kapitza conductance at early times, the conductance for 284 nm film is extracted by solving the one dimensional diffusion equation numerically,

$$\frac{\mathrm{d}T(t,x)}{\mathrm{d}t} = \frac{\kappa}{C}\frac{\mathrm{d}^2T(t)}{\mathrm{d}z^2}, \tag{7.8}$$

with boundary and initial conditions,

$$CL\frac{\mathrm{d}T(t)}{\mathrm{d}t} = -\sigma_K \frac{\mathrm{d}T}{\mathrm{d}z}\,|_{z=0}, \tag{7.9}$$

$$\frac{\mathrm{d}T}{\mathrm{d}z} = 0\,|_{z=-L}, \quad \text{and} \tag{7.10}$$

$$\Delta T(z, t=0) = T_0 e^{-z/\xi}, \tag{7.11}$$

where T_0 is the maximum temperature directly following laser irradiation with penetration depth ξ=15 nm for Bi. The simulation is weighted by convolution with the x-ray profile. With the known bulk thermal conductivity, the least square fit gives Kapitza conductance above 3000 W/cm^2/K for the data with α=6^o. There is not much difference among reduced χ^2 for conductance above 3000 W/cm^2/K for 284 nm film, as can be seen in Fig. 7.9(b). The best fit for Kapitza conductance is 7760 W/cm^2/K here, with negligible difference among χ^2 values for conductance above 3000 W/cm^2/K. This lack of sensitivity is due to the fact that Bi has relatively low thermal conductance and 284 nm is relatively thick; therefore, the temperature jump across the film is small, reducing the sensitivity to the Kapitza conductance as discussed in Sec. 7.5.

7.6.3 Kapitza conductance studied by symmetric TRXD

Using symmetric reflection, x rays probe the entire film and average its temperature profile. Fig. 7.10 shows Bragg angle shift as a function of time delay. The angle shift is derived from the difference in Bragg angle with and without the laser on, weighted by peak intensity at various time delays. The maximum average temperature in the film can be estimated via $\Delta\theta = -\alpha_l \mathrm{T}\tan\theta$. The estimates are about 15, 30, and 60 K for 284, 141 and 65 nm respectively, with the same fluence $\sim$0.2 mJ/cm^2.

Note that the plateau in the logarithm plot of Bragg angle shift in Fig. 7.10

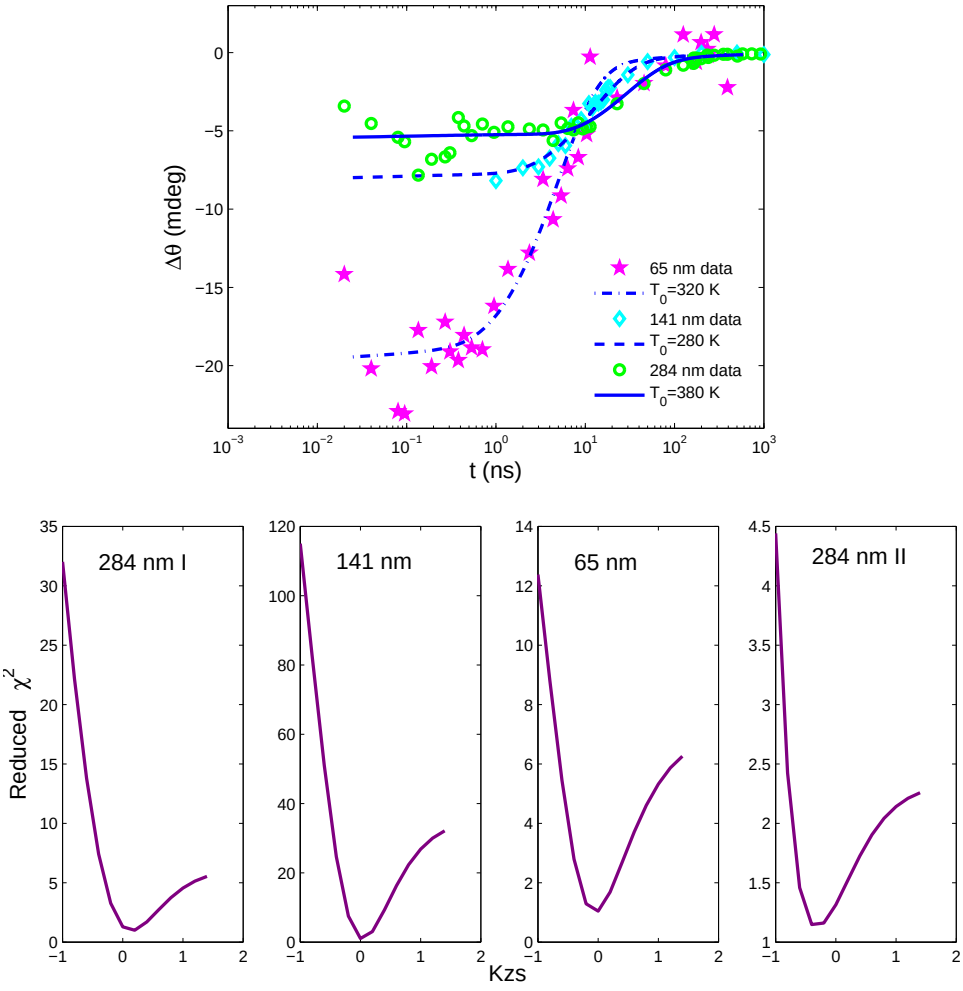

Figure 7.10: Time-resolve Bragg angle shift and reduced chi square fit. Upper: Time resolved Bragg angle shift of 006 diffraction for 3 different samples. The lines are best fit from numerical simulation. Lower: Reduced χ^2 fitting for various films. 284 nm I and II are measured from two beamtimes. The relation between Kzs and Kapitza conductance is $1.95\times10^{2+Kzs}$ W/cm^2/K.

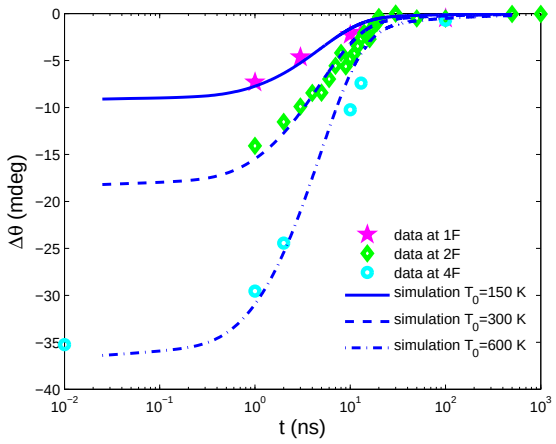

Figure 7.11: (color online) Time resolved Bragg angle shift from 006 diffraction at 3 different fluence for 65 nm film. The lines are numerical simulations using κ=2 W/m/K and σ_K=1950 W/cm^2/K and various T_0. T_0 is dereived from best fit of fluence 2F and is changed linearly with respect to the fluence.

is due to thermal conductivity which redistributes temperature to reduce the large gradient near the surface. From eq. 7.5, the characteristic times are about 12, 3, and 0.6 ns for 284, 141, and 65 nm respectively using the value of lattice thermal conductivity in Bi from the literature. The length of plateaus in the upper panel of Fig. 7.10 is about 10 and 1 ns for 284 and 65 nm films. The plateau is not clear in the data for 141 nm film due to lack of data points before 5 ns. However, the plateaus in the plots for 284 and 65 nm film correspond to the characteristic time using literature value for lattice thermal conductivity in Bi.

Following the plateau a decay in the Bragg angle shift is attributed to Kapitza conductance, and overall heat of the film is reduced. The reduced χ^2 fit for Kapitza conductance using lattice thermal conductivity from the literature is shown in the lower panel of Fig. 7.10. 284 nm I and II are from two different beamtimes. The best fit is 1950 W/cm^2/K for both 141 and 65 nm, and 3100 and 780 W/cm^2/K for 284 nm I and II respectively, giving an average of about 1920 W/cm^2/K.

The test of the fluence-dependent cooling using symmetric 006 reflection is demonstrated for 65 nm, shown in Fig. 7.11. The maximum change in Bragg angle is linear with increasing fluence below 3F, F≈0.2 mJ/cm^2. Above that value, the $\theta-2\theta$ curve shows a strongly asymmetric lower peak intensity and a broadened tail, indicating a huge diffuse scattering and some sample damage. The time it takes the film to cool through substrate depends on the film thickness via eq. 7.7 but not on the fluence. For samples with the same thickness, tt takes about the same time for most of the deposited energy to dissipate through the interface, indicating the fluence independence of Kapitza conductance. The time it takes for the same amount of energy to dissipate is roughly proportional to the film thickness, which is expected from eq. 7.7.

7.7 Discussion

The expression for Kapitza conductance for heat flow from medium A (B) to B (A) is discussed in Chap. III given as [37]

$$\sigma_K(T) = \frac{1}{V}\frac{\partial}{\partial T}\sum_{\mathbf{k}j}^{A(B)} \hbar\omega_{\mathbf{k}j} n(\omega_{\mathbf{k}j}, T)|v_{\mathbf{k}jz}|t_{\mathbf{k}j}. \tag{7.12}$$

The determination of transmission coefficient is usually based on two models, acoustic mismatch model (AMM) and diffusive mismatch model (DMM). If phonons can be treated as elastic waves, AMM is usually used. The transmission coefficient for normal incident phonons from material A to B in the AMM model is also discussed in Chap. III given as [3, 37]

$$T_{AB} = \frac{4\mathrm{Z}_A\mathrm{Z}_B}{(\mathrm{Z}_A + \mathrm{Z}_B)^2}. \tag{7.13}$$

If phonons are non-normal incident, Snell's law applies. For $v_A < v_B$, phonons can experience total internal reflection, reducing their transmission probability across an interface.

On the other hand, if phonons experience strong scattering near the interface, the diffusive mismatch model (DMM) might be more appropriate [37, 39]. In DMM phonons lose memory of where they are from and have the same transmission probability for high and low frequency phonons either from A to B or from B to A. In this model, the same frequency phonons from all angles have equal transmission probabilities which is mainly dependent on the density of state on each side of material. The transmission coefficient making use of the Debye assumption is also discussed in Chap. III where it is given as [39]

$$T_{AB} = \frac{\sum_j v_{B,j}^{-2}}{\sum_j v_{A,j}^{-2} + \sum_j v_{B,j}^{-2}}. \tag{7.14}$$

For sapphire, the transverse and longitudinal speeds of sound are 10.8×10^5 cm/s and 6.4×10^5 cm/s. For Bi, they are 1.97×10^5 cm/s and 1.03×10^5 cm/s. The densities of sapphire and Bi are 3.98 and 9.8 g/cm^3. AMM and DMM give respectively 86% and 97% predictions for transmission coefficient for Bi on sapphire when Debye's assumption is valid. Since the speed of sound for Bi is much smaller than for sapphire, in AMM the critical angle is small, $\sim$11.5^o, for phonons incident from Bi, assuming all scattering is elastic. Phonons with incident angles larger than the critical angle reflect toward the Bi surface. Therefore, taking incident angle into account in AMM we may have less than 86% phonon transmission for Bi/sapphire interface. Our optical reflectivity measurement shows that about 30$\pm$5% acoustic strain are reflected from the interface of Bi and sapphire. From energy conservation , the transmitted phonons will be about only 70$\pm$5% which is less than AMM normal incident prediction.

Both AMM and DMM treat phonon scattering as elastic. At very low temperature, the dominant phonons have very long wavelengths, close to the continuum case. Usually AMM predicts well for Kapitza conductance at very low temperature. At higher temperature, phonon wavelength becomes shorter, specular reflection from the interface is rare, and DMM should be a more appropriate mechanism to calculate the transmission coefficient. When samples are below their Debye temperature, both these two models are valid. Room temperature is below Debye temperature only for sapphire (T_D=1024 K) but not for Bi (T_D=120 K), meaning that neither AMM nor DMM is fully applicable. However, within the assumption of elastic scattering, the maximum transmission can be estimated by the radiation limit [37, 39]. For Debye temperature of B greater than that of A, phonons incident from either side cannot have frequency larger than $\omega_{cut,A}$ if only elastic scattering is allowed. The maximum Kapitza conductance occurs when all the phonons from B have transmission probability 1 across the interface. If Debye temperature of B is much higher than room temperature, the dominant phonons are long wavelength acoustic phonons. Since Debye temperature of sapphire is much higher than that of Bi , Kapitza conductance can be estimated to its upper limit as [37],

$$\sigma_K(T) = \frac{1}{V}\frac{\partial}{\partial T}\sum_{\mathbf{k}j,\omega\leq\omega_{cut,A}}^{B} \hbar\omega_{\mathbf{k}j} n(\omega_{\mathbf{k}j}, T)|v_{\mathbf{k}jz}|. \tag{7.15}$$

The advantage to using this radiation limit approximation is that we need not take phonon dispersion into account. Because Bi has a similar phonon spectrum to that of lead (Pb) at room temperature and a slightly higher Debye temperature, we can use the literature estimate for radiation limit of Pb (Debye temperature 102 K) grown on sapphire is around 1000 W/cm^2/K at room temperature [37]. It would be reasonable

to expect that the value of Kapitza conductance for Bi is larger because of higher cutoff frequency due to higher Debye temperature. The radiation limit in literature estimates Kapitza conductance across Pb/sapphire interface $\sim$ 1000 W/cm^2/K at room temperature, whereas the experimental results derive $\sim$ 5500 W/cm^2/K at room temperature in the same article [37]. The derived Kapitza conductance $\sim$ 1950 W/cm^2/K in our measurement for Bi/sapphire interface is within the range of their estimate and the extracted value from experiment at room temperature. For similar phonon spectrum in Pb and in Bi with slightly higher Debye temperature for Bi, our results is closer to the prediction using radiation limit.

Our optical reflectivity measurements for Bi not only show $\sim$30$\pm$5% acoustic reflection from the interface, but also demonstrate that the acoustic reflection has no clear dependence on the film thicknesses investigated in this dissertation. If energy is conserved, the sum of phonon transmission and reflection should be equal to one and thus the transmission should also be independent of the thickness. In principle, Kapitza conductance should have no explicit dependence on the film thickness used here, as they are thick enough to be approximately assumed bulk-like. The different values of Kapitza conductance obtained for 284 nm by symmetric diffraction could be due to the systematic error from the two beamtimes since the average signal for Bragg angle shift is smallest in 284 nm compared to 65 and 141 nm. This is due to the relatively small thermal conductivity of thick (284 nm) film leading to negligible temperature jump across the interface and increasing the fluctuation over different measurements.

7.8 Summary

The use of time- and depth-resolved x-ray diffraction to study the thermal transport across the interface of Bi on sapphire has allow direct measurement of atomic dynamics through lattice expansion. The depth-resolved measurements demonstrate that the cooling near the surface for 284 nm film is dominated by the thermal conductivity, while sensitivity to Kapitza conductance increases when grazing angle increases. Although there is a large gradient near the surface, thermal conductivity of the film redistributes heat rapidly over a thickness of 65 nm, taking much less than 1 ns. Therefore, the depth resolved measurement for 65 nm film is dominated by Kapitza conductance. From the existence of a thermal gradient near the surface of Bi grown on sapphire averaged out due to a x-ray long penetration depth, Kapitza conductance can be extracted from the symmetric TRXD. The extracted Kapitza conductance is 1950 W/cm^2/K for 65 as well as 141 nm film. This value is also the average from the two measurements of 284 nm film. Thus $\sim 1950 pm 1000$ W/cm^2/K is averaged over three samples and various beamtimes. Comparing the material (Pb) with similar phonon spectrum and with slightly lower Debye temperature to Bi, both grown on sapphire, our derived value for Bi/sapphire interface is between the estimate using radiation limit and the value extracted from experiments for Pb/sapphire interface. Our deduced value is closer to the estimate for Pb/sapphire interface using radiation limit in the literature, assuming phonon spectra in Bi and in Pb are similar.

CHAPTER VIII

Optical Pump-Probe Studies of Bi Thin Film at Low Excitation

Ultrafast laser excitation of solids can dramatically alter the interatomic forces by depositing substantial amounts of energy into free-carriers on a time scale that is short compared to energy relaxation. In the group V semimetals, the excitation of even modest plasma densities leads to large-amplitude atomic motion corresponding to a coherent zone-center fully symmetric (A_{1g}) optical phonon. The generation of the coherent phonon can be understood, at least in the low density limit, as a Raman process [43], or phenomenologically as an electronically driven reduction in the Peierls distortion in these materials which suddenly alters the equilibrium position of the ions within the unit cell (displacive excitation) [67].

Recently there has been considerable interest in the dynamics of the A_{1g} mode in the limit of dense photoexcitation, particularly for bismuth [6, 8, 9, 15, 58, 68, 69, 70, 71]. It was first pointed out in Hase et al. [15] that the frequency of the mode is dramatically chirped. Murray et al. [8] demonstrated both experimentally using double-pulse excitation and theoretically using constrained density functional theory (DFT) and frozen phonon calculations, that the chirp is dominated by electronic softening and the evolution of the dense electron-hole plasma. Later, the

theoretical studies were extended to include softening of the entire phonon spectrum [45]. The general results for the A_{1g} mode were confirmed by Fritz et al. [9] using femtosecond x-ray diffraction to measure the quasi-equilibrium position and curvature of the excited state potential. However, the results of measurement of ultrafast oscillations in the Debye Waller factor by Johnson et al. [72] suggested that the coupling of the plasma with low-frequency acoustic phonon modes may not be well described in current theoretical models. The calculations in [8, 45] assume that a single electron-hole pair is created by each absorbed photon and that, whereas intraband scattering rapidly establishes a Fermi-Dirac distribution of carriers in each band, the electron-hole recombination time is substantially longer than the period of the relevant phonon and, as a result, the chemical potential for the conduction bands differs from that of the valence bands (two chemical potential model). In contrast, Zijlstra et al. [12] performed frozen phonon calculations on the zone-center mode, also assuming rapid scattering and equilibration throughout all conduction and valence bands, but using a single chemical potential, in which the carrier density is determined by temperature of the electron-hole plasma. Johnson et al. [58] performed depth-resolved femtosecond x-ray diffraction to measure the phonon dynamics and concluded that the two-chemical potential model may be appropriate only on a time-scale less than a single phonon period, transitioning to a single-chemical potential model for a longer time scale. Recently Scianini et al. [73] measured a 2–3 ps lattice thermalization time of the photoexcited carriers in the limit of dense excitation using ultrafast electron diffraction, indicating a rapid energy transfer from carriers to the lattice. Still the dynamics of the photoexcited carriers is not well understood.

In this chapter, I show experimental results for the four different pump-probe geometries introduced in Chap.VI at low excitation region $\sim 10^{18}$ cm^{-3}. Optical

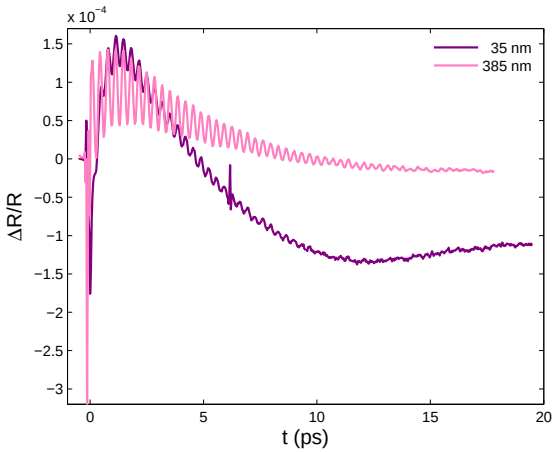

Figure 8.1: Comparison between 65 nm and 385 nm films for A_{1g} phonons in surface-pump-surface-probe data.

reflectivity is modulated by carriers, optical as well as acoustic phonons, and lattice heating. Carrier diffusivity, recombination, and lattice thermalization time will be deduced by comparison with model simulation.

8.1 Sample

Various thickness Bi films were grown on 1×1 cm^2 sapphire substrates (c-axis cut ~ 0.5 cm thick by molecular beam epitaxy (MBE). The films are single crystals with the trigonal axis perpendicular to the film as determined by x-ray diffraction. The determination of film thickness is described in Chap.VII, by x-ray and optical reflectivity.

8.2 Surface Pump Surface Probe

Fig. 8.1 displays the A_{1g} phonon with frequency ~ 2.88 THz for 35 nm and 385nm films, measured by conventional surface-pump and surface-probe geometry. The A_{1g} phonon generation mechanism is discussed in Chap. IV as displacive excitation. The oscillation frequency strongly depends on the carrier density. The softening of the

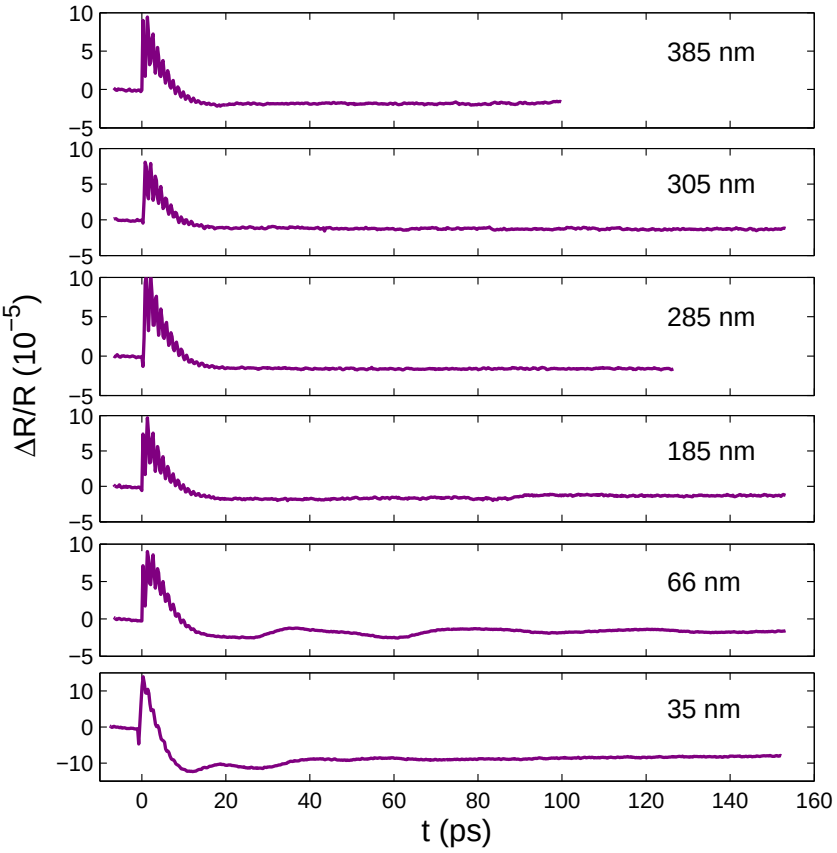

Figure 8.2: Surface-pump-surface-probe data for various film thicknesses.

A_{1g} oscillations may be induced by the large amount of photoexcited carriers that changes the interatomic potential [45]. The density excited here is $\sim 10^{18}$ cm^{-3}, and neither softening nor clear evidence of frequency chirp is observed here. Compared to the carrier density at room temperature without any excitation, i.e. $\sim 5\times10^{17}$ cm^{-3}, 10^{18} cm^{-3} corresponds to low excitation density. Less than 10^{-4}% of the valence electrons are excited.

Fig. 8.2 shows reflectivity data for conventional surface-pump and surface-probe geometry, ranging from 35–385 nm. Maximum fluence absorbed was estimated to be about 0.8 μJ/cm^2, and the corresponding excitation carrier density is $\sim 2\times10^{18}$ cm^{-3}. Upon the arrival of the pump pulse, photoexcited carriers are generated on a time-

scale short compared to the highest frequency phonon oscillation $f(A_{1g}) \approx 2.92$THz. The partial derivatives are in general not known at nonequilibrium state; however, we can deduce their signs as to be: $\partial R/\partial Q > 0$ (x driven towards the symmetric non-Peierls distorted structure), $\partial R/\partial n > 0, \partial R/\partial \eta < 0$ for tensile and > 0 for compressive strain and $\partial R/\partial T < 0$. Assuming small perturbations, the second order and higher terms are negligible .

In surface-pump surface-probe data as Fig. 8.2, $\Delta R(t)/R$ first increases rapidly due to the increase in carrier density and then slowly decreases as the carriers relax via multiple processes. This increase and then decrease of reflectivity signal is referred to as carrier peak in the following discussion. Because of strong absorption, carriers are generated near the surface (15 nm laser penetration depth), and the probe beam only detects the change near this region. Clearly from Fig. 8.2 any differences in the data for different film thicknesses are subtle. The oscillations are due to the A_{1g} optical phonons aliased by the sampling rate. Approximately 10 ps after the arrival of the pump pulse, the relative change in reflectivity ($\Delta R/R$) becomes negative due to lattice heating, slowly returning to its unperturbed signal due to thermal diffusion into the bulk. The overall reduction of the reflectivity signal during the first few picoseconds is due to a competition of effects: carrier relaxation through ambipolar diffusion into the bulk; recombination; lattice heating; and the propagation of an acoustic pulse generated through a combination of rapid thermal expansion and acoustic deformation potential interaction, complicating the analysis. Although one can also use samples thin compared to optical penetration depth to avoid diffusion effects, strain, lattice heating and optical interference will still affect the measurements. As shown in Fig. 8.2, in 35 nm film acoustic strain mixes with its echoes, making the problem more complex.

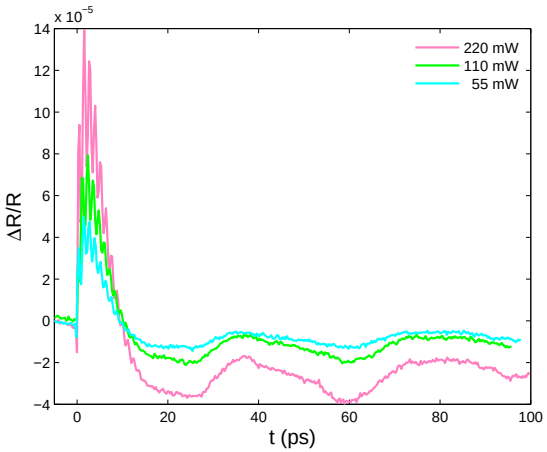

Figure 8.3: Power dependence data for 66 nm film measured from surface-pump-surface-probe geometry.

Except for in 35 nm thin film, the carrier peak as shown in Fig. 8.2 looks almost identical for films ranging from 35–385 nm. In the data for 66 nm film, the separation of acoustic strain and its echoes is not as clear as in other thicker films, partially because of overlap in the reflectivity signal. Apart from this difference, all features including the magnitude of the relative change in reflectivity, positive and negative, are similar to those in thicker films.

The 35 nm film has a major difference in the falling edge of its carrier peak: it takes less time to reach the negative signal, which is attributed to lattice heating. In addition, both maximum positive and minimum negative signals have magnitudes of relative change in reflectivity larger than those of other samples. This is due to more absorption (less reflection) for 35 nm when comparing time-independent reflectivity measurements to those of thicker samples. From the figure it is clear that the width of the carrier peak including rising and falling edges is narrower in 35 nm.

Except in 35 and 66 nm films, no clear evidence shows any difference among various film thickness ranging from 35–385 nm. The power dependence data is shown

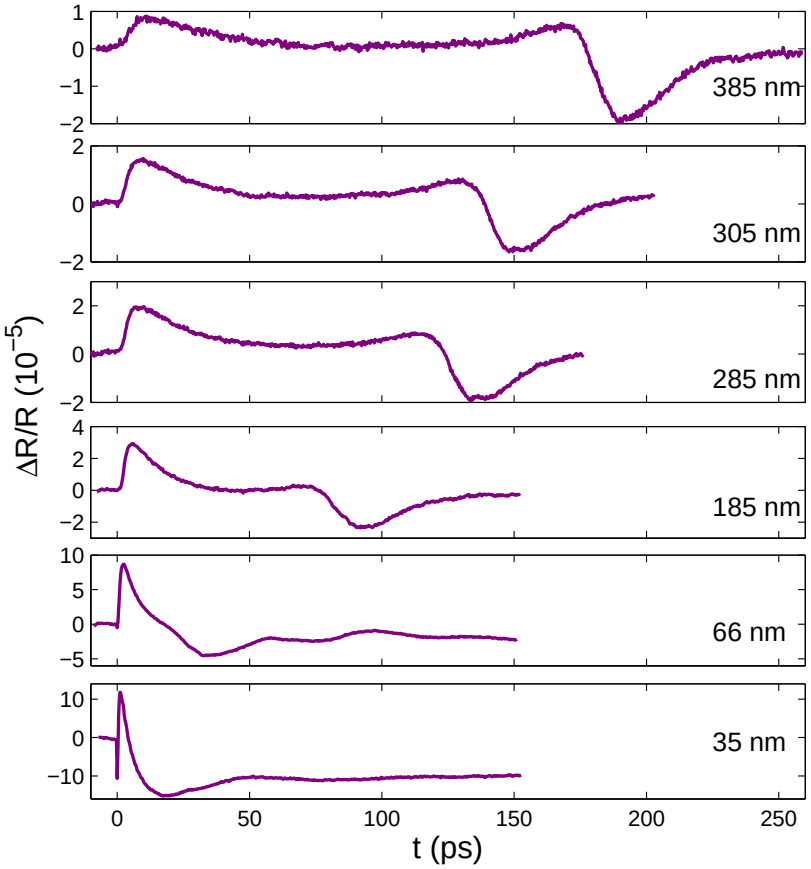

Figure 8.4: Surface-pump-interface-probe data for various film thicknesses.

in Fig. 8.3. The carrier peaks are scaled linearly to the excitation density. The signals of acoustic and lattice heating are slightly off at the highest excitation density. However, the overall behavior of the signals in these excitation regions is close to linear.

8.3 Surface Pump Interface Probe

Fig. 8.4 shows the reflectivity signal for Bi films using surface-pump and interface-probe geometry. Clear differences can be distinguished from the surface-pump and interface-probe data. There is no coherent A_{1g} phonon signal present on the surface-pump and interface-probe data, consistent with a localized excitation of the zero

group velocity mode in the laser-excited volume of the optically thick films [74]. In addition, there is no clear effect on our samples thicker than 65 nm from heating due to relatively low thermal diffusivity. Thus, to the extent that we can ignore heating due to recombination at the back surface, both the first and last two factors on the right hand side of equation 6.4 are absent in the backside signal of samples thicker than 185 nm. The bipolar shape of the plot at late times for films ranging from 185–385 nm is attributed to the acoustic strain pulse. The speed of sound derived from the time the acoustic pulse takes to propagate across a known thickness sample (185 nm, measured by grazing incident x-ray reflectivity, see Chap.V), 2150 m/s, is close to the literature value of 1972 m/s [75]. We use this value to calibrate other film thicknesses, which were too thick to get reliable measurements by interference fringes in grazing incidence x-ray reflectivity. Note that the time needed for the early signal to peak decreases with decreasing film thickness. This time is shorter than the time it takes sound to propagate across the sample, and is attributed to the carriers diffusing across the sample. The whole peak at early times after time zero is thus interpreted as a carrier peak. It is important to note that the acoustic pulse is well separated from the carrier peak due to the relatively low speed of sound yet high carrier diffusivity, allowing the isolation of the effects from recombination and diffusion.

8.3.1 Comparison between surface and interface probe

It is worth noting that lattice heating is still observed in 66 and 35 nm films when probed from the interface. Additionally, partial overlap between acoustic strain and its echoes is also observed. Both these effects are partially due to thinness of the films; which does not separate well between the profiles of the pump and probe. The

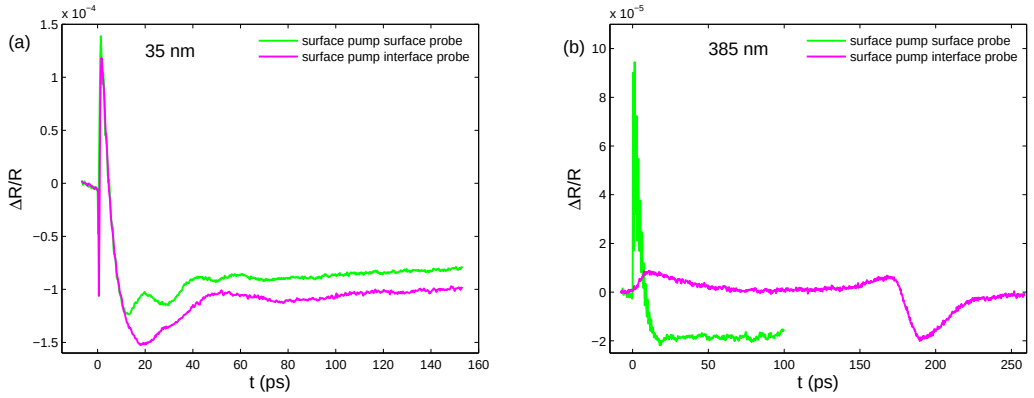

Figure 8.5: Comparison between surface-pump-surface-probe and surface-pump-interface-probe data for (a) 35 nm and (b) 385 nm films.

superposition of the reflected and incoming acoustic strain happens at the interface, and the acoustic strain has a finite width in the film. When the film is not much thicker than the acoustic width, its echoes are not well separated in time as they would be in thicker films.

The differences between surface probe and interface probe are shown in Fig. 8.5. The carrier peaks in these two geometries are similar for 35 nm film, while for 385 nm film they are very different. For 35 nm film, carrier diffusion is negligible and carrier recombination dominates carrier dynamic. For 385 nm film, both diffusion and recombination are important, which leads to a smaller and broader carrier peak for interface probe. In addition, the pump and probe are well separated in 385 nm film but not in 35 nm film. Therefore, except for the acoustic echoes, the reflectivities measured from either side are similar for 35 nm film.

8.3.2 Analytical approach for carrier diffusion and recombination

The carrier peak shown in Fig. 8.4 contains information on both ambipolar diffusion and recombination. The experiments performed for a range of low excitations (see Fig. 8.6) show no significant change in the time of peak signal (t_p) and the sub-

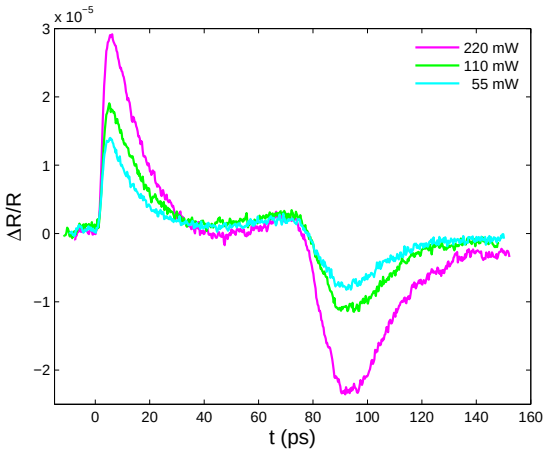

Figure 8.6: Surface-pump-interface-probe data for 185 nm film at various excitation densities.

sequent decay for different thicknesses, indicating that the recombination rate γ and ambipolar diffusivity D are approximately independent of density at low excitation region. Since film thickness is a few hundred nanometers and therefore much smaller than the pump diameter $\sim$150 μm, it can be assumed that carriers are subject to one-dimensional diffusion along the trigonal axis, z (surface normal),

$$\frac{\mathrm{d}n}{\mathrm{d}t} = D\frac{\mathrm{d}^2 n}{\mathrm{d}z^2} - \gamma n. \tag{8.1}$$

Before proceeding to fit the data with a detailed model of the carrier dynamics, it is instructive to consider the limiting case of an infinitely thick sample with a delta-function excitation. A rough estimate for both D and τ can be derived from measurements of t_p. In this limiting case the solution to eq. 8.1 is well known,

$$n(z,t) = \frac{n_0}{\sqrt{\pi D t}} \mathrm{e}^{-\frac{z^2}{4Dt}} \mathrm{e}^{-t/\tau}. \tag{8.2}$$

Thus,

$$t_p = \frac{\tau}{4}\left(\sqrt{1+\frac{4z^2}{D\tau}} - 1\right). \tag{8.3}$$

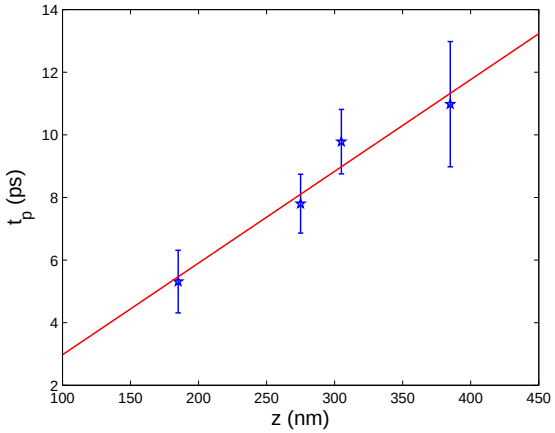

Figure 8.7: Peak times versus film thicknesses.

Note that deep into the bulk t_p is linearly proportional to z,

$$\frac{\mathrm{d}t_p}{\mathrm{d}z} \approx \frac{1}{2}\sqrt{\frac{\tau}{D}},\ z \gg \sqrt{D\tau/4}. \tag{8.4}$$

From this analysis we find that samples of 185–385 nm reasonably approximate this condition on the back face. At time t_p, the carrier density n is approximately uniform throughout the film, and thus τ can be estimated from the exponential decay of reflectivity signal while D is estimated from the slope, $\sqrt{\tau/4D}$, of eq.8.4 (see Fig. 8.7). In this manner, τ is $\approx 25 \pm 5$ ps and D is $\approx 72.8 \pm 51.8$ cm^2/s, averaged over the films. Note that $\mathrm{d}L/\mathrm{d}t = 2\sqrt{D/\tau} \approx 3.4 \times 10^6$ cm/s is more than 10 times the speed of sound, which leads to the separation of carrier peak and acoustic peak when pump and probe are at different sides.

8.3.3 Numerical approach–carrier diffusion and recombination

To better model the data for surface pump and interface probe, I solve the finite crystal case numerically. Assume the carriers are confined at both the air and sapphire interfaces, $\mathrm{d}n/\mathrm{d}z|_{z=0,\mathrm{L}} = 0$, which is valid so long as surface recombination is slow compared to bulk. The photoexcited carriers are assumed to decay exponen-

Bi film	De (cm^2/s)	$\tau = 1/\gamma$ (ps)	Bi film	De (cm^2/s)	$\tau = 1/\gamma$ (ps)
185 nm	18±5	12±2	275 nm	24±6	26±4
305 nm	28±5	24±3	385 nm	40±14	26±6

Table 8.1: Diffusivity and recombination for various film thicknesses at low excitation.

tially as a function of depth,

$$n(z, t = 0) = \frac{Q}{\hbar\omega\zeta} \mathrm{e}^{-z/\zeta}, \tag{8.5}$$

where Q, $\hbar\omega$, and ζ are respectively fluence absorbed in films, photon energy (1.5 eV), and laser penetration depth (15 nm). Simulated signal is convolved with the probe profile (exp(-z/ζ)). The initial carrier density n(z=0,t=0) is estimated to be about 2×10^{18} at the surface. The simulated amplitude is normalized to the data signal. The best fits are summarized in Table 8.1.

The result shows that the diffusion of photoexcited carriers for Bi at low density is relatively fast. Comparing the surface-pump and interface-probe data with the surface-pump surface-probe data (as in Fig. 8.5 (b)), it is clear for the 185 nm and thicker films that lattice heating occurs only near the surface region in the latter geometry. For the thinnest films, a lattice heating signal is still observed by the interface probe. This is due to a film thickness comparable to the laser penetration depth, making pump and probe overlap partially. While a large negative relative-change in reflectivity occurs near the surface, interface probe data shows no clear evidence of lattice heating for thick films with substantial numbers of carriers diffusing to the interface. Comparison with surface-probe data indicates that in the interface-probe case, the carriers arrive at the interface and become cold, as a carrier peak without lattice heating is observed.

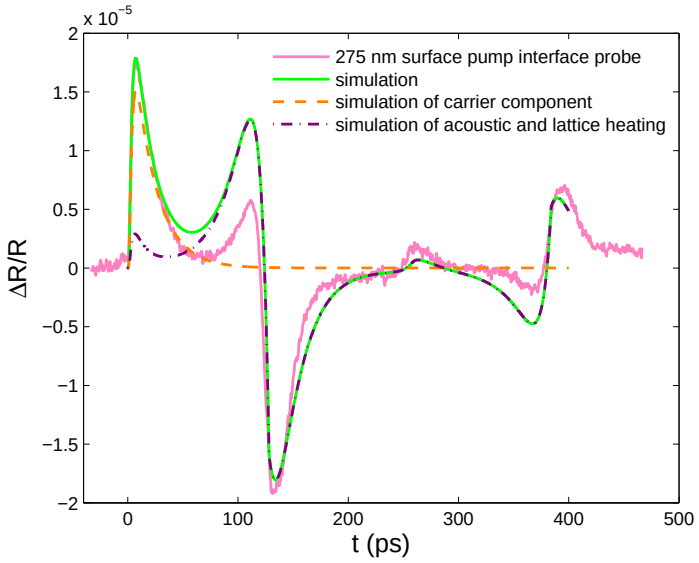

Figure 8.8: Surface-pump-interface-probe data and simulations for 275 nm film. Figure shows both data and simulations using two-decay model. Various components from simulations are also displayed separately. The simulations use parameters of diffusion constant D_e=28 cm^2/s, recombination time $\tau_1=1/\gamma_1$=20 ps, and lattice thermalization time $\tau_2=1/\gamma_2$=0.8 ps.

8.3.4 Numerical approach– acoustic strain and two decay model

Generation of acoustic strain contains information about carrier dynamics. Propagation of acoustic strain can elucidate the interface properties. Fig. 8.8 shows several echoes bouncing back and forth in 285 nm film. The first bipolar feature around 100–150 ps is the incoming strain propagating from the surface corresponding to $t=L/v$. The second one at around 400 ps is the echo reflected from the surface propagating back toward the interface. The phase of the reflected strain depends on the acoustic impedance. The acoustic impedance Z of air, Bi and substrate are in the order $Z_{air}<Z_{Bi}<Z_{sapphire}$. Thus, acoustic strain flips phase at the air/Bi interface but remains the same phase at the Bi/sapphire interface. A small peak around 280 ps is attributed to the strain generated from deformation potential coupling. When the pump is on the surface, this time of propagation is not correlated to any thermal

strain generated from lattice heating near the Bi surface. The only possibility corresponding to the observed strain at $t = 2L/v$ is the non-thermal strain generated by fast carrier diffusion toward the interface. Thus the small peak is attributed to the strain generated at the interface by carrier diffusion via deformation potential coupling.

When modeling the strain generation, I found that it cannot be explained using the instantaneous heating model. For instantaneous heating, the width of strain is equal to laser penetration depth. However, from the data it is wider than laser penetration depth, which indicates that fast carrier diffusion occurs before energy transfers to the lattice. On the other hand, taking carrier diffusion and recombination from Table 8.1 and assuming lattice heating is from carrier recombination, I obtain the modeled strain too wide compared to the data. Therefore, lattice heating is not mainly from carrier recombination, and lattice thermalization time should be faster than carrier recombination.

As a result, the total strain is the superposition of the thermal strain generated from lattice heating and the non-thermal strain generated from the deformation potential. The thermal strain can be modeled by the two-decay model: one decay is the carrier cooling and the other is the carrier recombination. Assuming one photon absorption per electron-hole pair, the process includes: one dimensional carrier diffusion, energy transfer to the lattice by carrier cooling which reduces the average energy per carrier but maintains carrier density, and energy transferred by electron-hole recombination which changes the number of carriers but maintains the average energy per carrier. If ϵ is the average energy per carrier and n is the carrier number density, the decay in total energy u is,

$$\frac{\mathrm{d}u}{\mathrm{d}t} = \epsilon\frac{\mathrm{d}n}{\mathrm{d}t} + n\frac{\mathrm{d}\epsilon}{\mathrm{d}t}, \tag{8.6}$$

where the first term on the right hand side is due to carrier recombination. The average energy decay is assumed to be a single exponential with decay rate ϵ_1,

$$\frac{\mathrm{d}\epsilon}{\mathrm{d}t} = -\gamma_2\epsilon(t) \tag{8.7}$$

with a simple solution

$$\epsilon(t) = \hbar\omega e^{-\gamma_2 t}. \tag{8.8}$$

The carrier density satisfies

$$\frac{\mathrm{d}n(z,t)}{\mathrm{d}t} = D\frac{\mathrm{d}^2u}{\mathrm{d}z^2} - \gamma_1 n(z,t). \tag{8.9}$$

Energy transfer from carrier to lattice satisfies

$$C_l\frac{\mathrm{d}T(z,t)}{\mathrm{d}t} = -\frac{\mathrm{d}u}{\mathrm{d}t} = \epsilon(\gamma_1+\gamma_2)n(z,t) \tag{8.10}$$

$$= \hbar\omega e^{-\gamma_2 t}[(\gamma_1+\gamma_2)n(z,t)]. \tag{8.11}$$

Using the diffusion and recombination (τ_2=$1/\gamma_2$) from Table 8.1, the simulated strain has thermalization time $\tau_1 = 1/\gamma_1 \sim 0.8$ ps. The simulated signal is convolved with the exponential profile of the interface probe. There are several contributions to the simulated signal: carrier, thermal strain, non-thermal strain, and lattice heating. The coefficient of $(\mathrm{d}R/\mathrm{d}T)/R$ is -8×10^{-5} $1/\mathrm{C}^0$, taken from Ref. [76]. Using the relation

$$\frac{\mathrm{d}R}{\mathrm{d}T} = \frac{\mathrm{d}R}{\mathrm{d}\eta}\frac{\mathrm{d}\eta}{\mathrm{d}T} = \frac{\mathrm{d}R}{\mathrm{d}\eta}\alpha, \tag{8.12}$$

where α is the linear expansion coefficient, the coefficient of $(\mathrm{d}R/\mathrm{d}\eta)/R = 5.97$ is thus deduced. In addition, $\mathrm{d}\eta/\mathrm{d}n$ is 0.72 along c axis [53]. Therefore, the differential coefficient of strain is known, but those of the carriers are still not known. The simulated signal of carrier peak, i.e. $(\mathrm{d}R/\mathrm{d}n)/R$, is scaled to peak intensity from the thickest film, i.e. 385 nm, and applied to simulations of other film thickness. The carrier peak is not entirely contributed by the increase in carrier density upon laser excitation. Partial ($\sim$10%) contribution is from strain generated from carrier-induced non-thermal lattice expansion. The thicker the film, the less contribution from non-thermal strain. Taking parameters from Table 8.1 as well as 0.8 ps thermalization time, the comparison between data and simulation for the 275 nm film is shown in Fig. 8.8. The various lines are different contributions from carrier, strain (including thermal as well as non-thermal), and lattice heating.

Chap. IV contains an overview of several mechanisms of strain generation. I summarize some features based on the comparison between the data and the numerical simulation in this section. Adding the coupling between photoexcited carriers and strain, the simulation shows a small feature around $t = 2L/v$ corresponding to the non-thermal strain. Sudden increase in carrier density produces stress on a lattice, which launches two compression strains propagating oppositely. The asymmetric nature of the acoustic strain is clearly seen from the simulation (Fig. 8.8). The simulation results in a a nearly unipolar non-thermal strain taking parameters from Table 8.1. In the generation model of non-thermal strain, the spatial distribution of carriers can affect the shape of the propagating strain. The dominating factors that alter the spatial distribution of carriers are the diffusion and recombination. Carrier diffusion has a similar effect to change the shape of strain as the thermal diffusion discussed in Chap. IV. However, this effect is much more pronounced when caused

by fast carrier diffusion than slow thermal diffusion. In addition, recombination reduces the overall carrier density, and the corresponding stress produces the expansion strain. The overall effect makes the non-thermal strain more unipolar, as shown in the individual components in Fig. 8.8. Therefore, the superposition of thermal and non-thermal strain produces the asymmetric overall acoustic strain.

The decay and recombination in the thinnest films (35, 66 nm) are faster than in thick films; however, these two parameters have no explicit dependence on the carrier density at low excitations. The discrepancies of faster diffusion and recombination observed between thin films and thick films are not yet clear.

8.4 Interface pump

In the previous section, I have shown the comparison between surface- and interface-probe data when both are pumped from the surface. One might be interested in the results of experiments that are pumped from the interface. Since sapphire is transparent to the laser, no excitation will occur in the sapphire. The boundaries of air/Bi and sapphire/Bi differ, since sapphire/Bi is not a free surface. The photoexcited carriers in Bi diffuse only toward the surface since there is no allowed electronic state for them in sapphire. The strain, on the other hand, can propagate in both directions. Because the impedance of sapphire is slightly higher than that of Bi, the strain propagating toward the interface partially transmits and partially reflects back toward the surface. Since acoustic echoes of the surface-pump and interface-probe signal have approximately 35% reflection from the interface, the acoustic signal from the surface probe is expected to be smaller than the case when the position of pump and probe are reversed.

In addition, the shape of the acoustic pulse observed from optical reflectivity is

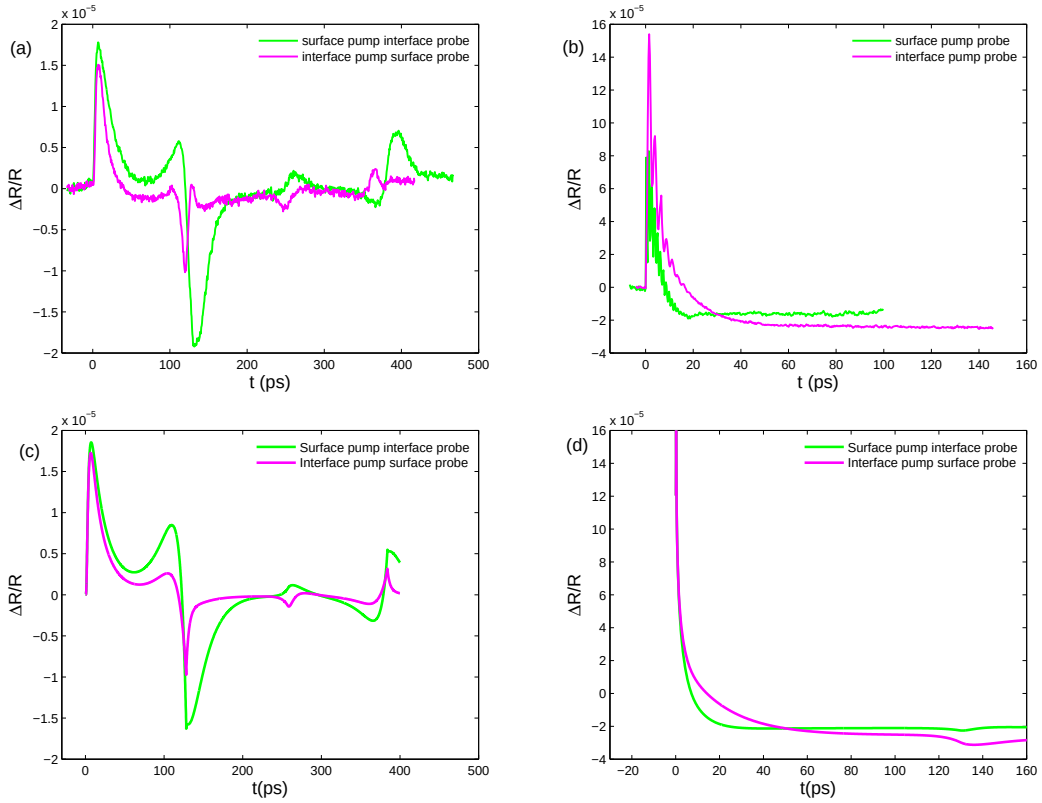

Figure 8.9: Comparison between surface-pump (magenta line) and interface-pump (green line) geometries. (a) Opposite side pump probe for 285 nm film. (b) Same side pump probe for 385 nm film. (c) Simulations of opposite side pump probe for 285 nm film. (d) Simulations of same side pump probe for 385 nm film. The simulation uses parameters of diffusion constant D_e=28 cm^2/s, recombination time $\tau_1=1/\gamma_1$=20 ps, and lattice thermalization time $\tau_2=1/\gamma_2$=0.8 ps.

different due to the different boundary conditions between air/Bi and sapphire/Bi interfaces. Acoustic strain does not flip its phase at the interface of sapphire/Bi. It is thus expected that the signal of thermal strain from counter-propagating pump-probe data (respectively, conventional same side pump-probe data) will be different when the position of surface and interface are reversed. Fig. 8.9 displays the comparison between surface-pump and interface-pump signals. Fig. 8.9(a) is the signal probed on the opposite site of the pump. Thermal strain signal from surface pump is larger than that from interface pump due to partial transmission of the acoustic strain from

the interface upon excitation.

Pump and probe from the same side, either surface pump or interface pump, has similar signal except for the decay rate starting from the peak signal as in Fig. 8.9(b). Surface-pump-surface-probe data has faster decay while interface-pump-interface-probe data has slower decay. The decay has been explained in Sec. 8.2 due to a combination of effects including carrier recombination, carrier diffusion, acoustic strain propagating across the absorption region, and lattice heating which induces negative reflectivity change. The main difference between surface and interface generation is due to the different boundary conditions for generation and propagation of acoustic strain as discussed above. The simulation also qualitatively displays similar behavior for both sides.

8.5 Conclusion at low excitation

In this chapter, I have compared various film thicknesses at extremely low excitation, $\sim 10^{17}$–$\sim 10^{18}$ cm^{-3}, using four pump-probe geometries from the combination of pump or probe at surface or interface of various Bi films. For film thicknesses above 185 nm, pump and probe profile are well separated for counter-propagating geometries, and the probe detects the dynamic when carriers are more or less homogeneous (when $t > t_p$). The decay is attributed to electron-hole recombination, which is about 12–26 ps for films ranging from 185–385 nm. The extracted diffusivity for these film thicknesses is ~ 25 cm^2/s with slightly deviation from film to film. Several acoustic echoes are observed and can be qualitatively simulated by the proper modification of Thomsen's model incorporating a two-decay model that I develop in Sec. 8.3.4. Non-thermal strain due to carrier deformation potential is evident and is simulated within the framework of the modified model. From strain analysis,

lattice thermalization time is estimated about 0.8 ps for various film thicknesses. The results of relative fast carrier diffusion, slow carrier recombination, and fast lattice thermalization are in agreement with two-chemical potential model assumption, where photoexcited carriers can maintain their density by varying chemical potential and temperature.

At low carrier density, each contribution to the reflectivity signal is more or less linear as a function of fluence. Comparison of the data for pump on either surface or interface shows clear evidence of different boundary conditions for strain generation and propagation. One problem not solved here is the tendency for faster decay of the signal in thin films, i.e. 35 and 66 nm. The mixture of lattice heating, acoustic echoes, and carrier decay signals, is another remaining problem for thin films. The observed decay in thin films is faster than in thick films. From the theoretical point of view, one may expect this is due to the confined carrier density. However, varying carrier density in experiments at low excitation by changing fluence has no effect on the fast decay, i.e. decay rate is independent of the carrier density. I discuss this problem further in the next chapter on the high excitation region.

CHAPTER IX

Optical Pump-Probe Studies of Bi Films at High Excitation

The low excitation region is a key starting point for the understanding of carrier dynamics of Bi upon laser excitation. It is a bridge between the fundamental phenomenon of carriers near the Fermi surface and the extreme case of carriers far above the Fermi surface. Investigation of high densities of excited carriers is important for understanding the ultrafast dynamics of atomic motion [6, 8, 10, 45, 58]. Additionally, in materials like semiconductors a high excitation carrier density can induce a phase transformation to a metallic state which increases the optical reflectivity [77, 78]. If the phase transition happens in a time-scale shorter than the time for energy transfer from carriers to the lattice, it is usually called non-thermal melting. During this process, ions are movable like liquid, though not due to increase in the lattice temperature.

In this chapter, I present similar experiments to those discussed in Chap. VIII but with higher excitation using an amplified Ti:sapphire laser. Highly nonlinear behavior is observed for excitation densities above $\sim 5 \times 10^{19}$ cm^{-3}. The carrier peak shows strong saturation as function of fluence in the counter-propagating pump-probe data, whereas the reflectivity signal behaves almost linearly in the conven-

Incident power (mW)	10	40	120	250
Absorbed fluence (μJ/cm^2)	11	48	130	285
Excitation density (cm^{-3})	3×10^{19}	1×10^{20}	4×10^{20}	8×10^{20}

Table 9.1: Corresponding absorbed fluence and excitation density at various incident power.

tional pump-probe data. The acoustic signal becomes more and more symmetric, approaching bipolar as excitation increases. The diffusion may become slower and recombination become faster when a large number of carriers is excited. In addition, the same side pump-probe data for 35 nm film shows overall negative values for the relative change in reflectivity ($\Delta R/R$) under high excitation, even for the peak values (referred to at low excitation as a carrier peak). The detailed explanation of these behaviors is not clear; however, I present the results and a discussion of the present state of knowledge. Further experiments and simulations are required to gain a deeper understanding.

For convenience, Table 9.1 lists the absorbed fluence and excitation density corresponding to various incident powers.

9.1 Surface pump for thick Bi films

The thick films in this section range from 185–385 nm. The surface-pump-surface-probe data shows linear behavior up to excitation density $\sim 10^{20}$ cm^{-3} as in Fig. 9.1(a). Features of carrier peak and lattice heating are similar to the data at low excitation density. As fluence increases, phonon softening becomes prominent. The 12th oscillation peak in the 50 mW data lines up with the 12th valley in the 5 mW data, shown in Fig. 9.1(c) . This frequency chirp is attributed to the electronic contribution that softens the atomic bonding [8]. The A_{1g} frequency derived by fast Fourier transform is 2.80 THz for 5 mW and 2.54 THz for 50 mW within ~0–20 ps

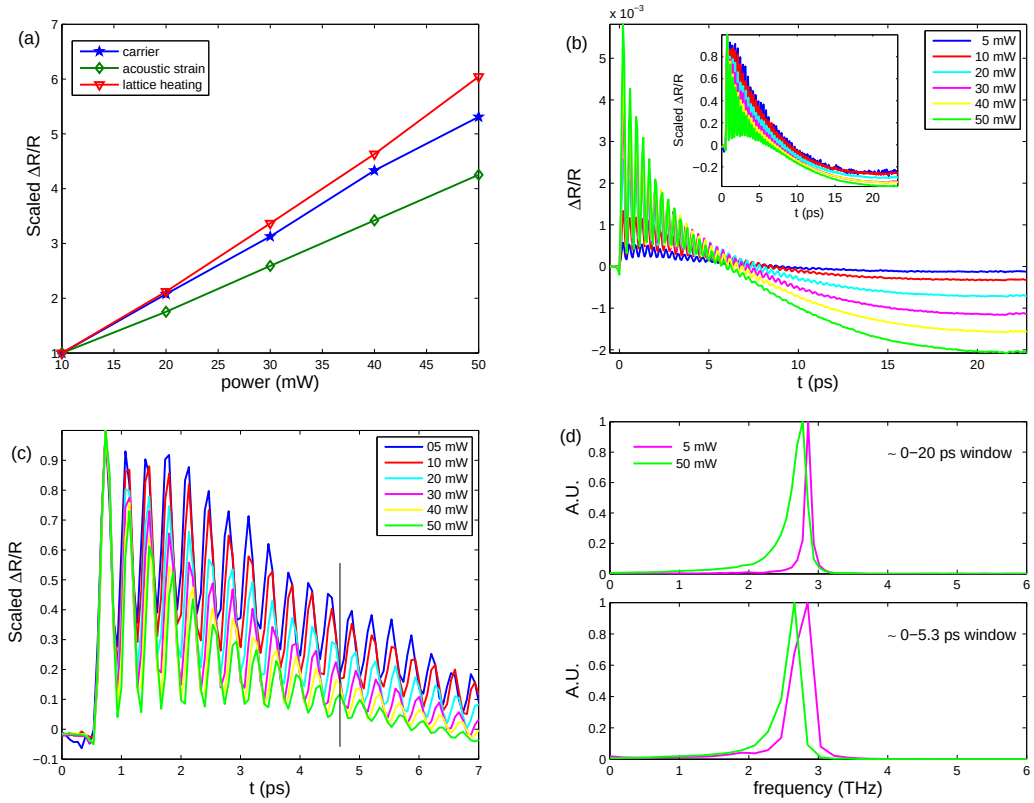

Figure 9.1: Surface-pump-surface-probe data for 185 nm film at various excitation power. (a) Peak intensity versus incident power. Each component is scaled by the maximum intensity at 10 mW from carrier peak, acoustic strain and lattice heating signals. (b) Reflectivity signal of A_{1g} optical phonon oscillation. The inset is scaled to its maximum peak amplitude, which is the first oscillation peak here. The inset shows that the reflectivity reaches below zero signal earlier as power increases. (c) Oscillation of first ∼18 cycles. (d) Fast Fourier transform of A_{1g} phonon within different windows.

window. For the first 14 cycles, the softening is more clear as the frequency is 2.63 THz for 5 mW and 2.43 THz for 50 mW. In addition to the phonon softening, another difference from low excitation is the fact that the relative change in reflectivity falls below zero faster at higher excitation, as shown in Fig. 9.1(b). However, the distinction between faster recombination or faster carrier diffusion is not straightforward, due to the lattice heating signal and the acoustic strain propagating across the laser absorption depth.

	10 mW	40 mW	120 mW	250 mW
D_e ($cm^2/2$)	30	22	20	18
τ ($=1/\gamma$ ps)	16	15	14	13

Table 9.2: Method 1: Diffusivity and recombination fit for 385 nm film measured from surface-pump-interface-probe geometry at various power, derived by the first scaling method discussed in the text.

On the other hand, the surface-pump-interface-probe data is different from the surface-pump-surface-probe data. Fig. 9.2(a) shows a carrier peak due to a combination of carrier diffusion and recombination in 385 nm film under various excitations, scaled to the peak amplitude. The peak time, t_p, is delayed and the decay (10 ps $< t <$ 50 ps) becomes faster at higher excitation density. Fig. 9.2(b) displays the nonlinear behavior of carrier peak at high excitation.

To analyze the data using the simple diffusion decay model of eq.8.1, I use two scaling methods to obtain $(\partial R/\partial n)/R$ for various value of fluence. Assume linear absorption such that the carrier density excited from the surface goes linearly with excitation power. Since the shape of the carrier peak is determined by the diffusion and recombination, the first method is to fit the shape and force the simulation to match the height of each peak. For the second method, the strong saturation of the carrier peak is determined by using a constant scaling factor between the simulation and the data for different excitation powers. This constant factor can be derived from the simulation and the data at lowest excitation power.

If the data is modeled by the first method using eq.8.1 and the simulated signal is convoluted with the probe profile, the fit for 385 nm film with various excitation powers is summarized in Table 9.2. The diffusion becomes slower and recombination becomes faster as excitation increases.

The fit in Table 9.2 scales the simulation to match the peak intensity of the data,

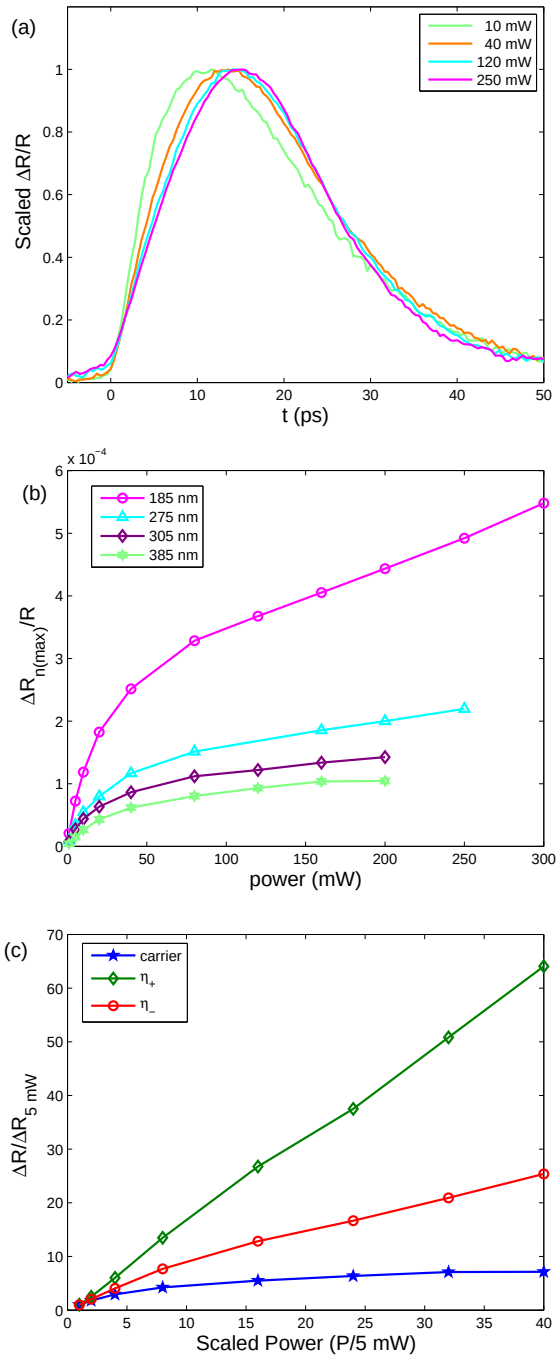

Figure 9.2: (a) Surface-pump-interface-probe data for 385 nm film at various excitation densities. The peak time is delayed as density increases. $\Delta n \sim 3\times 10^{19}$ cm^{-3} is estimated from incident power of 10 mW assuming linear absorption. (b) The peak intensity versus excitation power for various thickness. (c) Peak intensity of carrier, bipolar acoustic in negative signal (η_-) and positive signal (η_+). Each data point is scaled to the signal at lowest power, 5 mW.

Bi100 (385 nm)	D_e (cm^2/s)	τ (ps)
010 mW ($\Delta n \approx 1.5 \times 10^{19} cm^{-3}$)	30	16
040 mW ($\Delta n \approx 1.2 \times 10^{20} cm^{-3}$)	18	12
120 mW ($\Delta n \approx 3.6 \times 10^{20} cm^{-3}$)	12	10
250 mW ($\Delta n \approx 6.0 \times 10^{20} cm^{-3}$)	10	9
Bi105 (305 nm)	D_e (cm^2/s)	τ (ps)
010 mW ($\Delta n \approx 1.5 \times 10^{19} cm^{-3}$)	26	21
040 mW ($\Delta n \approx 1.2 \times 10^{20} cm^{-3}$)	12	14
120 mW ($\Delta n \approx 3.6 \times 10^{20} cm^{-3}$)	8	11
250 mW ($\Delta n \approx 6.0 \times 10^{20} cm^{-3}$)	6	10
Bi90 (275 nm)	D_e (cm^2/s)	τ (ps)
010 mW ($\Delta n \approx 1.5 \times 10^{19} cm^{-3}$)	28	20
040 mW ($\Delta n \approx 1.2 \times 10^{20} cm^{-3}$)	12	15
120 mW ($\Delta n \approx 3.6 \times 10^{20} cm^{-3}$)	8	11
250 mW ($\Delta n \approx 6.0 \times 10^{20} cm^{-3}$)	6	10
Bi50 (185 nm)	D_e (cm^2/s)	τ (ps)
010 mW ($\Delta n \approx 1.5 \times 10^{19} cm^{-3}$)	18	18
040 mW ($\Delta n \approx 1.2 \times 10^{20} cm^{-3}$)	10	10
120 mW ($\Delta n \approx 3.6 \times 10^{20} cm^{-3}$)	6	7
250 mW ($\Delta n \approx 6.0 \times 10^{20} cm^{-3}$)	4	7

Table 9.3: Method 2: Diffusivity and recombination fit for various film thicknesses measured from surface-pump-interface-probe geometry at various power, derived by the second scaling method described in the text.

and the best fit is determined by the best match to the shape of carrier peak. If, however, the second method is used with a constant scaling factor derived from the ratio between the 10 mW data and the simulation, the fit for various films at different powers is summarized in Table 9.3. In this case, the best fit is determined by the best match for peak intensity. The second fit results also show that the diffusion becomes slower while the recombination is faster at higher excitation density.

Comparing Table 9.2 with Table 9.3 for 385 nm film, faster decay and slower diffusion appear in both methods as excitation increases. The derived carrier recombination does not differ significantly between the two methods. However, the second scaling method is more sensitive to the fit parameters. Nonlinearities are observed

in the peak intensity for thick films as a function of fluence shown in Fig. 9.2(b) and 9.2(c). Between 5 mW and 200 mW, the intensity of carrier peak grows to a value at least a factor of 5 less than the value it would have attained assuming linear growth.

Fig. 9.3 displays the comparison between surface-pump-surface-probe data and surface-pump-interface-probe data for 185 nm film at 3 different powers. The ratio between carrier peaks for surface-probe and interface-probe data decreases with increasing excitation, consistent with the saturation observed in carrier peak for interface-probe data. The bipolar nature of acoustic strain becomes more distinct as power increases. Denote the maximum value of the relative change in reflectivity as η_+ and minimum value as η_- for the bipolar acoustic strain in the interface-probe data. The nonlinearity of η_+ and η_- as functions of fluence is shown in Fig. 9.2(c). The η_- is slightly saturated while the η_+ increases as a function of excitation with slope greater than 1. It is also evident from Fig. 9.3 that for film thicker than 185 nm, there is no indication of lattice heating from the interface.

Using the carrier two-decay model in eq.8.9–eq.8.11 and assuming that diffusivity as well as recombination are density-independent, the lattice thermalization time is found to be $\sim$1.5 ps. Comparing recombination time in Table 9.3 with lattice thermalization time, it is not yet clear whether lattice thermalization is due to fast carrier cooling leading to a cold plasma, or a density-dependent Auger-type recombination from an increase in phonon-mediated recombination due to lattice heating. Support for the hypothesis of faster recombination comes from the increasing symmetry of the acoustic strain. Since the acoustic strain is a superposition of bipolar thermal strain and unipolar non-thermal strain, its symmetric profile indicates that thermal strain is the dominate component at high excitation. This is consistent with the carrier saturation observed from the surface-pump-interface-probe data.

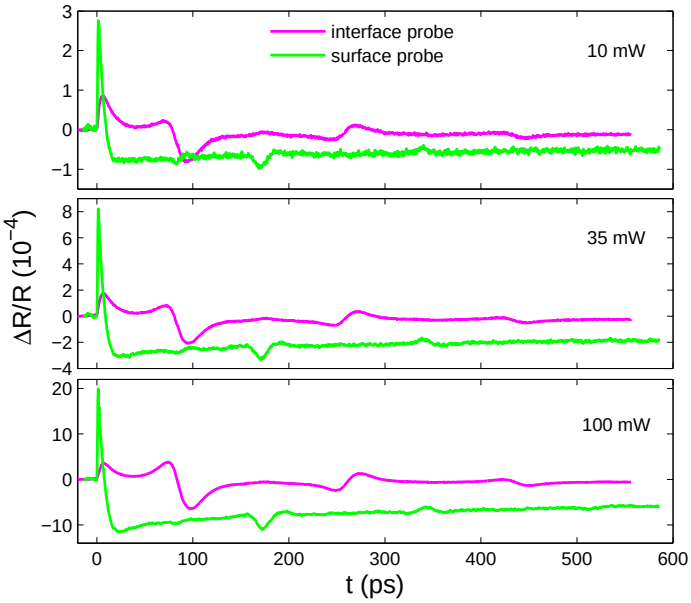

Figure 9.3: Comparison between surface-pump-surface-probe (green) and surface-pump-interface-probe (magenta) data at various power.

9.2 Interface pump surface probe for thick films

Owing to many factors, the interface-pump-surface-probe results are more complex at high excitation. The nonlinearity of the carrier peak as a function of fluence is quantitatively similar to the surface-pump-interface-probe data. In addition to the highly nonlinear carrier behavior, the acoustic strain has more features as shown in Fig. 9.4(a). The decay of the carrier peak is different than in the surface-pump-surface-probe data, partially due to the different boundary conditions as discussed in Chap. VIII. The boundary condition also results in a different width of acoustic signal. Most features are similar to the low excitation region; however, the dip close to the sharp η_- trough makes the high excitation region more complex. Neither standard Thomsen's model nor the version incorporating a one- or two-decay model can explain this feature. Fig. 9.4(b) is the signal of interface pump and surface

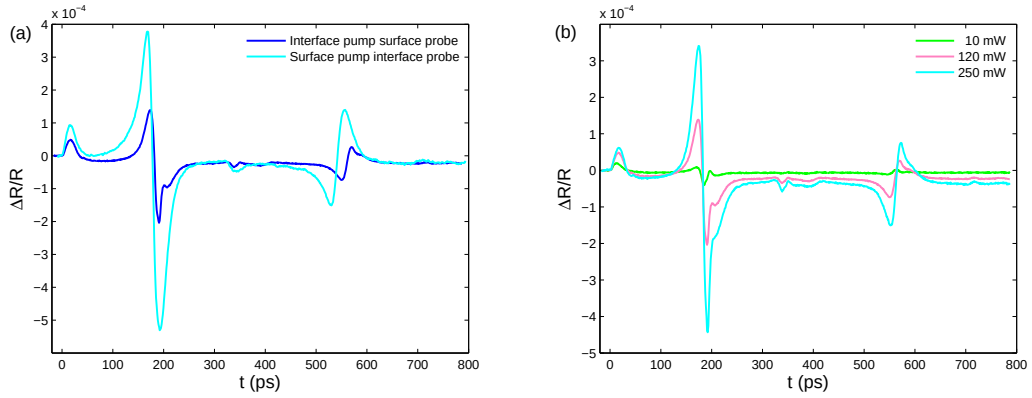

Figure 9.4: Comparison between different geometries and among various fluence for 385 nm film. (a) Comparison between surface-pump-interface-probe and interface-pump-surface-probe data at 120 mW. (b) Power-dependence signals from interface-pump-surface-probe geometry.

probe at various powers. The acoustic strain is nearly unipolar at low excitation and becomes symmetric bipolar at higher excitation.

The small peak in Fig. 9.4(a) and 9.4(b) around $t = 350$ ps is attributed to non-thermal strain. Its nonlinear behavior is similar to the carrier peak. However, due to its weak signal, the bipolar profile is not clearly distinguished. The shape of peak is more bipolar for 250 mW data in Fig. 9.4(b), but unipolar for 10 and 120 mW data.

9.3 Surface pump surface probe for thin films

The reflectivity of thin films at high excitation is more complex than low excitation for all the pump-probe geometries. I focus on the surface-pump-surface-probe and surface-pump-interface-probe data for the 35 and 66 nm films. What was referred to as a carrier peak for positive values of relative change in reflectivity now appears below zero for highly excited 35 nm film, shown in Fig. 9.5(a). The peak itself has lower reflectivity than the un-perturbed reflectivity when power exceeds

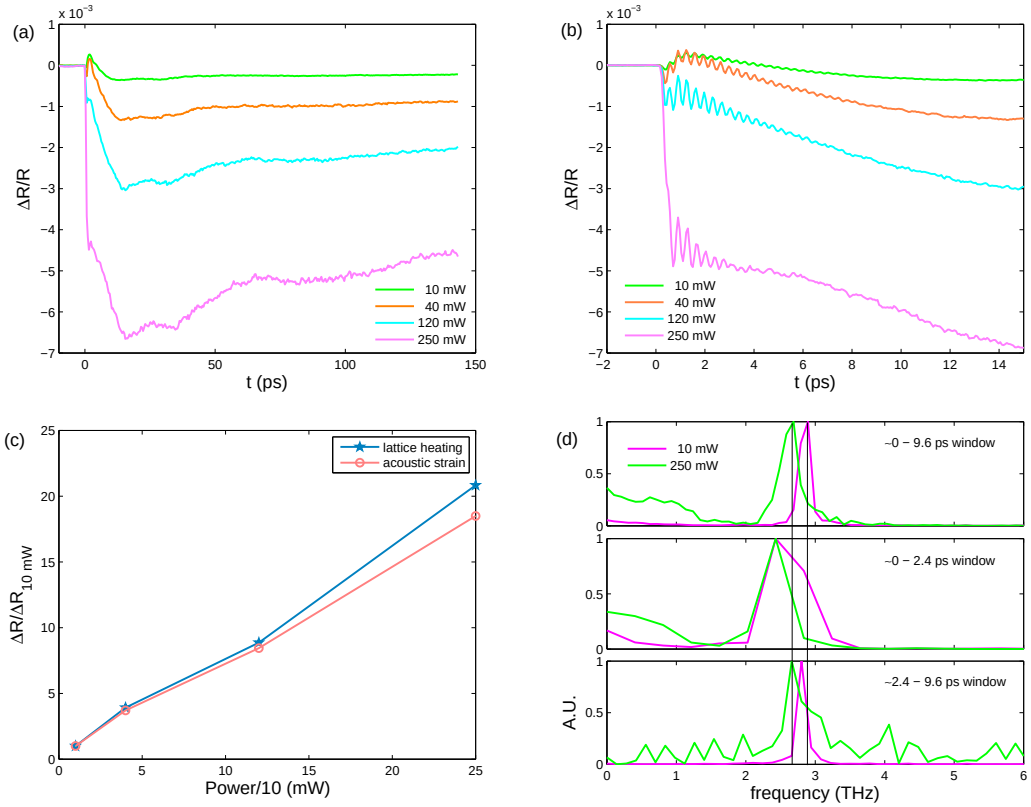

Figure 9.5: Surface-pump-surface-probe data at various power for 35 nm film. (a) Signals within long time spans. (b) Signals within short time spans at early times. Optical phonons are resolved. (c) Peak intensity as a function of incident power from lattice heating and acoustic signals. (d) Fast Fourier transform for various windows.

40 mW, and becomes indistinguishable when excitation is above 120 mW. At highest excitation of 250 mW, a rapid reflectivity drop is followed by a slower decrease, which changes in shape and takes longer to reach its minimum compared to the low excitation below 40 mW.

The overall negative signal after excitation may not be attributable to permanent damage of sample, since the carrier-like peak signal returns when low power is applied again. However, a slight difference is observed when applying low power again. Comparing the signal at low excitation without any previous application of high power to that with high excitation first, the main difference is the magnitude of

carrier peak. The overall shape of the carrier peak (rising, falling and so on) is the same.

With the modeled shape of acoustic strain derived from the thick films, the simulation can roughly model the reflectivity signal at low fluence. However, it still cannot explain the abnormal negative reflectivity for 35 nm film with $t < 20$ ps, and especially cannot explain the disappearance of carrier peak.

Fig. 9.5(b) is the optical phonon from 35 nm film. An A_{1g} oscillation is observed up to 250 mW. The damping rate of the phonon is fast for high excitation: the oscillation disappears after 6 cycles for excitation power above 40 mW, whereas more than 20 cycles are observed below 40 mW. The phonon frequency is 2.93 THz at 10 mW and 2.77 THz at 250 mW for a window around 0–9.6 ps, derived by fast Fourier transform and shown in the upper panel of Fig. 9.5(d). The 7th oscillation peak at 10 mW nearly overlaps with the 6th oscillation valley at 250 mW. The first 5-6 cycles soften more if a fast Fourier transform is made around a 0–2.4 ps window, which gives a weighted frequency ~2.67 THz at 10 mW and ~2.46 THz at 250 mW, shown in the middle panel of Fig. 9.5(d). Because 35 nm film is optically thin, the excited carriers do not diffuse but are locally confined, which may lead to higher carrier density near the surface upon excitation than in thick films. Thus before the recombination, the softening effect of atomic bonding by a dense plasma is larger in 35 nm film than in thick films.

Although the carrier peak is indistinguishable under high excitation, the results for acoustic signal with $t < 70$ ps and the results for lattice heating are nearly linear with the increasing excitation, shown in Fig. 9.5(c). This indicates that the energy transfer to the lattice is nearly linear, as well as that the absorption is not saturated at least up to 6×10^{20} cm $^{-3}$ excitation density.

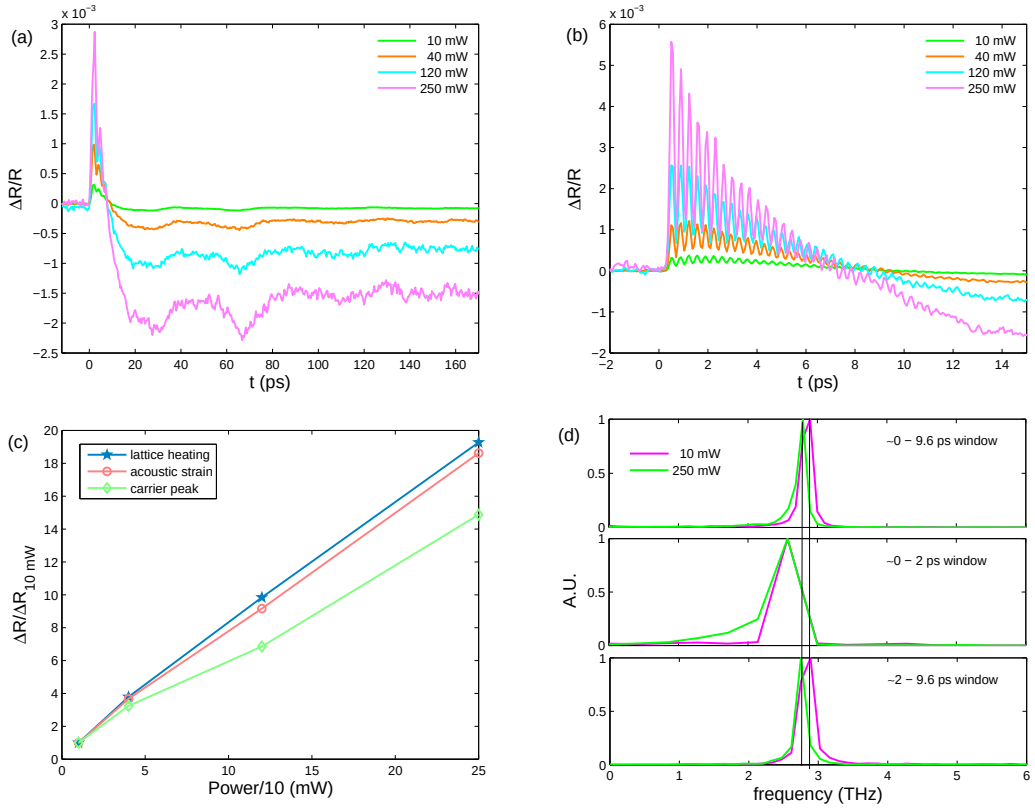

Figure 9.6: Surface-pump-surface-probe data at various power for 65 nm film. (a) Signals within long time spans. (b) Signals within short time spans at early times. Optical phonons are resolved. (c) Maximum signals as a function of incident power, including carrier peak, acoustic strain and lattice heating. (d) Fast Fourier transform for various windows.

As film approximately doubles in thickness to 66 nm, shown in Fig. 9.6, the normal positive-valued carrier peak reappears, even at 250 mW high excitation. The acoustic echoes are also observed at various excitations for 66 nm film. The fast Fourier transform gives A_{1g} (weighted) frequency ∼2.93 THz at 10 mW and ∼2.86 mW at 250 mW for the window near $0 < t < 9.6$ ps. For first 5–6 cycles, the (weighted) frequency is ∼2.65 THz at 10 mW and ∼2.53 THz at 250 mW. Frequency is highly chirped for the first few cycles due to a high density of photoexcited carriers that alters the interatomic potential energy and softens the atomic bonding. As excitation increases, the carrier peak, acoustic strain and lattice heating are nearly

linear with a slope slightly smaller than 1. The linearity of acoustic strain and lattice heating are similar to the 35 nm film. Thus it is straightforward to expect linear absorption for various film thicknesses up to 6×10^{20} cm^{-3} excitation density.

The reflectivity drops below zero earlier as excitation increases, indicating a faster recombination or faster diffusion. However, from analysis of surface-pump-interface-probe data of thick films, the recombination is faster while diffusion could be slower. In conclusion, surface-pump-surface-probe data for 66 nm film at high excitation is similar to that at low excitation, but with highly chirped A_{1g} phonons and perhaps faster recombination or diffusion.

9.4 Surface pump interface probe for thin films

Similar to surface-pump-surface-probe data, surface pump interface probe data for 35 nm film displays the abnormal negative carrier peak when incident power is greater than 20 mW, shown in Fig. 9.7(a) for original data and Fig. 9.7(b) for scaled data. Although signals earlier than 20 ps are referred to as carrier peaks at low excitation, the abnormal peak might not be a carrier peak from the observation of high excitation data. The reason for the peak before 20 ps for 35 nm film is so far not clear. From the fact that the surface probe and the interface probe data are out of phase, show in Fig. 9.8(a) and Fig. 9.8(b), the peak could be due to the acoustic strain. One possible explanation for the overall negative signal including carrier peak is a fast carrier recombination at early times. In this scenario a huge amount of excited electron-hole plasma recombines rapidly and transfers the energy into the lattice, reducing the reflectivity upon excitation. This fast recombination could also caused by the density-dependent Auger recombination. However, the mechanism is not clear at present due to the unexplained disappearance of the carrier peak (t

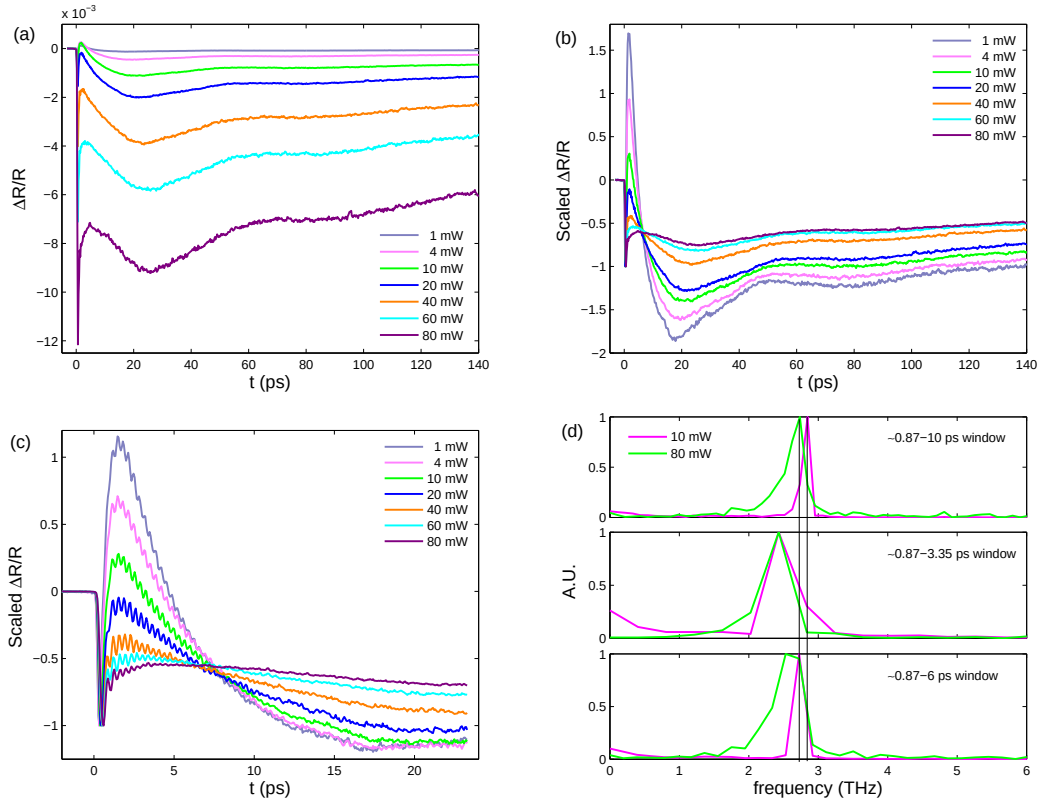

Figure 9.7: Surface-pump-interface-probe data for 35 nm at various power. (a) Data include carrier, acoustic and thermal components. (b) Data as in (a) is normalized to the time zero (dip) signal. (c) Optical phonon with data normalized to the time zero dip signal. (d) Fast Fourier transform within various windows at 10 and 80 mW.

$<$ 20 ps) at high excitation for surface-pump-surface-probe data, and due to the acoustic-like peak (t $<$ 20 ps) for the surface-pump-interface-probe data.

Due to the partial overlap between pump and probe profiles, optical phonon oscillation is also observed in surface-pump-interface-probe for 35 nm film, shown in Fig. 9.7(c). Fig. 9.7(c) is scaled to the initial drop/dip of reflectivity. The fast Fourier transform within window 0.87–10 ps gives a weighted frequency ∼2.92 THz at 10 mW and 2.88 THz at 80 mW. The first 10 cycles around window $0.87 < t < 3.35$ ps experience more softening, and a fast Fourier transform gives ∼2.83 THz at 10 mW and ∼2.55 THz at 80 mW.

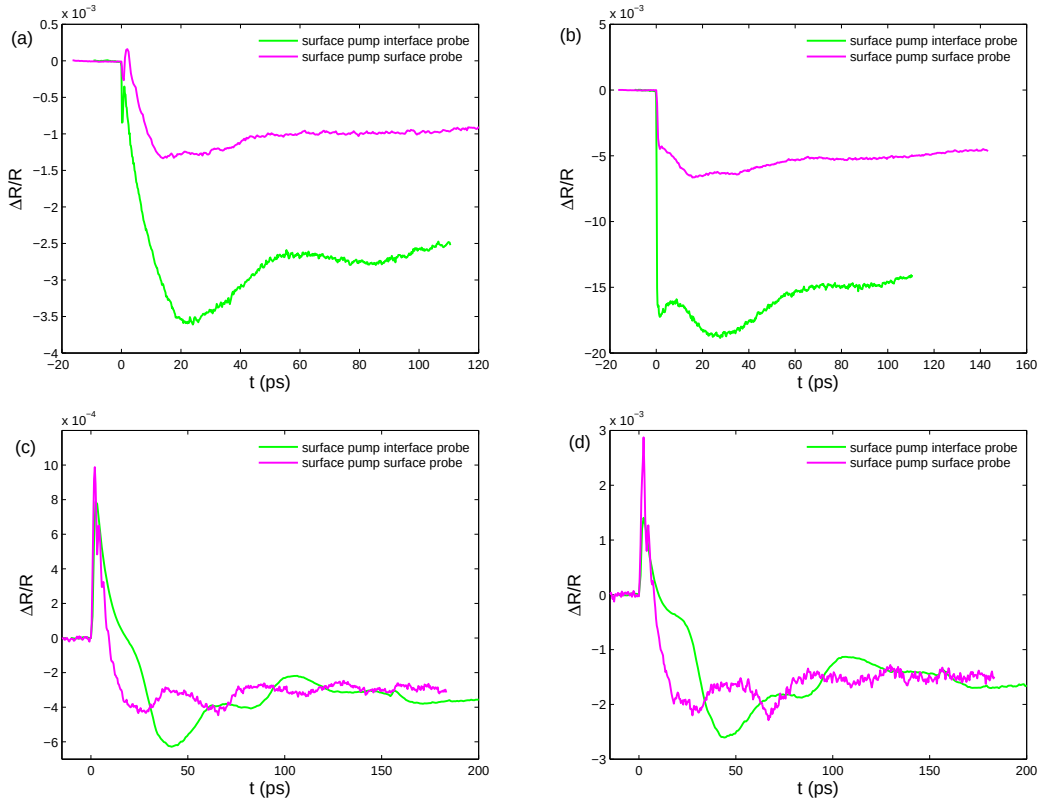

Figure 9.8: Surface-pump-surface-probe and surface-pump-interface probe data for 35 and 66 nm films at low and high excitation. (a) 35 nm at 10 mW. (b) 35 nm at 250 mW. (c) 66 nm at 10 mW. (d) 66 nm at 250 mW. Power indicated here is incident power.

Fig. 9.9 shows surface-pump-interface-probe data for 66 nm film at various powers. Similar features for each component are observed in both surface-pump-surface-probe and surface-pump-interface-probe data, as shown in Fig. 9.8(c) and Fig. 9.8(d). However, no optical phonon is observed in interface probe data due to zero group velocity of the A_{1g} phonon as well as to the separated pump and probe profiles. The acoustic echoes in interface probe data are out of phase with the echoes observed in the surface probe data. The acoustic strain and lattice heating signals vary linearly as a function of incident power. However, the carrier peak intensity at $t = t_p$ is reduced by up to a factor of 5 compared with the linear prediction, an effect

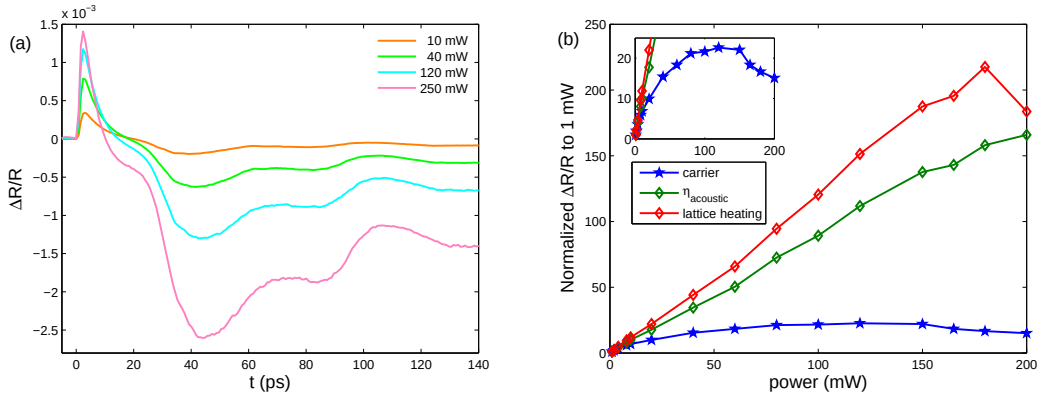

Figure 9.9: Surface-pump-interface-probe data at various power for 66 nm film. (a) Data are normalized to the dip signal at time zero. (b) Maximum signals as a function of incident power, including carriers, acoustic strains and lattice heating.

also observed in thick film for surface-pump-interface-probe data.

9.5 Conclusion of high excitation and comparison with low excitation

The surface-pump-interface-probe data indicates that cooling of the carriers occurs by heat transfer to the lattice in a time less than 3 ps and that the carriers reaching the back surface of the film are relatively cold, compared to the initial photo-excited plasma. The surface pump-probe signal drops below zero after about 10-20 ps, with a slow recovery on the nanosecond time-scale. This initial drop is caused by acoustic strain propagation from the surface through the optical absorption depth, leaving a thermally expanded lattice in its wake, while the subsequent very slow decay is attributed to cooling due to heat conduction. It is observed that the background reflectivity change due to this thermal expansion is much greater at the surface of the film than the corresponding background at the interface. This indicates that lattice heating must occur faster than the time (less than 3 ps) taken for diffusion to produce a uniform plasma in the 185 nm thick film. This is consis-

tent with electron diffraction measurements of thin films reported in Ref. [73] that suggest a lattice heating time of $2 - 2.5$ ps. Thus, although the plasma cools in less than 3 ps, its density decays with a much longer time constant (10-30 ps). This indicates that the decay of the plasma density is determined by the electron-hole recombination rate, and it is therefore estimated that recombination time is of the order of 20 ps for incident power less than 40 mW, i.e. $\sim 10^{19}$ cm^{-3} excitation density.

However, for the carrier density $\gtrsim 10^{20}$ cm^{-3}, the dynamics become more complex. The peak intensity of the carrier signal saturates, and the peak time t_p becomes longer and carrier recombination becomes faster. On the other hand, for the surface pump and probe, the maximum (carrier density) and minimum (thermal) component of the relative reflectivity remain linear up to much higher fluence. It is not clear at what level this signal saturates due to potential artifacts at the highest fluence for the surface probe. Nonetheless, it appears that at high densities the recombination and diffusion become nonlinear. The increased plasma decay rate in the initial dense plasma reduces the amplitude $\Delta R_{n(max)}/R$ of the carrier peak of the counter-propagating reflectivity at $t = t_p$ by up to a factor of 5 at the highest fluences, indicating that the plasma density decays at an average rate of 0.3 ps^{-1} at early times ($t < 5$ ps), comparable to the rate of heat transfer to the lattice. At this point, the nature of the nonlinearity cannot be determined without further experiments and more sophisticated analysis (for example to distinguish Auger recombination from an increase in phonon-mediated recombination due to lattice heating).

CHAPTER X

Summary

In this thesis, I present both carrier and thermal transport studies of various thickness Bi films grown on sapphires. Ultrafast lasers are used to photoexcite carriers in the near surface region of the film. The optical reflectivity is monitored by a weak laser probe, in order to investigate the modulation contributed by photoexcited carriers, acoustic strains, and lattice heating. Lattice changes are also studied using time-resolved x-ray diffraction. The change in atomic structure due to laser heating is directly probed by x rays for long time scales (up to a few hundred nanoseconds).

Counter-propagating pump-probe geometry is used in optical measurements to separate the modulations of the dielectric constant due to carriers, acoustic strain, and lattice heating, which are difficult to distinguish in conventional pump-probe measurements. In counter-propagating pump-probe geometry, optical phonons have zero group velocity and do not propagate out of the excitation region, making them unobservable in thick films. In addition, the modulation from lattice heating is not observed for films thicker than 185 nm up to a few hundred nanosecond, owing to rapid heating at the surface and relatively slow thermal diffusion. I also find that the carriers diffuse to the back surface several times faster than the speed of sound. The carrier peak including carrier diffusion and recombination is thus easily

distinguishable for film thicknesses above 185 nm and can be analyzed by a simple diffusion and decay model at low excitations.

The x-ray measurements using grazing incident geometries are capable of measuring inhomogeneous temperature across film. In addition, symmetric diffraction measures temperature changes averaged over the entire films. Therefore, a combination of the two x-ray geometries is useful for thermal transport studies.

From both optical and x-ray studies, a fast lattice thermalization is confirmed from that fact that heat deposit near the surface of films results in a large thermal gradient. Lattice thermalization time is in the range between 0.8–1.5 ps, derived from comparison between the simulations and the data at high and low excitation ($\sim 10^{18}$ cm^{-3}–10^{20} cm^{-3}). The thermal profile is possibly twice as broad as laser penetration depth at 800 nm wavelength, analyzed from the modified acoustic strain generation. This could be attributed to the fast carrier diffusion that spreads the thermal profile before energy of photoexcited carriers transfers to the lattice. The fast carrier diffusion is about 25 cm^2/s at excitations below 5×10^{19} cm^{-3}, from counter-propagating pump-probe measurements.

In addition to carrier transport, thermal transport across the Bi/sapphire interface is studied, and the Kapitza conductance is derived to be 2000 ± 1000 W/cm^2/s/K averaged over the various film thicknesses. A large thermal gradient is observed immediately after excitation from the grazing incidence data in thick film (284 nm). The observed plateau from symmetric diffraction measurements of Bragg angle changes is in good agreement with the thermal conductivity being the same as the measured bulk value. However, for the thinnest film (65 nm) the thermal profile is found to be nearly uniform within the 100 ps time resolution of the x-ray probe, whereas one would expect it to take $\sim$ 650 ps if the initial heat deposition were limited to the

$\sim$ 15 nm laser penetration depth. This apparent inconsistency is resolved given the relatively large ambipolar diffusivity and finite lattice thermalization time.

This dissertation provides a broad and general understanding of photoexcited Bi films, as well as detailed studies of carriers, acoustic strains and lattice heating at low excitation by optical pump-probe experiments. In addition, a clear understanding of thermal transport across the Bi/sapphire interface by time-resolved x-ray diffraction under the damage threshold is presented. However, some open questions remain. In this summary, I point out these questions and some limitations of the optical and x-ray techniques, as a starting point for further studies.

10.1 Nonlinear carrier and acoustic dynamics

When excitation density increases, the dynamics become complex, and the studies presented in this dissertation open some questions. As excitation rises above 5×10^{19} cm^{-3}, carrier dynamics become nonlinear. Carrier peaks observed from the counter-propagating pump-probe measurements reduce their intensity by a factor of 5 at the highest excitation, below what would be expected if the dynamics were linear, whereas signals measured by the conventional pump-probe geometry are nearly linear with increasing excitation densities. This reduction could be due to the combination of reduced carrier diffusivity and faster recombination, analyzed from both shape and intensity of carrier peaks. From the current studies, we cannot distinguish whether the diffusivity and recombination rates are explicitly dependent on carrier density or lattice temperature. For example, the recombination rate could increase due to Auger processes from the increased phonon population with lattice temperature.

As mentioned above the studies does not allow us to allowing to discriminate the factor resulting in reduced carrier peak intensity, at least given the existing

model of our data. Three parameters have been used in the simulation, i.e. lattice thermalization time, decay rate, and carrier diffusivity. For thick film, the only way to better fit the data is to add more parameters. From a mathematical point of view, this might yield a better result, but we would probably not gain additional insights into the physics. For thin film, localizing the photoexcited carriers could potentially rule out the contribution from both carrier and thermal diffusion, eliminating one parameter (carrier diffusivity) from the model. However, modulation from acoustic strains is large in Bi and cannot be ignored. For thick films, acoustic strain can be well modeled phenomenologically at both low and high excitation, but for thin films, we are not able to model it effectively at high excitation. Thus although it might appear that restricting to thin film simplifies the model by eliminating carrier diffusivity, the situation is in fact complicated by the incompletely-understood dynamics of acoustic strain.

While the current model cannot explicitly incorporate the acoustic strain, a qualitatively understanding can be gained from the analysis of thermal and non-thermal contributions in thick films. The shape of acoustic strain becomes more symmetric at higher excitation. The asymmetric nature at low excitation is attributed to the combination of thermal and non-thermal strains generated via lattice heating and deformation potential couplings respectively. The bipolar nature of acoustic strain at high excitation is indirect evidence of a very fast carrier recombination rate that reduces the non-thermal strain generation. As a result, the acoustic strain generated at high excitation is contributed mostly by lattice heating and is nearly symmetric, resulting from the relatively slow lattice thermal diffusion of Bi. The fast recombination rate thus reduces the ratio between non-thermal and thermal strain. This is consistent with the carrier saturation observed from counter-propagating pump-probe data for

film thicknesses above 66 nm. Therefore, a fast carrier recombination rate or a density dependent Auger recombination is suggested but not numerically implemented, for the reason discussed in the preceding paragraph. The problem remains unless we can find an alternative measurement (temperature-dependent pump-probe measurements including conventional and counter-propagating geometries) or a different model (density-dependent diffusion and recombination)

10.2 Improvements of thermal transport studied by Time-resolved x-ray diffraction

There are several areas where the x-ray measurements would obviously be improved including shorter x-ray pulse duration, higher laser repetition rate allowing for better statistic, and less intense excitation as well as better fluence control. However, there are also non-source related improvements that can be made including appropriate sample design to reduce the free parameters and simplify the problem. It is in practice difficult to determine whether the temperature decay is dominated by the thermal conductivity or by the Kapitza conductance, especially when both parameters are unknown. Different combinations of both thermal conductivity and Kapitza conductance can lead to similar temperature evolutions, resulting in similar time-resolved diffraction signals, even given the depth dependence of the grazing incidence probe and especially given the finite time-resolution. The ambiguity arising from those combinations can be eliminated by better time resolution to resolve a fast temperature decay and using thinner film to increase the temperature jump across an interface.

If time-resolution is not limited and film is thin (but not thin enough to incur small size effect), depth- and time-resolved x-ray diffraction can measure temperature

profile for both film and substrate separately. Therefore, film thermal conductivity and Kapitza conductance across the interface can be derived numerically.

For structures such as superlattices, time-resolved x-ray diffraction can measure the effective thermal conductivity of the whole superlattice. Therefore, the phonon population and transmission can be mapped out. The study of reduced thermal conductivity in superlattices has potential for thermoelectric materials, such as Bi, its alloys, and their heterostructures.

BIBLIOGRAPHY

BIBLIOGRAPHY

[1] Y. M. Sheu, S. H. Lee, J. K. Wahlstrand, D. A. Walko, E. C. Landahl, D. A. Arms, M. Reason, R. S. Goldman, and D. A. Reis. Thermal transport in a semiconductor heterostructure measured by time-resolved x-ray diffraction. *Physical Review B (Condensed Matter and Materials Physics)*, 78(4):045317, 2008.

[2] M. Highland, B. C. Gundrum, Yee Kan Koh, R. S. Averback, David G. Cahill, V. C. Elarde, J. J. Coleman, D. A. Walko, and E. C. Landahl. Ballistic-phonon heat conduction at the nanoscale as revealed by time-resolved x-ray diffraction and time-domain thermoreflectance. *Phys. Rev. B*, 76:075337, 2007.

[3] D. G. Cahill, W. K. Ford, et al. Nanoscale thermal transport. *J. Appl. Phys.*, 93(22):793–818, 2003.

[4] H. J. Zeiger, J. Vidal, T. K. Cheng, E. P. Ippen, G. Dresselhaus, and M. S. Dresselhaus. Theory for displacive excitation of coherent phonons. *Phys. Rev. B*, 45(2):768–778, Jan 1992.

[5] M. Hase, K. Mizoguchi, H. Harima, S. Nakashima, M. Tani, K. Sakai, and M. Hangyo. Optical control of coherent optical phonons in bismuth films. *Applied Physics Letters*, 69(17):2474–2476, 1996.

[6] Muneaki Hase, Masahiro Kitajima, Shin-ichi Nakashima, and Kohji Mizoguchi. Dynamics of coherent anharmonic phonons in bismuth using high density photoexcitation. *Phys. Rev. Lett.*, 88(6):067401, Jan 2002.

[7] R. Merlin. Generating coherent THz phonons with light pulses. *Solid State Communications*, 102:207–220, April 1997.

[8] E. D. Murray, D. M. Fritz, J. K. Wahlstrand, S. Fahy, and D. A. Reis. Effect of lattice anharmonicity on high-amplitude phonon dynamics in photoexcited bismuth. *Phys. Rev. B*, 72(6):060301, 2005.

[9] D. M. Fritz, D. A. Reis, B. Adams, R. A. Akre, J. Arthur, C. Blome, P. H. Bucksbaum, A. L. Cavalieri, S. Engemann, S. Fahy, R. W. Falcone, P. H. Fuoss, K. J. Gaffney, M. J. George, J. Hajdu, M. P. Hertlein, P. B. Hillyard, M. Horn von Hoegen, M. Kammler, J. Kaspar, R. Kienberger, P. Krejcik, S. H. Lee, A. M. Lindenberg, McFarland B., D. Meyer, T. Montagne, E. D. Murray, A. J. Nelson, M. Nicoul, R. Pahl, J. Rudati, H. Schlarb, D. P. Siddons, K. Sokolowski-Tinten,

Th. Tschentscher, D. von der Linde, and J. B. Hastings. Ultrafast bond softening in bismuth: Mapping a solid's interatomic potential with x-rays. *Science*, 315:633–636, February 2 2007.

[10] D. Boschetto, E. G. Gamaly, A. V. Rode, B. Luther-Davies, D. Glijer, T. Garl, O. Albert, A. Rousse, and J. Etchepare. Small atomic displacements recorded in bismuth by the optical reflectivity of femtosecond laser-pulse excitations. *Phys. Rev. Lett.*, 100(2):027404, 2008.

[11] C. Thomsen, H. T. Grahn, H. J. Maris, and J. Tauc. Surface generation and detection of phonons by picosecond light pulses. *Phys. Rev. B*, 34(6):4129–4138, Sep 1986.

[12] Eeuwe S. Zijlstra, Larisa L. Tatarinova, and Martin E. Garcia. Laser-induced phonon-phonon interactions in bismuth. *Physical Review B (Condensed Matter and Materials Physics)*, 74(22):220301, 2006.

[13] B. W. Batterman and H. Cole. Dynamical diffraction of X rays by perfect crystals. *Rev. Mod. Phys.*, 36(3):681–716, 1964.

[14] A. Gibaud and S. Hazra. X-ray reflectivity and diffuse scattering. *Current Science*, 78(12):1467–1477, 2000.

[15] M. Hase, M. Kitajima, S. Nakashima, and K. Mizoguchi. Coherent phonons: Electronic softening or anharmonicity? hase *et al.* reply. *Phys. Rev. Lett.*, 93:109702, 2004.

[16] A. Hanisch, B. Krenzer, T. Pelka, S. Möllenbeck, and M. Horn von Hoegen. Thermal response of epitaxial thin Bi films on Si(001) upon femtosecond laser excitation studied by ultrafast electron diffraction. *Phys. Rev. B*, 77(12):125410, 2008.

[17] Stuart Golin. Band structure of bismuth: Pseudopotential approach. *Phys. Rev.*, 166(3):643–651, Feb 1968.

[18] W. J. de Haas and P. M. van Alphen. *Comm. Phys. Lab. Leiden*, Nos. 208d, 212a, 1930.

[19] X. Gonze, J.-P. Michenaud, and J.-P. Vigneron. First-principles study of As, Sb, and Bi electronic properties. *Phys. Rev. B*, 41(17):11827–11836, Jun 1990.

[20] R. I. Sharp and E. Warming. The lattice dynamics of antimony. *J. Phys. F: Met. Phys.*, 1(1):570–587, 1971.

[21] N. W. Ashcroft and N. D. Mermin. *Solid State Physics*. Thomson Learning, Inc.

[22] Shoichi Mase. Electronic structure of bismuth type crystals. *Journal of the Physical Society of Japan*, 13(5):434–445, 1958.

[23] Morrel H. Cohen. Energy Bands in the Bismuth Structure. I. A Nonellipsoidal Model for Electrons in Bi. *Phys. Rev.*, 121(2):387–395, Jan 1961.

[24] J. Rose and R. Schuchardt. A theoretical investigation of the fermi surfaces of bismuth and antimony. *Physica Status Solidi (b)*, 117(1):213–224, 1983.

[25] M. Giura and R. Marcon. Band structure of the holes in bismuth. *Phys. Rev. B*, 1(4):1528–1532, Feb 1970.

[26] R. T. Bate, N. G. Einspruch, and P. J. May. Galvanomagnetic Studies of Sn-Doped Bi. II. Negative Fermi Energies. *Phys. Rev.*, 186(3):599–608, Oct 1969.

[27] P. Y. Wang and A. L. Jain. Modulated piezoreflectance in bismuth. *Phys. Rev. B*, 2(8):2978–2983, Oct 1970.

[28] A. A. Lopez and S. H. Koenig. Electron-hole recombination in bismuth below 20° K. *Solid State Communications*, 4(1):513–517, 1966.

[29] N. W. Ashcroft and N. D. Mermin. *Solid State Physics*, page 454. Thomson Learning, Inc., 1976.

[30] C. Kittel. *Introduction to Solid State Physics*. John Wiley & Sons.

[31] N. W. Ashcroft and N. D. Mermin. *Solid State Physics*, pages 498–499. Thomson Learning, Inc., 1976.

[32] B. Abeles. Lattice thermal conductivity of disordered semiconductor alloys at high temperatures. *Phys. Rev.*, 131(5):1906–1911, Sep 1963.

[33] M. A. Afromowitz. Thermal conductivity of $Ga_{1-x}Al_xAs$ alloys. *J. Appl. Phys.*, 44(3):1292–1294, 1973.

[34] Takafumi Yao. Thermal properties of AlAs/GaAs superlattices. *Appl. Phys. Lett.*, 51(22):1798–1800, 1987.

[35] W. S. Capinski, H. J. Maris, T. Ruf, M. Cardona, K. Ploog, and D. S. Katzer. Thermal-conductivity measurements of GaAs/AlAs superlattices using a picosecond optical pump-and-probe technique. *Phys. Rev. B*, 59(12):8105–8113, Mar 1999.

[36] S.-M. Lee, David G. Cahill, and Rama Venkatasubramanian. Thermal conductivity of Si–Ge superlattices. *Applied Physics Letters*, 70(22):2957–2959, 1997.

[37] R. J. Stoner and H. J. Maris. Kapitza conductance and heat flow between solids at temperatures from 50 to 300 K. *Phys. Rev. B*, 48(22):16373–16387, Dec 1993.

[38] G. Chen. Thermal conductivity and ballistic-phonon transport in the cross-plane direction of superlattices. *Phys. Rev. B*, 57(23):14958–14973, Jun 1998.

[39] E. T. Swartz and R. O. Pohl. Thermal boundary resistance. *Rev. Mod. Phys.*, 61(3):605–668, Jul 1989.

[40] E. T. Swartz and R. O. Pohl. Thermal resistance at interfaces. *Applied Physics Letters*, 51(26):2200–2202, 1987.

[41] Yong-Xin Yan, Jr. Edward B. Gamble, and Keith A. Nelson. Impulsive stimulated scattering: General importance in femtosecond laser pulse interactions with matter, and spectroscopic applications. *The Journal of Chemical Physics*, 83(11):5391–5399, 1985.

[42] Y. Liu, A. Frenkel, G. A. Garrett, J. F. Whitaker, S. Fahy, C. Uher, and R. Merlin. Impulsive Light Scattering by Coherent Phonons in $LaAlO_3$: Disorder and Boundary Effects. *Phys. Rev. Lett.*, 75(2):334–337, Jul 1995.

[43] T. E. Stevens, J. Kuhl, and R. Merlin. Coherent phonon generation and the two stimulated raman tensors. *Phys. Rev. B*, 65(14):144304, Mar 2002.

[44] G. A. Garrett, T. F. Albrecht, J. F. Whitaker, and R. Merlin. Coherent thz phonons driven by light pulses and the sb problem: What is the mechanism? *Phys. Rev. Lett.*, 77(17):3661–3664, Oct 1996.

[45] É. D. Murray, S. Fahy, D. Prendergast, T. Ogitsu, D. M. Fritz, and D. A. Reis. Phonon dispersion relations and softening in photoexcited bismuth from first principles. *Physical Review B (Condensed Matter and Materials Physics)*, 75(18):184301, 2007.

[46] J. G. Fujimoto, J. M. Liu, E. P. Ippen, and N. Bloembergen. Femtosecond laser interaction with metallic tungsten and nonequilibrium electron and lattice temperatures. *Phys. Rev. Lett.*, 53(19):1837–1840, Nov 1984.

[47] S. I. Anisimov, B. L. Kapeliovich, and T. L. Perelman. Electron emission from metal surfaces exposed to ultrashort laser pulses. *Zhurnal Eksperimental noi i Teoreticheskoi Fiziki*, 66:776–781, August 1974.

[48] H. E. Elsayed-Ali, T. Juhasz, G. O. Smith, and W. E. Bron. Femtosecond thermoreflectivity and thermotransmissivity of polycrystalline and single-crystalline gold films. *Phys. Rev. B*, 43(5):4488–4491, Feb 1991.

[49] C.-K. Sun, F. Vallée, L. H. Acioli, E. P. Ippen, and J. G. Fujimoto. Femtosecond-tunable measurement of electron thermalization in gold. *Phys. Rev. B*, 50(20):15337–15348, Nov 1994.

[50] Private discussion with S. Fahy.

[51] C. Thomsen, J. Strait, Z. Vardeny, H. J. Maris, J. Tauc, and J. J. Hauser. Coherent phonon generation and detection by picosecond light pulses. *Phys. Rev. Lett.*, 53(10):989–992, Sep 1984.

[52] L. D. Landau and E. M. Lifshitz. *Theory of Elasticity*. Oxford.

[53] Private discussion with S. Fahy and use the result of E. D. Murray's numerical calculation.

[54] M. F. DeCamp, D. A. Reis, et al. Coherent control of pulsed x-ray beams. *Nature*, 413:825–828, October 2001.

[55] D. A. Reis, M. F. DeCamp, et al. Probing impulsive strain propagation with x-ray pulses. *Phys. Rev. Lett.*, 86(14):3072–3075, 2001.

[56] S. H. Lee, A. L. Cavalieri, et al. Generation and propagation of a picosecond acoustic pulse at a buried interface: Time-resolved x-ray diffraction measurements. *Phys. Rev. Lett.*, 95(24):246104, 2005.

[57] M. Trigo, Y. M. Sheu, D. A. Arms, J. Chen, S. Ghimire, R. S. Goldman, E. Landahl, R. Merlin, E. Peterson, M. Reason, and D. A. Reis. Probing unfolded acoustic phonons with x rays. *Physical Review Letters*, 101(2):025505, 2008.

[58] S. L. Johnson, P. Beaud, C. J. Milne, F. S. Krasniqi, E. S. Zijlstra, M. E. Garcia, M. Kaiser, D. Grolimund, R. Abela, and G. Ingold. Nanoscale depth-resolved coherent femtosecond motion in laser-excited bismuth. *Phys. Rev. Lett.*, 100(15):155501, 2008.

[59] http://www.aps.anl.gov/.

[60] D. Attwood. *Soft X-Rays and Extreme Ultraviolet Radiation: Principles and Applications*. Cambridge University Press, 1^{st} edition, 2007.

[61] S. Brauer, G. B. Stephenson, and M. Sutton. Perfect crystals in the asymmetric bragg geometry as optical elements for coherent x-ray beams. *Journal of Synchrotron Radiation*, 2:163–173, 1995.

[62] Jesse W. M. DuMond. Theory of the use of more than two successive x-ray crystal reflections to obtain increased resolving power. *Phys. Rev.*, 52(8):872–883, Oct 1937.

[63] D. Strickland and G. Mourou. Compression of amplified chirped optical pulses. *Opt. Commun*, 56:219, 1985.

[64] H.-J. Hagemann, W. Gudat, and C. Kunz. Optical constants from the far infrared to the x-ray region: Mg, Al, Cu, Ag, Au, Bi, C, and $A1_2O_3$. *J. Opt. Soc. Am.*, 65(6):742–744, 1975.

[65] J. B. Renucci, W. Richter, M. Cardona, and E. Schonherr. Resonance raman scattering in group Vb semimetals: As, Sb, and Bi. *Physica Status Solidi (b)*, 60(1):299–308, 1973.

[66] F. Völklein and E. Kessler. Analysis of the lattice thermal conductivity of thin films by means of a modified mayadas-shatzkes model: The case of bismuth films. *Thin Solid Films*, 142(2):169 – 181, 1986.

[67] T. K. Cheng, J. Vidal, H. J. Zeiger, G. Dresselhaus, M. S. Dresselhaus, and E. P. Ippen. Mechanism for displacive excitation of coherent phonons in Sb, Bi, Te and Ti_2O_3. *Appl. Phys. Lett.*, 59:1923, 1991.

[68] M. F. DeCamp, D. A. Reis, P. H. Bucksbaum, and R. Merlin. Dynamics and coherent control of high-amplitude optical phonons in bismuth. *Phys. Rev. B.*, 64:092301, 2001.

[69] K. Sokolowski-Tinten, C. Blome, J. Blums, A. Cavalleri, C. Dietrich, A. Tarasevitch, I. Uschmann, E. Förster, M. Kamller, M. Horn von Hoegen, and D. von der Linde. Femtosecond X-ray measurement of coherent lattice vibrations near the Lindenmann stability limit. *Nature*, 422:287–289, 2003.

[70] S. Fahy and D. A. Reis. Coherent phonons: Electronic softening or anharmonicity? *Phys. Rev. Lett.*, 93:109701, 2004.

[71] P. Beaud, S. L. Johnson, A. Streun, R. Abela, D. Abramsohn, D. Grolimund, F. Krasniqi, T. Schmidt, V. Schlott, and G. Ingold. Spatiotemporal stability of a femtosecond hard–x-ray undulator source studied by control of coherent optical phonons. *Physical Review Letters*, 99(17):174801, 2007.

[72] S. L. Johnson, P. Beaud, E. Vorobeva, C. J. Milne, É. D. Murray, S. Fahy, and G. Ingold. Directly observing squeezed phonon states with femtosecond x-ray diffraction. *Phys. Rev. Lett.*, 102(17):175503, 2009.

[73] German Sciaini, Maher Harb, Sergei G. Kruglik, Thomas Payer, Christoph T. Hebeisen, Frank-J. Meyer zu Heringdorf, Mariko Yamaguchi, Michael Horn-von Hoegen, Ralph Ernstorfer, and R. J. Dwayne Miller. Electronic acceleration of atomic motions and disordering in bismuth. *Nature*, 458:56–59, 2009.

[74] In principle the rapidly expanding plasma can also generate coherent phonons during roughly the first half phonon periods.

[75] Yakov Eckstein, A. W. Lawson, and Darrell H. Reneker. Elastic constants of bismuth. *Journal of Applied Physics*, 31(9):1534–1538, 1960.

[76] Alexander Q. Wu and Xianfan Xu. Coupling of ultrafast laser energy to coherent phonons in bismuth. *Applied Physics Letters*, 90(25):251111, 2007.

[77] D. H. Reitze, X. Wang, H. Ahn, and M. C. Downer. Femtosecond laser melting of graphite. *Phys. Rev. B*, 40(17):11986–11989, Dec 1989.

[78] Pier Luigi Silvestrelli and Michele Parrinello. Ab initio molecular dynamics simulation of laser melting of graphite. *Journal of Applied Physics*, 83(5):2478–2483, 1998.